# MACHINE LEARNING-BASED MULTISCALE MODELING AND CONTROL OF QUANTUM DOT MANUFACTURING AND THEIR APPLICATIONS

A Dissertation

by

NIRANJAN ARVIND SITAPURE

Submitted to the Graduate and Professional School of
Texas A&M University
in partial fulfillment of the requirements for the degree of

DOCTOR OF PHILOSOPHY

| | |
|---|---|
| Chair of Committee, | Joseph Sang-Il Kwon |
| Committee Members, | Stratos Pistikopoulos |
| | Perla Balbuena |
| | Eduardo Gildin |
| Head of Department, | Victor Ugaz |

August 2023

Major Subject: Chemical Engineering

ABSTRACT

In the past few years, there has been a major impetus in the search for quantum dots (QDs), which are a type of semiconducting nanocrystals (NCs) with tunable optical and optoelectronic properties for next-generation photonic devices. This can be attributed to their relatively high photoluminescence quantum yield, wide color gamut, tunable optoelectronic properties, and cost-effective solution processibilities. Furthermore, the rising market share of these applications has led to an increased demand for fast and scalable production of QDs and the associated optoelectronics devices. However, there are major commercialization challenges associated with the manufacturing of QDs: (a) lack of mechanistic understanding of the crystallization kinetics of various QD systems, which hinders the predictive control of the QD size distribution; (b) absence of a well-established paradigm for high-fidelity modeling and scale-up of various QD manufacturing processes (e.g., crystallization and thin-film deposition); and (c) no presence of computationally efficient solutions for control and optimization of QD processes.

To address these knowledge gaps, in this work, we develop different models to describe the mechanism of QD crystal growth, enable fast-scalable manufacturing of QDs and the associated optoelectronic devices, and develop an appropriate control framework for various QD processes. First, a first-principled kinetic Monte Carlo (kMC) was developed and experimentally validated to describe the crystallization kinetics of QDs. Second, to resolve the various issues associated with the batch synthesis of QDs, continuous manufacturing of QDs using a plug flow crystallizer (PFC) was demonstrated using a multiscale modeling approach. Further, this approach was extended to two-phase slug flow crystallizers (SFCs) by combining the construction of a CFD-based multiscale model. Also, a highly efficient data-driven optimal control framework was formulated using a deep neural network (DNN) to control QD crystal size and distribution. Third, modeling of thin-film deposition required for manufacturing of solar cells and high-resolution displays was performed. Specifically, a multiscale model that combines the surface-level discrete element method (DEM) model of QD aggregation and macroscopic mass and energy balance equations was

developed for describing the spray coating of QDs. Further, given the computational expense of this model, a surrogate DNN model was developed, which was integrated with a model predictive controller (MPC) to control the film characteristics (i.e., thickness and roughness). Next, although the resulting thin-films are of the desired quality, they are chemically labile and cannot withstand subsequent downstream processing during the manufacturing of LEDs or solar cells. Thus, a kMC model was developed to describe crosslinking of QD thin-films for increased chemical robustness resulting in the manufacturing of high-resolution displays. Moreover, it is important to note that all of the above-developed models were experimentally validated using appropriate experimental observations.

Lastly, although the above-developed model accurately describes various processes related to QD manufacturing, these models are very system-specific, and cannot be easily extrapolated to other QD systems. To provide a concrete direction for addressing this issue in the future, we propose a transformer-based hybrid model, which can leverage the remarkable transfer learning properties of transformers for better generalization across different QD systems. Overall, the proposed work addresses three major challenges in the QD field (i.e., control of QD kinetics, continuous production of QDs, and designing manufacturing processes for fast scale-up of QD-based devices) by developing various experimentally validated multiscale models and combining them with an appropriate control framework.

# ACKNOWLEDGMENTS

I would like to thank Dr. Joseph Kwon, my doctoral advisor, for his constant guidance and dedication to my research work, as well as for teaching me about research methodology, academic writing, work ethic, and strategic planning. Similarly, Dr. Pistikopoulos' teachings have contributed to my leadership qualities, professional growth, and charisma. In addition, I would like to appreciate Dr. Balbuena, Dr., and Dr. Eduardo Gildin for carefully reviewing my research and providing insightful feedback.

All members of the Kwon Research Group have supported this dissertation in numerous ways. I greatly value their scholarly as well as friendship-based generosity. Specifically, Parth Bhandakkar, Sagar Lakhwani, Silabrata Pahari, Parth Shah, Dr. Bhavana Bhadriradju, Dr. Pallavi Kumari, Dr. Abhinav Narasingam, and Dr. Dongheon Lee have been perpetual supporters of my PhD voyage. In addition, I have learned, joked, and collaborated with many others from the Texas A&M Energy Institute, and I would like to express my appreciation by singling out Dr. Iosif Pappas, Dr. Akhilesh Gandhi, Dr. Spyros Tsolas, Dr. Baris Burnak, Moustafa Ali, and others. In addition, numerous peers, mentors, and allies from the Chemical Engineering Department have been instrumental in keeping me on track during my PhD. I would like to mention Dr. Rachit Gupta, Soham Kulkarni, Rushant Sabnis, Suvesh Lalwani, Debopamaa Debnath, Suyash Oka, Niraj Vidwans, Atharva Kulkarni, Jitesh Pandya, Dr. Kasturi Sarang, Dr. Nutan Patil, Dr. Naveen Mishra, Akshaya Kulkarni, Tushar Goel, Dr. Omkar Bhatavdekar, and umpteen others. Ashley Henley, Terah Cooper, and Jeff Sammons deserve special recognition for guiding me through all administrative difficulties during my graduate career.

Next, I would be negligent if I did not thank my close friends and family members, including Omkar Gavhane, Tejaswini Gavhane, the Mulay family, Tamara McNiece, and Sarah Binker, with special appreciation. My parents, Arvind and Jyoti Sitapure, and my partner, Ojaswini Parab, have been my most steadfast supporters throughout my Ph.D. voyage.

Live Long and prosper!

# CONTRIBUTORS AND FUNDING SOURCES

## Contributors

This work was supported by a thesis committee consisting of Dr. Joseph Kwon, Dr. Perla Balbuena, Dr. Stratos Pistikopoulos of the Artie McFerrin Department of Chemical Engineering, and Dr. Eduardo Gildin of the Harold Vance Department of Petroleum Engineering. All other work conducted for the dissertation was completed by the Niranjan Sitapure independently.

## Funding Sources

Financial support from the Artie McFerrin Department of Chemical Engineering, and the Texas A&M Energy Institute are gratefully acknowledged. r

TABLE OF CONTENTS

Page

LIST OF FIGURES

FIGURE Page

# LIST OF TABLES

TABLE Page

# 1. INTRODUCTION AND LITERATURE REVIEW

## 1.1 Motivation

The US Department of Energy has set high-priority targets to reduce the cost of photovoltaics from $\sim$ 15 cents/kWh to 5 cents/kWh by 2030. This has fueled a plethora of research in the discovery, optimization, and commercial production of high-efficiency solar cells [4, 5]. Towards this goal, QD-based solar cells have received special attention due to their high quantum efficiency and tunable absorption/emission spectra [6, 7, 8]. Furthermore, increasing market demand for energy-efficient high-resolution displays (HRDs) has also propelled the search for new semiconducting materials which can be nano-patterned to provide the high-resolution requirement [9, 10, 11, 12]. Even in this area, various QDs with a wide color gamut, and high photoluminescence quantum yield (PLQY) have shown promising results [13]. Basically, the plethora of applications (i.e., solar cells, HRDs, and other optoelectronics devices) has propelled the investigation of various QDs, their properties, manufacturing techniques, and potential real-world applications [14, 15, 16].

To this end, the literature is rife with studies investigating the synthesis, and effect of different process parameters on the tunable characteristics of QDs, and comparing different synthesis protocols for better control of QD size (a crucial factor in determining the photoelectronic properties of QDs) [17, 18, 19, 20]. Unfortunately, previous studies are majorly focused on the small lab-scale batch synthesis of QDs using umpteen number of different reaction protocols and do not conclusively yield an understanding of QD crystallization kinetics that can assist in designing better manufacturing protocols [21, 22]. Thus, a continuous synthesis platform for large-scale QD production with precise size-tuning and prediction capability is highly coveted in the semiconductor community. Further, manufacturing of QD-based devices (i.e., solar cells and HRDs) needs advanced processing capabilities like lithography and thin-film deposition, which have not seen a detailed computational investigation [23, 24, 25]. Thus, there is an absence of modeling and optimization studies to enable scale-up, better yield, and superior process control of QD-based

thin-film deposition for the manufacturing of various optoelectronics. Overall, the three major challenges in this field are (a) the need for a mechanistic understanding of various QD processes to enable better QD models; (b) the lack of a well-established paradigm for high-fidelity modeling and scale-up of various QD manufacturing processes (e.g., crystallization and thin-film deposition); and (c) no presence of computationally efficient solutions for control and optimization of QD processes.

## 1.2 Literature Review

Given the variety of the above challenges, a single modeling technique or standalone process will not provide a viable solution, thereby requiring a combination of various modeling, control, and validation techniques. Thus, this section provides an overview of various existing works in the literature that can be leveraged to effectively address the above challenges.

### 1.2.1 Crystallization and Size Control of QDs

Various approaches in the literature have demonstrated size-tuning or bandgap tuning of QDs, and they can be divided into three categories. First, a set of literature studies achieve facile tuning of QD bandgap through halide/anion exchange [26, 27, 28]. The second set of studies utilizes different surface ligand species with varying chain lengths and concentration [29, 30, 31, 32] to control QD size. Here, the ligands form a ligand shell around the QDs, and hinder the mass transfer of solute to control the growth kinetics, and thereby the size of QDs. Third, there are some studies utilizing hot-injection (HI) techniques [33, 34, 35, 36], where reaction temperature is utilized to control the QD size. However, although there is a plethora of QD synthesis techniques, they provide little insight into the crystallization kinetics of QDs. For example, during the HI synthesis, the crystallization reaction proceeds very rapidly (i.e.,$\sim$5 s) making it challenging to control the size of QDs in every batch, thereby leading to a wide size distribution. Then, the ligand-based QD control techniques majorly focus on the exploration of different ligand species and chain lengths to control QD size and shed little light on the mechanism by which these ligands help control the QD size. Furthermore, existing crystallization models, which are primarily developed for organics and

protein crystallization cannot mimic QD growth kinetics [37, 38, 39, 40]. Thus, the development of an alternate crystallization model that can help predict and control QD size is required.

### 1.2.2 Continuous QD Manufacturing

Conventional lab-scale QD synthesis techniques are difficult to scale up to meet the market demand and there is batch-to-batch variation resulting in wide QD size distribution, which affects the performance of QD-based devices. Recently, there have been some efforts towards the development of continuous manufacturing techniques for QDs. For example, recent studies showcased a millifluidic platform for fast-scalable manufacturing of $CsPbBr_3$ QDs in the size range of 5 to 10 nm [41, 42]. However, currently there are no well-established models to describe continuous QD crystallization, and further control the QD size using an appropriate framework. Then, another experimental study demonstrated a slug-flow crystallizer (SFC) for continuous production of QDs [43]. Specifically, the authors utilized a millifluidic SFC with an inlet for inert gas and the precursor solution and manipulated these flow rates to facilitate size-tuning of $CsPbBr_3$ QDs. They showcased that an SFC operating in a stable regime provides alternating gas-liquid slugs; each liquid slug acts as a batch crystallizer, whereas the entire SFC behaves as a continuous reactor. However, although these select few studies demonstrate continuous production of QDs, the literature lacks high-fidelity models which can be used for scale-up and subsequent control of the above processes. For example, existing SFC models do not account (a) slug-to-slug (S2S) variation (i.e., all liquid slugs are not identical) can affect the crystallization kinetics and the overall CSD; and (b) do not have appropriate controllers that can manipulate air/liquid flow rates for regular QD size. Thus, there is a strong need for the development of a QD crystallization platform that combines a high-fidelity crystallizer model with an adequate controller to regulate QD crystal size for enabling continuous manufacturing of QDs in PFCs and SFCs.

### 1.2.3 Thin-film Deposition of QDs

A majority of QD-based applications need QD thin films to be used in solar cells or HRDs. For example, current solar cell manufacturing utilizes spin coating to produce QD-based thin films,

which then act as a functional/active layer [44, 45, 46]. However, batch-to-batch variation, low material utilization, and the requirement of a separate curing step act as major challenges in the fast-scalable production of QD-based devices. To resolve this issue, spray coating of QDs has been proposed in the literature to address the above challenges [47, 48, 49]. Furthermore, studies show that spray coating couples macroscopic phenomena (e.g., transport and thermal), and surface-level interactions (i.e., coffee ring effect) contributing to the uneven deposition of thin-film, which is detrimental to the optoelectronic performance of QDs [50, 51]. Thus, to enable the optimal control of thin-film characteristics, it is important to have an accurate QD spray coating model, which can account for the coupling of the above-mentioned surface-level and continuum-level phenomenon.

Another major area where thin-film QDs have received significant attention is the nanopatterning of QDs using photolithography for direct application in HRDs [52, 53]. However, when integrating QDs into thin-film photonic devices, the QD films are damaged during post-processing steps involving various chemical solvents [54, 55]. To this end, ligand crosslinking of QDs has emerged as a promising scalable solution [56]. However, despite the successful formation of crosslinked QD films, these studies offer little insight into the kinetics and mechanism of the crosslinking reaction. Thus, it is imperative to develop an appropriate model to address this knowledge gap, which devise better nano-patterning techniques for the manufacture of QD thin films in the future.

### 1.2.4 Multiscale Modeling Techniques

The above two challenges (i.e., continuous QD manufacturing and spray coating-based thin-film deposition) require a certain level of multiscale modeling. Specifically, for PFC and SFC, crystal growth kinetics at the microscopic scale need to be coupled with continuum-level mass and energy balance equations. Similarly, for spray coating, there are QD-QD interactions at the surface level that results in thin-film deposition while at the macroscopic level, there is droplet atomization, heat transfer, and droplet evaporation. Overall, a majority of QD manufacturing techniques require a combination of system-agnostic macroscopic models with QD-specific microscopic interactions, thereby necessitating the formulation of a multiscale modeling framework. To this end, there are

many studies in the literature that utilize such an approach for a wide variety of chemical processes.

#### *1.2.4.1 Multiscale Modeling of Crystallization*

Christofides and colleagues have done extensive research work on multiscale modeling and control of protein crystallization by coupling microscopic-level kinetic Monte Carlo (kMC) with macroscopic mass and energy balance equations. Specifically, one of the initial studies focuses on the development and experimental validation of a high-fidelity kMC model, which considers several microscopic steps (i.e., adsorption, migration, and desorption), of lysozyme crystallization [57, 37]. The next few studies focus on utilizing the kMC model in conjunction with macroscopic mass and energy balance equations for a batch crystallizer. and further utilizing a model predictive controller (MPC) to regulate not only the crystal size distribution (CSD) but also the shape of lysozyme crystals [37, 58]. This work further extended to continuous crystallization and was also integrated with a run-to-run control scheme to provide better control over the CSD [59, 60]. Further, the above models were coupled with particle aggregation dynamics, fine removal strategies, and product classification protocols to maximize the productivity of continuous protein crystallizers while reducing the polydispersity [61, 62]. Finally, to handle the issue of computational expense of the above models, one of the studies focuses on development of a multidomain MPI-powered parallel computation framework that utilizes a combination of problem decomposition, task assignment, and information flow orchest ration techniques to achieve a speed boost of $\sim 40$ times [63]. The above works provide a perfect starting point for developing similar multiscale models for QD-specific crystallization systems.

#### *1.2.4.2 Multiscale Modeling of Thin-Film Deposition*

Considering the other aspect of thin-film deposition, there also have been some notable multiscale modeling studies by Christofides and colleagues that couple a surface-level kMC model with gas-phased microscopic models to describe the plasma-enhanced chemical vapor deposition (PECVD) for manufacturing silicon solar cells. Specifically, the kMC models include four processes (i.e., physisorption, surface migration, hydrogen abstraction, and chemisorption), and is

combined with gas-phase two-dimensional partial differential equations that account for chemical reactions, diffusion, and convection [64]. Using the developed model, thin-film deposition with uniform thickness and an optimized light-trapping surface microstructure can be achieved by choosing different gratings of the wafer surface. Moreover, the authors also demonstrate the use of run-to-run control that uses an exponentially weighted moving average (EWMA) control algorithm to reduce batch-to-batch variability between different deposition cycles [65]. Finally, these models are integrated with a CFD model to accurately capture plasma chemistry and transport phenomena in a 2D/3D axisymmetric reactor geometry through a dynamic boundary that connects the surface-level wafer domain with the gas-phase [66, 67]. Similarly, Sandoval and colleagues have developed various multiscale thin-film deposition models for a generalized CVD system that combines continuum-level transport model with a surface-level kMC model. Moreover, to gain computational efficiency, they utilize an artificial neural network to surrogate the multiscale thin-film model, and then incorporate it within a MPC to control thin-film characteristics [68, 69]. This model was extended to a stochastic MPC implementation by accounting the inherent uncertainty of the thin-film deposition process by polynomial series expansion (PSE) and a DNN-based framework [70, 71]. Thus, the above works were utilized as a reference to formulate the multiscale modeling framework for thin-film deposition.

#### *1.2.4.3 Multiscale Modeling of Pulping Process*

Although the above two subsections provide structural guidance on multiscale modeling of QD systems, there are other notable multiscale modeling studies from the literature that provide background for coupling of different lengths and time scales, and methods to computationally treat such systems. For example, Kwon and colleagues performed extensive studies on multiscale modeling of the wood pulping process. Specifically, they coupled (a) a microscopic kMC model that describes the delignification process of various constituents (i.e., lignin, cellulose, and hemicellulose) in the presence of entrapped liquor with (b) a continuum-level Purdue model that considers mass and energy balance equations along with cell wall thickness (CWT) and Kappa number ($K$) [72, 73]. After experimental validation of the above model, it was integrated with dif-

ferent soft sensors (e.g., Kalman Filter and Luenberger observer) and implemented within an MPC for regulating CWT and $K$ [74]. Further, the kMC model was modified with various scission and degradation mechanisms that are applied to an ensemble of wood fibers to consider fiber-to-fiber heterogeneity, and subsequently regulate the fiber-length-distribution (i.e., similar to controlling CSD) [75, 76, 77]. Also, a different study addresses the issue of fiber strength, which is essential in the paper-based packing industry, by integrating modified buckling theory along with kMC and the Purdue model, and subsequently using a MPC to reach a target fiber strength of packaging applications [78]. Finally, as these high-fidelity models are computationally expensive, data-driven or machine learning (ML)-based surrogate models were developed to expedite the online implementation of MPC for the pulping process [79, 80]. Moreover, given the highly nonlinear and complex nature of the pulping process, an offset-free MPC scheme, which utilizes a disturbance model that is augmented with the state-matrix to minimize the offset, was demonstrated for this process [81]. In the context of QD processes, the above studies provide inspiration for treating different lengths and time scales in a computationally tractable manner for efficient online control as it will be essential during QD manufacturing.

#### *1.2.4.4 Kinetic Monte Carlo Simulation (kMC)*

The above examples illustrate that system-specific microscopic interaction can be effectively captured by kMC simulations, as it is a powerful tool for procuring feature-rich information about the spatiotemporal evolution of the process at a fraction of the cost than Molecular Dynamics (MD) or other molecular simulation tools [82, 83, 84]. More importantly, kMC models can be easily integrated with continuum-level mass-energy balance and population balance equations for the realistic modeling of chemical reactors, fermenters, pulp digesters, and crystallized [85]. Furthermore, kMC simulations are not restricted to simple adsorption, desorption, and migration steps as indicated by the above subsections, and can be easily extended to more complex phenomena.

For example, Kwon and colleagues developed extensive kMC models for different biological systems including cholera toxin subunit B (CTB), multivalency glycan-lectins, and their receptive receptors (e.g., GM1, GM2, GD1b, and others) [86, 87, 88, 89]. Specifically, the kMC model

describes the binding mechanism between CTB and GM1 receptors along with the competitive binding of GM2 receptors [90]. Moreover, different size and shape of CTB and GM1 receptors can also be considered along with different binding pockets. Using the above models as a basis, several new models that address cell-to-cell heterogeneity and complexity signaling pathways have been developed [91, 92]. These models provide inspiration to tackle the QD-QD crosslinking issue, wherein a kMC model is required to model the interaction between QDs and various multidented crosslinkers.

Another well-established use case of kMC simulations is in regards to heterogeneous catalysis, wherein a multitude of microkinetic reaction steps can be modeled with respective rate equations, various interactions between reaction species can be considered, and the lattice sites can be modified to reflect some degradation reactions. For example, Kwon and colleagues recently developed a comprehensive reaction kMC simulation for modeling the nitrogen reduction reaction (NRR) for shortlisting high-performance bimetallic transition metal catalysts [93, 94]. The literature is rife with similar notable works for treating industrially relevant catalyst systems [95, 96, 97, 98]. A similar work is performed by Sandoval and colleagues, wherein they utilize kMC to model surface chemistry within a tubular catalytic reactor to account for various process uncertainties, and subsequently develop a hybrid kMC-data-driven model for simulating this process [99, 100, 101]. Furthermore, Sandoval and colleagues have also developed several kMC models for moving boundary problems in various microscopic interfacial systems [102, 103].

Moreover, these models were extrapolated to even microscopic modeling of battery systems. Specifically, Kwon and colleagues developed a microscopic kMC simulation for modeling dendrite-based capacity degradation in Lithium-ion batteries, wherein different electrochemical reactions at the battery electrodes are considered. Further, the kMC model also takes input from different mechanical properties of battery electrolytes and materials (e.g., Elasticity modulus, diffusion coefficient, and others) to dynamically change the dendrite forming reactions [104, 105, 106]. Overall, the above studies demonstrate that many different microscopic phenomena (i.e., reaction, diffusion, degradation, etc.) can be considered in a kMC model using the appropriate equations,

thereby providing a strong modeling paradigm for treating various QD-specific interactions using a kMC model.

### 1.2.5 Existing Data-driven Modeling Techniques

As mentioned earlier, although a standalone or combination of various high-fidelity modeling techniques can be utilized for resolving the above challenges, online process monitoring and control requires the presence of computationally efficient data-driven surrogate models. An overview of the literature suggests that there are three categories of such models: (a) subspace identification models; (b) machine learning (ML)-based models; and (c) next-generation hybrid models.

#### *1.2.5.1 Subspace Identification Models*

A popular approach to developing surrogate models is using data-driven model order reduction techniques. For example, Kwon and colleagues demonstrated the characterization of reservoir properties by considering the proper orthogonal decomposition (POD) technique to reduce the dimensionality of spatially varying Young's modulus profiles to accurately predict fracture propagation dynamics in hydraulic fracturing [107]. Basically, a POD technique identifies the dominant modes in a dataset by extracting the most important features, and these features can be linear combinations of the original state variables that capture the maximum amount of variability in the data [108, 109].

Another powerful approach is sparse identification of system dynamics (SINDy), wherein it utilizes a library of basis functions (selected using *a priori* process information) to find a sparse and interpretable set of equations to describe dynamic chemical processes (e.g., second-order CSTR, hydraulic fracking, battery dynamics, etc.). In addition, SINDy focuses on sparsity by finding a small number of basis functions that have the most significant impact on the system's behavior [110, 111]. However, since SINDy models utilize process data for a certain system, they tend to be very system-specific, and show plant-model mismatch when process parameters (e.g., rate constants, diffusion kinetics, degradation mechanism) change. To tackle this issue, Kwon and colleagues have developed and extensively demonstrated operable adaptive sparse identification of

systems (OASIS) models, wherein many different individual SINDy models are trained and then congregated using a deep neural network (DNN). This allows the OASIS model to adeptly select a local SINDy suited for the current process condition for minimal plant-model mismatch [112, 113]. This framework can be event extended for dynamic risk-based fault prediction in industrial scale chemical processes [114]. Very recently, a two-stage OASIS model was demonstrated for modeling capacity fade and cell failure in lithium-ion batteries [115], wherein two separate OASIS models, one for inter-cycle degradation and another for intra-cycle degradation, was successfully combined for producing accurate predictions.

Finally, a similar approach was introduced by Kwon and colleagues using the Koopman operator framework, which utilizes a set of basis functions to transform a low-dimensional nonlinear system into a higher-dimensional linear system that is easy to compute and integrate with an MPC [116]. Further, this framework was demonstrated for reactor systems and even highly nonlinear hydraulic fracking systems [117]. More importantly, a Koopman Lyapunov-based MPC (KLMPC) framework was demonstrated and theoretically proved to show closed-loop stability on a certain set of chemical systems [118], and this study was extended to further guarantee closed-loop stability of nonlinear systems by using a bilinear Koopman MPC system [119]. Furthermore, to address the challenge of plant-model mismatch due to the Koopman approximation, an offset-free KLMPC framework was formulated and showcased for accurate regulation of batch pulp digester [79, 120]. Overall, there are several powerful data-driven reduced-order modeling techniques that can be utilized to resolve some of the computational challenges associated with QDs.

#### *1.2.5.2 Machine Learning Models*

In the past decade, literature is rife with instances of ML-based surrogate models that DNN, convolution neural networks (CNN), recurrent neural networks (RNN), and others to describe various chemical processes. First, a majority of the works demonstrated DNNs for input-output prediction, surrogate modeling, and time-series modeling in catalyst, biochemical, and fault detection applications [121, 122, 123, 124, 92]. Second, many studies utilized convolution neural networks (CNNs), which allows spatiotemporal convolution and automatic feature detection, for applica-

tions in process analysis tools (PAT), spectroscopy image analysis and characterization along with a few cases of time-series prediction [125, 126, 127, 128, 129]. In another study, Bensmail and colleagues developed *DeepCrystal* for protein sequence-based prediction of crystal morphology [130] using a deep-CNN. Abolhasani and colleagues developed a DNN model to predict QD size and bang gap at the end of the crystallization process [131, 42]. Also, Shuangshuang and colleagues developed a CNN model for online image analysis in crystallizers for monitoring the progress of sugar crystallization [132]. Lastly, Hasan and colleagues provide a comprehensive overview of various DNN and CNN-based models for expedited exploration of search space in the field of computational material discovery [133].

Third, although DNNs and CNNs show quick training times, easy construction, and straightforward hyper-parameter tuning, they are not tailor-made for long-term time-series predictions, which is often required in complex non-linear chemical systems (i.e., crystallization, battery models, heterogeneous catalysis, etc.). To this end, there have been few instances of utilizing sequential ML models like recurrent neural networks (RNNs) and long-short-term-memory (LSTM) networks for time-series modeling in complex chemical systems. More precisely, the internal model architecture of RNN and LSTM is designed to consider various model states/features in the form of a time-series sequence using an internal *for loop* that reads the input state information at each time-point (i.e., $[X_t, X_{t-1}...X_{t-w}]$) and predicts the state at the next time-point (i.e., $y_{t+1}$). Consequently, RNN and LSTM models often perform better than DNN and CNN for long-term prediction of dynamic chemical systems even with reasonable model size and adequate training data [134, 135, 136, 137, 138]. For example, Wu and coworkers utilized an encoder-based RNN to learn the dynamics for batch crystallization of Fesoterodine fumarate [139, 140]. The encoder layer helps transform crystal size distribution (CSD) in a lower dimensional space that is more computationally tractable for the RNN to handle, thereby giving good prediction results. Overall, the abovementioned ML techniques can be treated as a guide path for modeling several computationally expensive aspects of QD manufacturing processes.

#### *1.2.5.3 Hybrid Modeling Techniques*

Although the above ML techniques show high accuracy and ease of model training, they result in black-box models that are not interpretable, and difficult to numerically treat within an online MPC or an optimal operation problem. Thus, there has been a strong impetus to develop hybrid models that combine system-agnostic first principles (e.g., mass and energy balance, transport phenomena, and others) with system-specific data-driven parameters (e.g., process parameters, kinetic constants, and others) to result in a 'best-of-both-worlds' approach. Specifically, Kwon and colleagues have developed various hybrid models for different non-trivial chemical systems. For example, in one study, a DNN-based hybrid model is developed for modeling the unknown dynamics of leak-off rate with a PKN model for accurately describing fracture propagation in hydraulic fracking [124]. Another study modifies this framework to dynamically estimate the process parameters (i.e., rate constants, diffusion coefficients, and others) and couple them with macroscopic mass and energy balance equations in an industrial scale fermentation process [141]. Moreover, this model was further modified to develop a physics informed neural network (PINN)-based framework for describing batch kinetics of different lab-scale fermentation processes [142]. Finally, the developed hybrid model framework was integrated within an MPC that guarantees stability within the domain of applicability of the model [143]. In a nutshell, the above examples of hybrid models provide a good background for integrating system-agnostic process equations with QD-specific ML models.

## 1.3 Objectives and Organization of the Proposed Research

The field of manufacturing of QDs and associated applications have garnered significant importance in recent years due to the impetus toward high-performance QD-based devices. However, there are three major challenges in this endeavor, viz., (a) the development of an accurate crystallization model for continuous manufacturing of QDs; (b) high-fidelity modeling of the different processes required in the production of QD-based devices; and (c) development of control framework that utilizes computationally efficient surrogate model for both of the above processes. Thus,

the overall objective of this doctoral study is to address the above challenges using a combination of different microscopic, macroscopic, machine learning, and control techniques. To this end, a schematic illustration of the organization of the proposed work is presented in Figure 1.1.

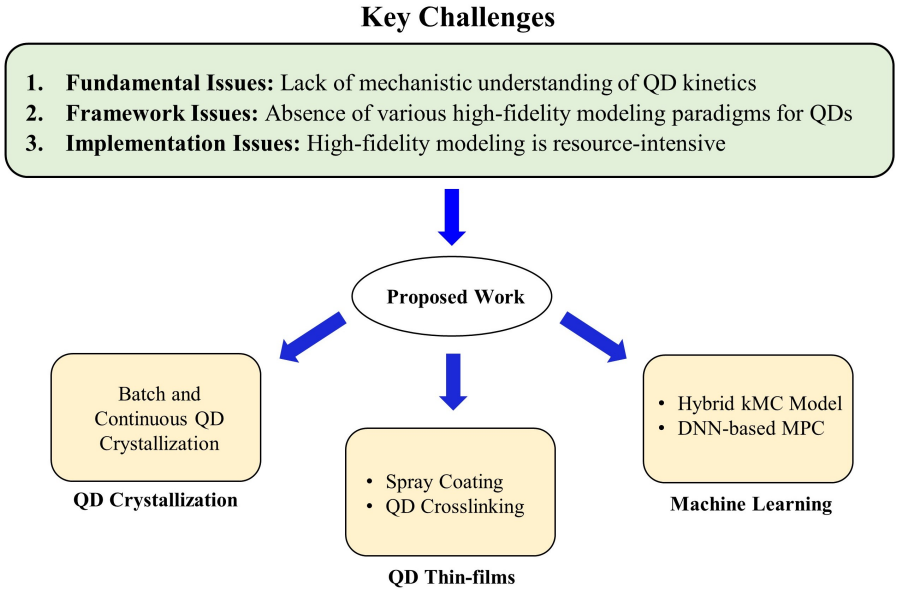


Figure 1.1: Schematic illustration of the proposed work.

Specifically, Section 2 describes our work in the development and testing of a continuous tubular flow crystallizer for fast-scalable manufacturing of QDs. Specifically, a kinetic Monte Carlo (kMC)-based microscopic crystallization model is developed and experimentally validated, and then utilized in conjunction with a nonlinear optimizer to control QD size. Then, Section 3 addresses the challenge of controlling the QDs size and CSD in SFCs by constructing a multiscale model, which combines a computational fluid dynamics (CFD) model, a crystallization model, and a DNN. The above two sections provide appropriate experimentally validated models addressing the challenge of continuous manufacturing of QDs, and thus, the next two sections focus on QD thin-film production. Section 4 presents a discrete element method (DEM)-based spray coating model to describe the thin-film deposition process of QDs along with a demonstration of an MPC

for regulating the film characteristics (i.e., film thickness and roughness). Next, Section 5 details a configuration kMC (ckMC) model describing the ligand crosslinking in QD systems for enabling the better design of nanopatterning techniques for HRD applications. Furthermore, a brief description of two high-impact future directions is mentioned in Section 6. Lastly, Section 7 gives the summary of the proposed work, and the list of publications is presented in Section A.

# 2. MULTISCALE MODELING AND CONTROL OF TUBULAR CRYSTALLIZER FOR CONTINUOUS QD MANUFACTURING*

As mentioned earlier, (a) understanding the crystallization kinetics for QDs (i.e., in this case, $CsPbBr_3$ QDs), and (b) development of a tubular crystallizer model and an associated control framework will be a crucial factor for large-scale continuous manufacturing of $CsPbBr_3$ QDs with size-tuning capabilities. These challenges are addressed by proposing a multiscale model for plug-flow crystallizer (PFC). Specifically, the macroscopic phase of PFC is modeled to describe the dynamic spatiotemporal evolution of precursor concentration and QD size using a continuum model for mass balance. The discretized continuum model is integrated with a kinetic Monte Carlo simulation (KMC) model to formulate a high-fidelity multiscale model; the KMC simulation describes the physics behind QD synthesis (i.e., $CsPbBr_3$ unit cell attachment and mass-transfer rate of ligand adsorption and desorption of the ligand), and its dependence on the local precursor concentration and superficial flow velocity. Then, the developed crystallizer model is experimentally validated. Then, an optimizer, which dictates the optimal input profile (i.e., inlet precursor concentration and flow rate) for set-point tracking is designed. More details about this chapter are presented in our previous work.

## 2.1 Mathematical Modeling of PFC

### 2.1.1 Process Description

We consider a PFC as shown in Figure 2.1 that has a length of 10 cm and an internal diameter of 0.1 cm. The PFC has two manipulated inputs, viz., precursor concentration, $C_o$, and superficial flow velocity, $v_z$, which can be used to fine-tune the size of $CsPbBr_3$ QDs at the end of the PFC, $r_{final}$. For an initial precursor concentration of $C_o$, and superficial flow velocity, $v_o$, the QD crystals start growing at $z_o$ (the entry location of the PFC), and reach the desired set-point value, $r_{final,sp}$,

*Content of this chapter was published in the Chemical Engineering Journal [144], and copyright permission from the journal has been granted for inclusion in the dissertation. All the figures in this work are adapted from the abovementioned journal publication.

at the end of the PFC, $z_n$. Thus, for an accurate description of QD crystal growth in a PFC, it is important to investigate the spatiotemporal evolution of QD crystal size, $r(t, z)$, and precursor concentration, $C(t, z)$, in the PFC.

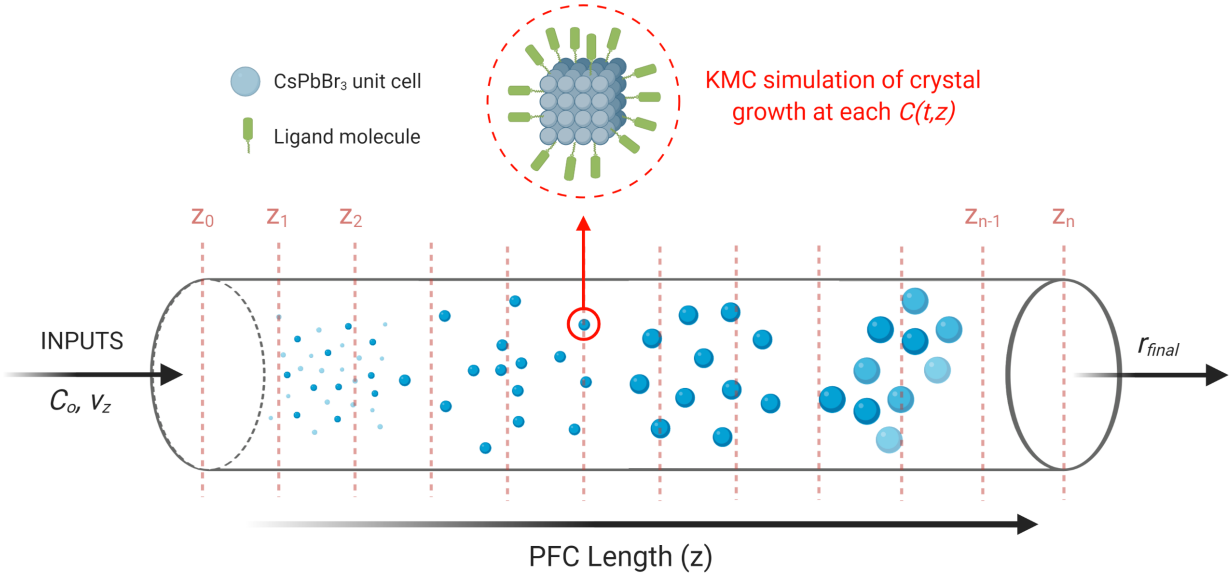


Figure 2.1: Schematic illustration of the proposed multiscale model of a PFC. The inputs to the PFC are the precursor concentration, $C_o$, and superficial flow velocity, $v_z$. The QD crystal size at the end of the PFC is denoted by $r_{final}$. The blue spheres represent the QD crystals growing along the flow direction, and the green extensions around the crystal represent the ligand molecules.

### 2.1.2 Macroscopic Model of the PFC

By employing a standard continuum model, and considering spherical nanocrystals at root temperature, we can describe the mass balance within the PFC as follows:

$$\frac{\partial C}{\partial t} = -v_z \frac{\partial C}{\partial z} - \rho_s n_s(t, z) 4\pi r^2(t, z) G_r(C, v_z, r) \tag{2.1}$$

where $r(t, z)$ is the radius of nanocrystals, $\rho_s$ is the density of $CsPbBr_3$ QD crystal, $\rho_f$ is the density of the solution phase, $n_s(t, z)$ is the number of crystals in the PFC, $v_z$ is the superficial flow velocity in the PFC, and $G_r$ is the one-dimensional (1D) crystal growth rate.

Generally, $G_r$ is estimated experimentally, and is a nonlinear function of precursor concentration and temperature of the solution phase [40, 145]. However, the room-temperature experimental studies show that crystal growth in $CsPbBr_3$ QD synthesis depends on the superficial flow velocity [43, 131]. Further, during $CsPbBr_3$ crystal growth, there are also other phenomena (i.e., ligand-shell formation [146], and Br rich crystal surface [36]) leading to a size-dependent crystal growth behavior. To this end, an alternative approach to computing $G_r(C, v_z, r)$ is required.

### 2.1.3 Microscopic Description of QD Crystal Growth

To accurately model the microscopic crystallization kinetics, the following experimental observation needs to be accounted for in the proposed kMC model. Firstly, the rigorous mixing of the precursors results in multiple $PbBr_6$ octahedra and subsequent formation of $CsPbBr_3$ unit cells, which then aggregate to form QD crystals. Secondly, this is accompanied by the attachment of ligand molecules on $CsPbBr_3$ crystal surface. Thirdly, recent studies have demonstrated the pivotal role of the superficial flow velocity in influencing the mixing characteristics in a PFC [1, 131].

### 2.1.4 KMC Model Development

A KMC model based on a solid-on-solid (SOS) approach, which takes into account the microscopic events (i.e., adsorption, migration, and desorption) occurring in the crystallization process is developed [147, 148].

#### *2.1.4.1 Surface Kinetics*

Firstly, the rate of crystal growth, which dictates the attachment of $CsPbBr_3$ unit cell to the crystal nuclei, is given as follows:

$$r_a = NK_o exp\left(\frac{\Delta\mu_{cry}}{kT}\right); \Delta\mu_{cry} = k_B T ln\left(\frac{C_{cry}}{S}\right) \tag{2.2}$$

where $K_0$ is the attachment rate at equilibrium ($\Delta\mu_{cry} = 0$), $T$ is the temperature in Kelvin, $N$ is equal to the KMC lattice size ($N = 200$), $C_{cry}$ is the precursor concentration [$CsPbBr_3$], $S$ is the solubility of [$CsPbBr_3$], which is a constant, $k_B$ is the Boltzmann constant and $\Delta\mu_{cry}$ refers to the

difference in the chemical potentials of [$CsPbBr_3$] in the solution phase and the crystal.

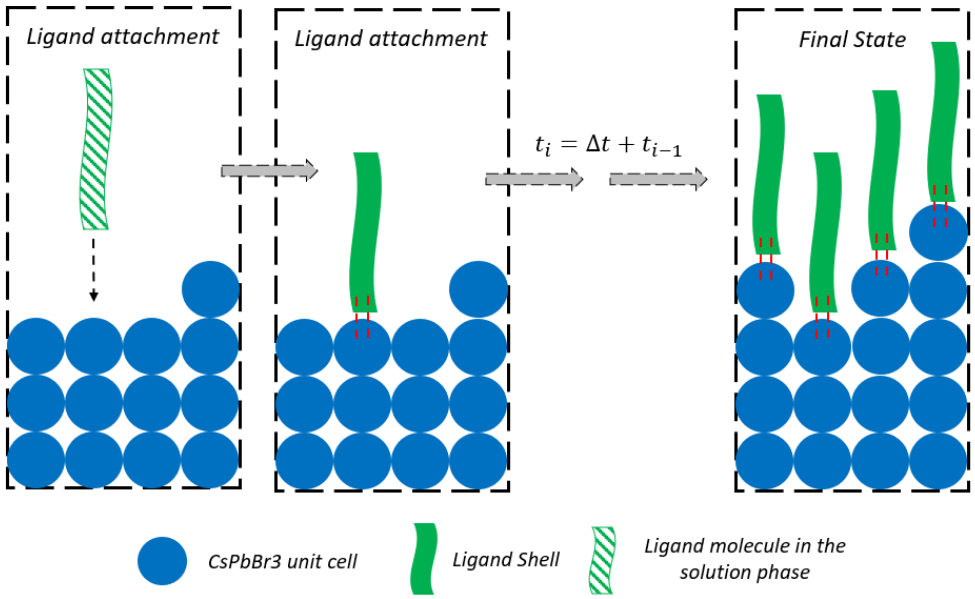


Figure 2.2: Schematic illustration of the ligand attachment event. The green waves schematically show the formation of ligand-shell on the crystal surface, and the blue spheres represent the individual $CsPbBr_3$ unit cells which build up to form one $CsPbBr_3$ QD crystal.

Secondly, the rate of ligand attachment is dictated by the molar flux of th ligand molecules from the solution phase to the crystal surface, which is defined as follows:

$$\begin{aligned} J_{lig} &= h_m \left(C_{lig} - C^*_{lig}\right) \\ r_{lig} &= N J_{lig} N_A d^2 \end{aligned} \tag{2.3}$$

where $h_m$ is the convective mass transfer coefficient, $C_{lig}$ is the concentration of free ligand molecules in the solution phase, $C^*_{lig}$ is the equilibrium concentration of free ligand molecules on the crystal surface, $N_A$ is the Avagadro's constant, and $d$ is the edge length of one unit cell of crystalline $CsPbBr_3$.

Thirdly, the loosely bound ligands can detach and dissolve back in the solution, and this is described as follows:

$$r_d(i) = K_o exp\left(-i\frac{E_b}{k_B T}\right) N_{lig}(i) \tag{2.4}$$

where $E_b$ is the average binding energy per bond between two ligands, $i \in [0, 2]$ is the number of nearest ligand neighbors, and $N_{lig}(i)$ is the number of lattice sites occupied by ligand molecules having $i$ nearest neighbors.

Lastly, the total rate, $W_{total}$, is the sum of all the three individual rates and is defined as $W_{total} = r_a + r_{lig} + \sum_{i=0}^{2} r_d(i)$.

#### *2.1.4.2 kMC Event Execution*

The probability of $CsPbBr_3$ unit cell attachment, ligand attachment, and ligand detachment is represented as $P_a$, $P_{lig}$ and $P_d$, respectively. These probabilities are calculated as shown below:

$$\begin{aligned} P_a &= \frac{r_a}{W_{total}} \\ P_{lig} &= \frac{r_{lig}}{W_{total}} \\ P_d &= \frac{\sum_{i=0}^{2} r_d(i)}{W_{total}} \end{aligned} \tag{2.5}$$

Only one KMC event can be executed at each event execution step. Thus, to determine which event to be executed, a random number, $\xi_1 \in (0, 1]$, is generated and used in conjunction with Table 2.1.

| Probability Conditions | Event Executed |
|---|---|
| $0 < \xi_1 \leq P_a$ | $CsPbBr_3$ unit cell attachment |
| $P_a < \xi_1 \leq P_{lig} + P_a$ | Ligand attachment |
| $P_a + P_{lig} < \xi_1 \leq P_a + P_{lig} + P_d$ | Ligand detachment |

Table 2.1: Probability conditions for selecting a KMC event.

Firstly, if a $CsPbBr_3$ unit cell attachment event is selected, lattice site $i \in [0, N]$ is chosen at random, then a $CsPbBr_3$ unit cell is deposited on lattice site $i$ and will result in crystal growth.

Secondly, if a ligand attachment event is selected, then lattice site $j \in [0, N]$ is selected at random, and a ligand molecule can successfully attach onto the top layer of lattice site $j$, as shown in Figure 2.2. Lastly, it is important to correlate the virtually executed KMC events to the time elapsed in the real world. Hence, after every KMC event, either successful or unsuccessful, there is a corresponding time increment, $\Delta t$, which is given by $\Delta t = \frac{-\log \xi_3}{W_{total}}$, where $\xi_3 \in (0, 1]$ is a random number. The detailed methodology can be found in our previous work [144].

## 2.2 Experimental Validation Results

For experimental validation, time-series data of $CsPbBr_3$ QD crystal size was collected using a millifluidic platform [43, 131].

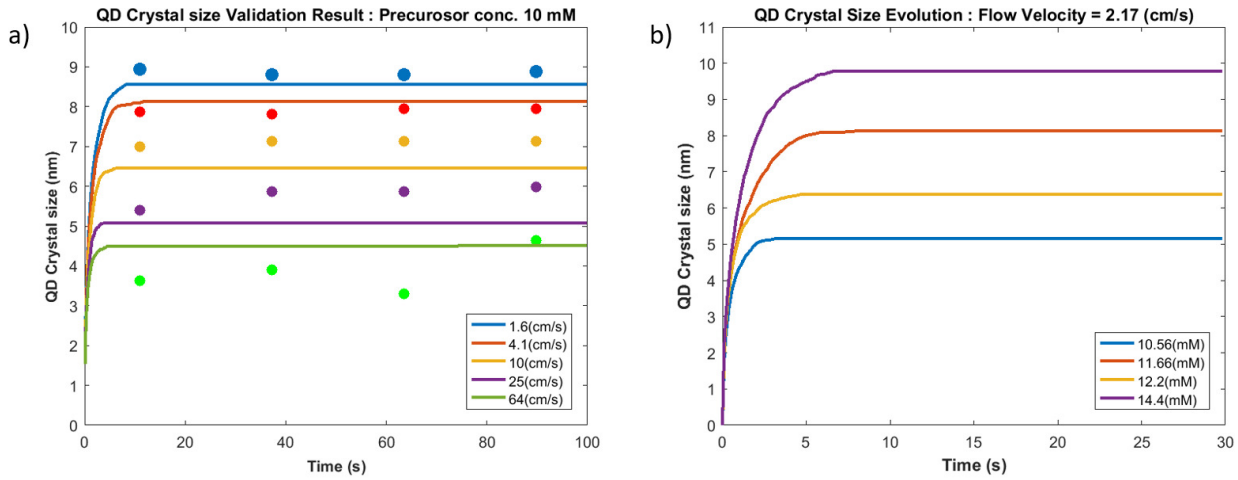


Figure 2.3: (a) Validation results for the proposed KMC simulation, where the solid line represents the KMC simulation and the scatter plot represents the experimental results [1], and (b) KMC simulation results for varying precursor concentrations at a constant superficial flow velocity of 2.17 cm/s.

Figure 2.3a the KMC simulation and the experimental observations at a precursor concentration of 10 mM and varying superficial flow velocities. It is evident from the validation results that the proposed KMC simulation captures the underlying crystallization phenomenon and predicts the experimental observations well (i.e., error is in the range of 2 % to 15 %). More importantly,

Figure 2.3 suggests that QD crystal size can be effectively controlled by manipulating the precursor concentration and superficial flow velocity.

## 2.3 Optimal Operation of PFC

Thus, for establishing a PFC for continuous QD manufacturing, it is paramount to determine the values of $C_o$ and $v_o$ to achieve a minimal offset from the set-point value for $r_{final}$ (i.e., the desired QD size). The formulation shown below presents an optimization problem to compute the optimal inputs, $C_o$ and $v_o$, for a desired $r_{final}$ value.

$$
\begin{aligned}
\underset{C_o, v_o}{Minimize} \quad & \left(r_{final} - r_{final,sp}\right)^2 + \lambda u^2 \\
\text{s.t} \quad & 5 < C_o(t) \leq 15 \; (mol/m^3) \\
& 0.05 < v_o(t) \leq 10 \; (cm/s) \\
& \frac{\partial C(t,z)}{\partial t} = -v_z \frac{\partial C(t,z)}{\partial z} - \rho_s n_s 4\pi r^2(t,z) G_r(C(t,z), v_z, r(t,z))
\end{aligned}
\tag{2.6}
$$

where $r_{final,sp}$ is the desired QD crystal size, $u$ is a vector of input variables ($C_0$ and $v_o$), and $\lambda$ is the input regularization parameter. The optimizer in Equation 2.6 is subject to certain constraints, which limits the values of $C_o$ and $v_o$ to realistic values which can be achieved in an experimental setup [1, 131]. Unfortunately, $G_r(C, v_z, r)$ is obtained by the computationally expensive KMC model, making it infeasible for the optimizer to perform multiple iterations to procure a feasible solution. Thus, we use an artificial neural network (ANN) to mimic the developed kMC model to increase the efficiency of the optimizer. Next, we can combine the kMC-mimicking ANN with the PDE for concentration balance to develop an ANN-based hybrid model that can efficiently describe the dynamics in a PFC.

### 2.3.1 ANN Architecture and Training

An ANN with three inputs (i.e., $C(t,z)$, $v_z$, and $r(t,z)$), a single output, $G_r(C, v_z, r)$, and two hidden layers has been developed. The input data comprise of the KMC simulation results of QD crystal growth for varying precursor concentrations and superficial flow velocities, which are averaged over 10 kMC trials. Various ANN architectures with two hidden layers and different numbers of neurons were tested, and it was observed that ANN with 20 neurons gave the least validation error of 0.0011 along with a testing error of 0.0095. Accordingly, Figure 2.4 shows the comparison between the proposed ANN, with 2 hidden layers and 10 neurons in each hidden layer, and the KMC simulation. It is evident that the ANN very well mimics the KMC simulation, and is 24000 times faster than the kMC.

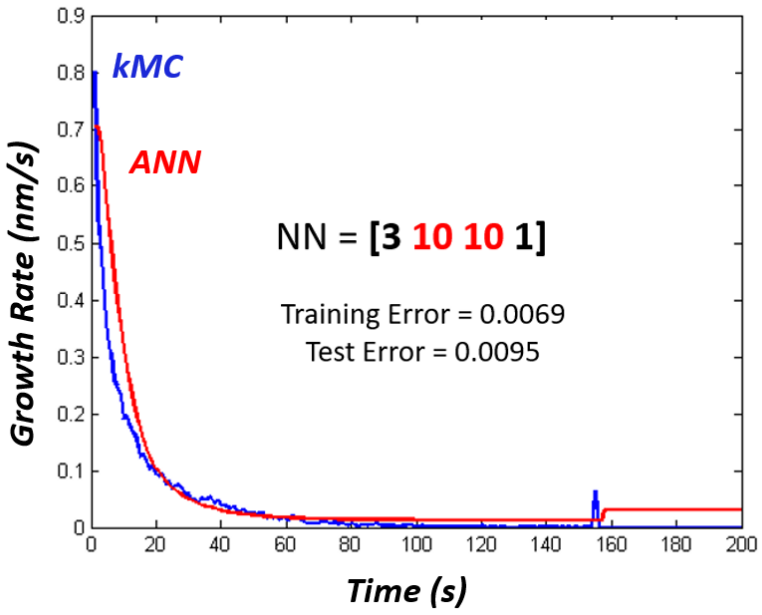


Figure 2.4: (a) Learning curve for ANN training, which shows that ANN with 2 hidden layers, each with 10 neurons, has the least validation error, and (b) comparison of the trained ANN and KMC simulation.

As mentioned earlier, the resulting ANN model simulates the computationally heavy kMC process in an expedited manner, and thus, it can be integrated with the discretized version of the

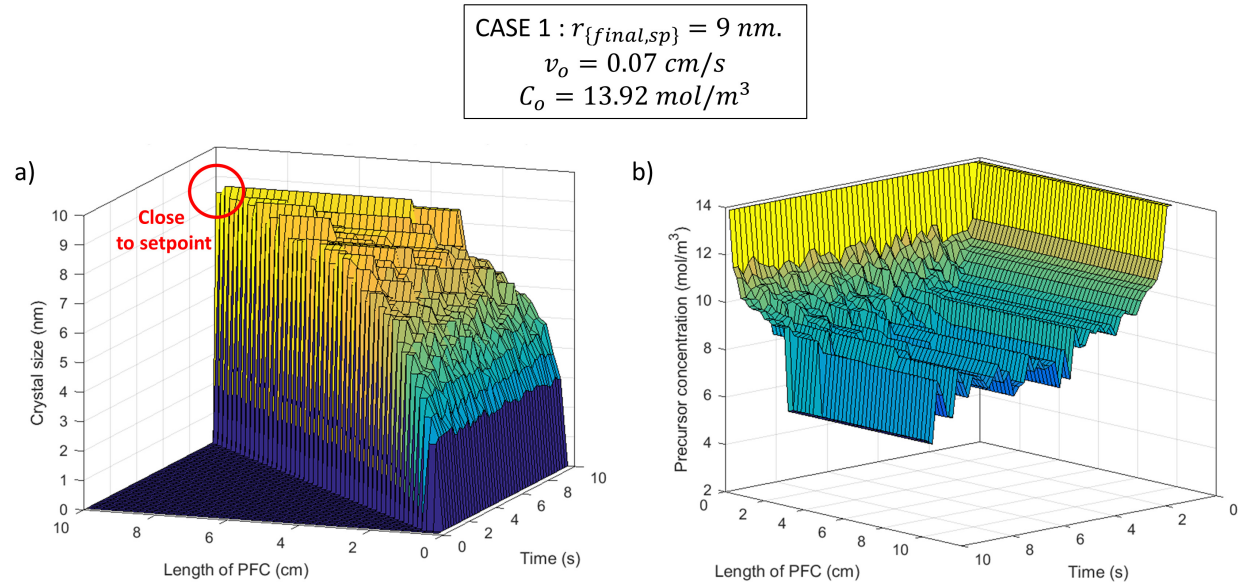


Figure 2.5: (a) Spatiotemporal evolution of QD crystal size for the optimal operation of the PFC for a set-point value of 9 nm, and (b) precursor concentration profile for the optimal operation of the PFC. The relative deviation from the set-point value is $\sim 6.1$ %.

concentration balance to develop a simple ANN-based hybrid model for the PFC.

### 2.3.2 Results for QD Size Control

Figure 2.5a shows the QD crystal size evolution in the PFC under optimal operation mode with a setpoint of 9 nm. Near the entry of the PFC, and for the first 2-3 seconds, the QD crystals grow very rapidly before they gradually saturate to terminal size, $r_{final}$, towards the end of the PFC. Initially, the large precursor concentration and absence of a ligand-shell give a boost to fast crystal growth, and then as precursor concentration drops and ligand-shell formation takes place, the QD crystal growth ceases and reaches a terminal value. Specifically, the relative deviation between $r_{final}$ and the set-point value is $\sim 6.1$ %. Figure 2.5b shows the precursor concentration profile in the PFC. Initially, the precursor concentration drops significantly due to the rapid crystal growth, and then it saturates to a stable value. This happens simultaneously with the QD size saturation (Figure 2.5b); because if the QD crystals cease to grow any further, additional precursors are not consumed, thereby stabilizing the precursor concentration towards the end of the PFC.

## 2.4 Conclusions

Inspired by a recent investigation of $CsPbBr_3$ QDs, a macroscopic model of PFC was modeled. Specifically, a first-principled KMC model was presented and was dynamically integrated with continuum models to formulate a multiscale model for a PFC. The KMC model was validated with relevant experimental observations to ensure model fidelity. The simulation results suggested that precursor concentration and superficial flow velocity could be manipulated to fine-tune the QD size at the end of the PFC. Thus, an optimal operation framework was proposed for set-point tracking in a PFC. To achieve quick computations in the optimizer, an ANN was proposed as a surrogate model for the high-fidelity KMC simulation. Lastly, open-loop operation was successfully demonstrated with a relative deviation of $< 10$ % from the set-point values. Moreover, the proposed PFC can be continuously operated and optimally controlled to produce $CsPbBr_3$ QDs of a desired size at a rate of 2-4 ml/min, thereby circumventing the problem of low production volume, which is prevalent in the conventional flask-based synthesis of perovskite QDs.

# 3. MULTISCALE MODELING OF SLUG FLOW CRYSTALLIZERS (SFC) FOR QD PRODUCTION*

The previous chapter focused on the development of a high-fidelity multiscale model for continuous crystallization of QDs using a PFC, and subsequent control of QD size using an ANN-based optimal operation framework. This concept of tubular crystallization can be extended to two-phase slug flow crystallizers (SFCs), which can provide access to larger control space by manipulation of three process inputs (i.e., gas and liquid velocity, and solute concentration). However, there is a scarcity of models which accurately describe slug flow crystallizers (SFCs) by considering (a) the existence of a stable slug regime, and (b) considering the effect of slug-to-slug (S2S) variation on CSD. To address the aforementioned two challenges, we developed an ANSYS Fluent-based computational fluid dynamics (CFD) model to accurately investigate the complexity associated with an SFC. The CFD model was capable of finding a stable slug flow regime in an SFC and analyzing the S2S variation. Further, the slug variation results from the CFD simulation were fed to a slug crystallizer model which combines a continuum and a kinetic Monte Carlo (kMC) model. The proposed CFD-based multiscale model (i.e., CFD + continuum + kMC) was used to investigate the effect of slug-variation on CSD in a SFC and underlined the need of minimizing this effect. Thus, an optimization problem was formulated to find the optimal operating condition for the SFC, which will provide good set-point tracking performance while maintaining a narrow CSD. Overall, (a) the CFD model was able to capture the phenomenon of S2S variation, and the CFD results were fed to the slug crystallizer model that successfully described the crystallization of QDs in a SFC, and (b) the optimal operation framework exhibited good set-point tracking performance. More details about this chapter are presented in our previous work.

*Content of this chapter was published in the Industrial & Engineering Chemistry Research Journal [149], and copyright permission from the journal has been granted for inclusion in the dissertation. All the figures in this work are adapted from the abovementioned journal publication.

## 3.1 CFD-based Multiscale Modeling of SFC

### 3.1.1 Process Description

Recently, a millifluidic SFC platform was used to fine-tune the size of QDs by manipulating the slug flow velocity and the precursor concentration [27, 150]. Here, the alternating air-liquid slugs are achieved when SFC is operated in a stable slug regime. In this scenario, it was observed that each liquid slug acts as an independent batch crystallizer while the overall SFC can be continuously operated. Based on these recent developments, in this work, we consider a SFC as shown in Figure 3.1. The pipe diameter and length are set to be 1.5 mm and 100 cm, respectively. Also, it has an L-shaped junction which has two inlets, one for nitrogen, and the other for the precursor solution. Furthermore, the velocity of gas (nitrogen), $v_{gas}$, and velocity of liquid (toluene), $v_{liq}$, are adjusted to investigate the existence of a stable slug flow regime.

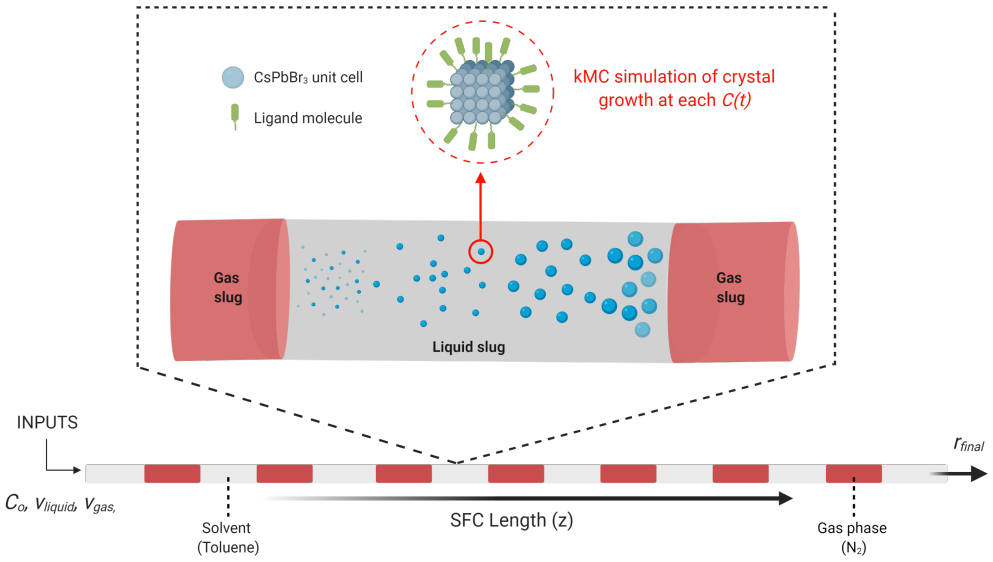


Figure 3.1: Schematic illustration of the multiscale phenomena taking place in a SFC. The blue spheres represent the QD crystals growing along the flow direction, and the green extensions around the crystal represent the ligand molecules.

### 3.1.2 CFD Modeling of Two-phase Slug Flow

While there exists a plethora of methods for modeling two-phase immiscible fluids, the volume of fluid (VOF) is the most common method [151]. Due to its superior ability to track topological changes in the interface and being naturally conservative, it has been widely applied to a number of different applications [152, 153].

#### *3.1.2.1 Governing Transport Equations*

Incompressible Navier-Stokes equations, which can be used to model the velocity ($u$), and pressure ($p$) for two interacting fluids with constant density, are given as follows:

$$\begin{aligned} &\frac{\partial \mathbf{u}}{\partial t} + \nabla \cdot (\mathbf{u}\mathbf{u}) = -\frac{(\nabla p + \mu \nabla^2 \mathbf{u})}{\rho} + \frac{F_{SF}}{\rho} + \mathbf{g} \\ &\nabla \cdot \mathbf{u} = 0 \end{aligned} \tag{3.1}$$

where $\mathbf{u}$ is the fluid velocity, $p$ is the pressure, $\mathbf{g}$ is the gravitational acceleration, $F_{SF}$ is the continuum surface force (CSF) vector, $\rho$ is the bulk phase density, and $\mu$ is the bulk phase viscosity. This formulation assumes an isothermal flow of two immiscible Newtonian fluids. The VOF method tracks the topological changes at the interface by creating an isocontour of a globally defined function ($\alpha$), which is defined as follows: [154, 155]

$$\frac{\partial \alpha}{\partial t} + \nabla \cdot (\mathbf{u}\alpha) = 0 \tag{3.2}$$

A detailed description of the modeling description can be found in our previous work [149], and in the appendix section.

#### *3.1.2.2 Meshing and Numerical Schemes*

The SFC was fine-meshed with triangular structured cells to ensure numerical convergence. The meshing quality, which can be assessed using various indicators like skewness and aspect ratio, is shown in Figure 3.2. Generally, an aspect ratio close to unity suggests a good quality mesh as shown in Figure 3.2c. Also, atmospheric pressure was maintained at the outlet, and a

| Parameters | Values |
|---|---|
| Density (Toluene) | 866 (kg/m$^3$) |
| Density (Nitrogen) | 1.225 (kg/m$^3$) |
| Interfacial tension (Toluene-Nitrogen) | 0.022 (N/m) |
| Mesh size | 0.1 mm |
| # of nodes in mesh | 649605 |
| # of elements in mesh | 314772 |

Table 3.1: Parameters for the ANSYS Fluent simulation.

no-slip boundary condition was used at the walls. The PISO (pressure-implicit with the splitting of operators) was used for pressure velocity coupling. And, the numerical convergence criteria for the continuity equation was set to 0.0001. Lastly, Table 3.1 presents the other details of the ANSYS Fluent simulation.

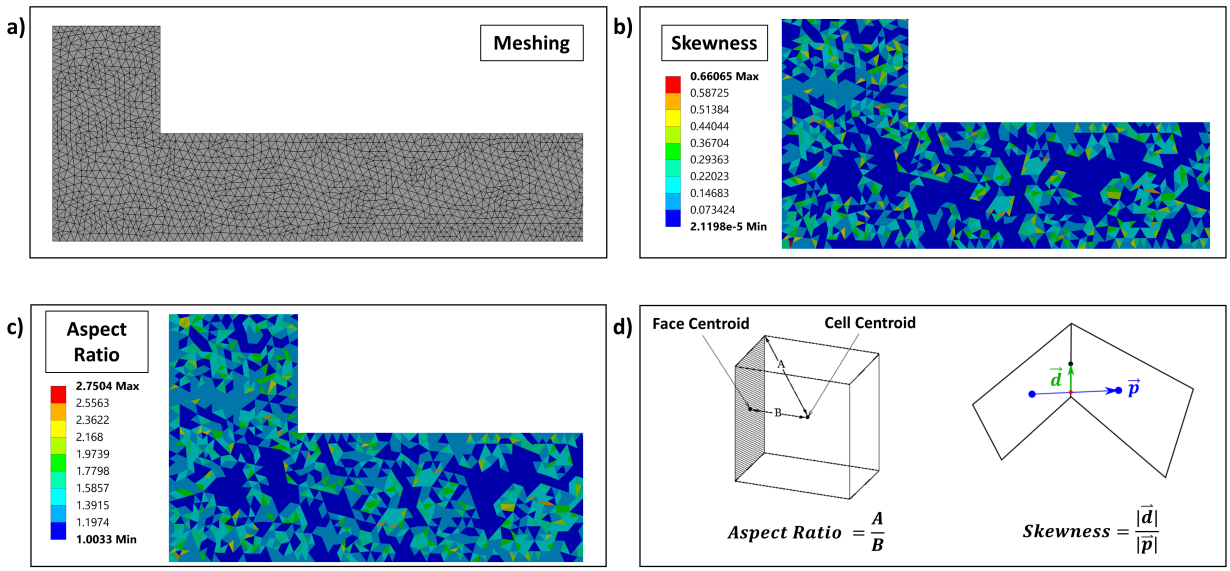


Figure 3.2: Snapshot of the ANSYS Fluent Mesh tool showing (a) triangular mesh of element size 0.1 mm, (b) distribution of skewness throughout the mesh, (c) distribution of aspect ratio throughout the mesh, and (d) illustration of skewness and aspect ratio.

### 3.1.3 Slug Crystallizer Model

#### *3.1.3.1 Macroscopic Modeling: Mass and Energy Balance*

In the stable slug regime, each liquid slug can be treated as a well-mixed mini-batch crystallizer [156, 157]. Subsequently, mass and energy balance for slug $i \in [1, N]$ can be described as follows:

$$\begin{aligned} \frac{dC(i)}{dt} &= \rho_s n_s(i,t) 4\pi r^2(i,t) G_r(i) \\ \frac{dT(i)}{dt} &= -\frac{\rho_s \Delta H_c}{\rho_f C_p} n_s(i,t) 4\pi r^2(i,t) G_r(i) - \frac{U_c a_c}{\rho_f C_p}(T(i) - T_w) \end{aligned} \tag{3.3}$$

where $r(i,t)$ is the average crystal radius in slug $i$, $C(i)$ is the precursor concentration in slug $i$, $T(i)$ is the temperature in slug $i$, $\rho_s$ is the density of $CsPbBr_3$ crystals, $\rho_f$ is the density of the solution phase (toluene), $C_p$ is the specific heat of the solution phase, $U_c$ is the heat transfer coefficient for the heating/cooling jacket, $a_c$ is the surface area of the heating/cooling jacket, $T_w$ is the temperature of the jacket wall, $n_s(i,t)$ is the number of $CsPbBr_3$ crystals in slug $i$, and $G_r(i)$ is the one-dimensional (1D) crystal growth rate in slug $i$.

#### *3.1.3.2 Microscopic Modeling: kMC Simulation*

Furthermore, since $CsPbBr_3$ QDs is a relatively new system, there is a scarcity of reliable correlations and empirical rate laws for $G_r(i)$. Therefore, it is of significant interest to develop a microscopic crystal growth model, which considers the effect of ligand-shell formation and slug velocity on $G_r(i)$. Our previous work describes the microscopic kMC crystallization model in detail, and is used to compute $G_r(i)$ [144]. Briefly, there are three major events in the KMC simulations, viz.., unit cell attachment, ligand attachment, and ligand detachment. The interplay of the aforementioned kMC events simulates the growth of QD crystals, and computes $G_r(i)$.

#### *3.1.3.3 Integration of Macroscopic and Microscopic Model*

The solution to Equation 3.3 is found by computing $G_r(i)$ for slug $i$ using the kMC simulation, which describes the microscopic phenomenon underlying $CsPbBr_3$ crystal growth. Specifically, since $C(i,t)$ and $G_r(i)$ affect each other, the kMC simulation is performed for each $t$ and slug $i$ to

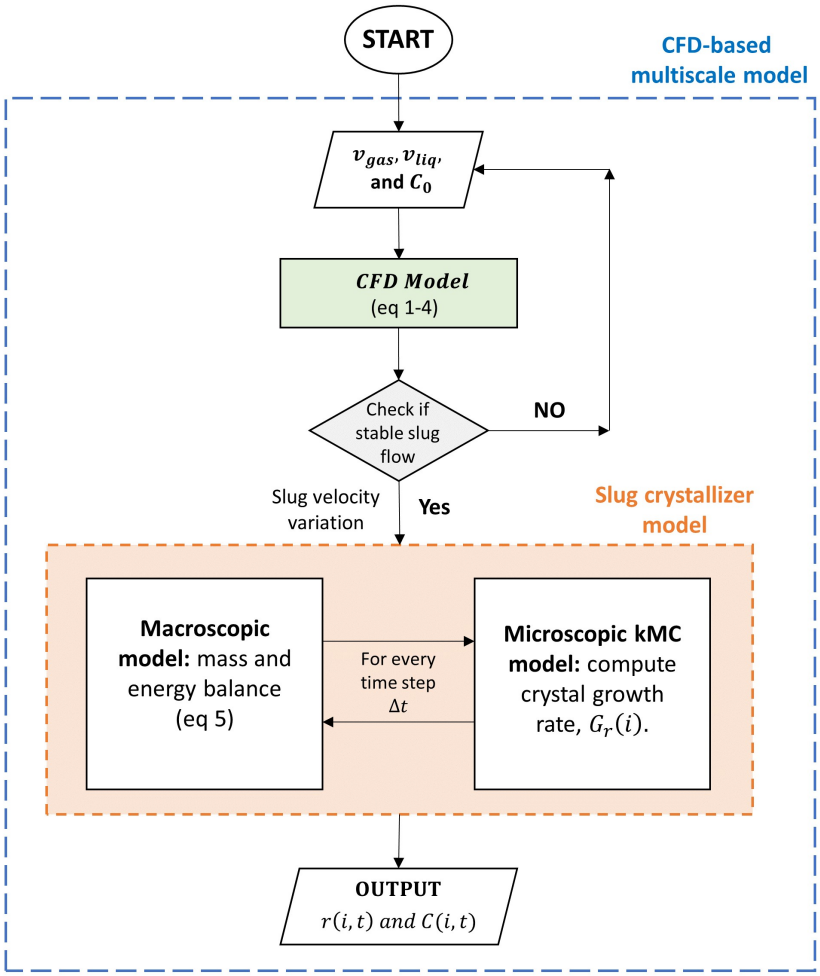


Figure 3.3: Schematic illustration of the workflow employed in the proposed CFD-based multiscale modeling framework.

accurately trace the evolution of $C(i,t)$ and $r(i,t)$ as shown in Figure 3.3. It is important to note that each slug $i$ has a slightly different slug velocity, which leads to a variation in the evolution of crystal size and precursor concentration; this variation ultimately results in a wide CSD. Lastly, the overall modeling methodology is schematically described in Figure 3.3.

## 3.2 Results and Discussion

### 3.2.1 Stable Slug Regime and Experimental Validation

To find the stable slug flow regime, CFD simulations were performed under various initial conditions (i.e., different sets of nitrogen and toluene velocities). Specifically, a grid search was performed, where the nitrogen velocity was varied from 0.01 m/s to 0.1 m/s, and the toluene velocity was varied from 0.01 to 0.04 m/s. Then the CFD results, which include the slug regime data and slug velocity, for each of these grid points was tabulated for further analysis.

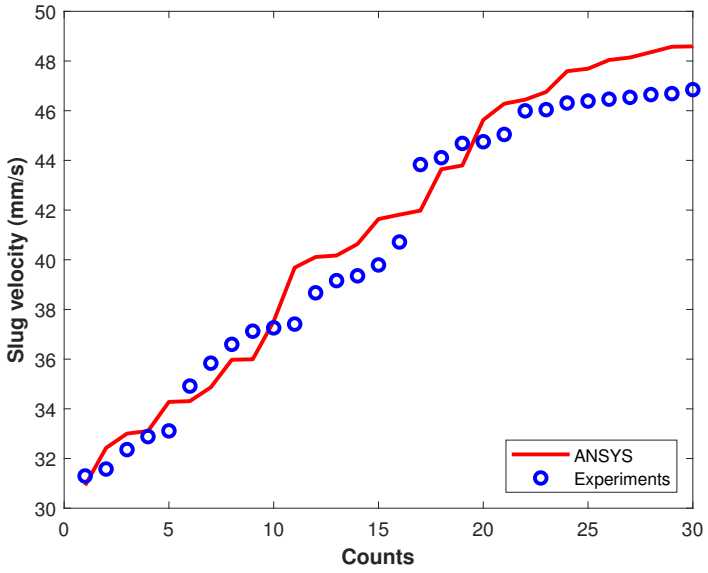


Figure 3.4: Comparison of slug velocity measured from experiments [2] and computed from the CFD simulation for a set of fluid velocities.

A stable slug flow was observed under certain initial conditions. For example, Figure 3.5 shows the temporal evolution of nitrogen volume fraction in the SFC when $v_{nitrogen}$ is 0.03 m/s and $v_{toluene}$ is 0.04 m/s. Clearly, the figure shows various steps in the formation of a stable slug flow, which are summarized in detail in our previous work [149]. To further confirm the existence of a stable slug flow, the temporal evolution of gas volume fraction at the tracer plane AB is shown in Figure 3.6.

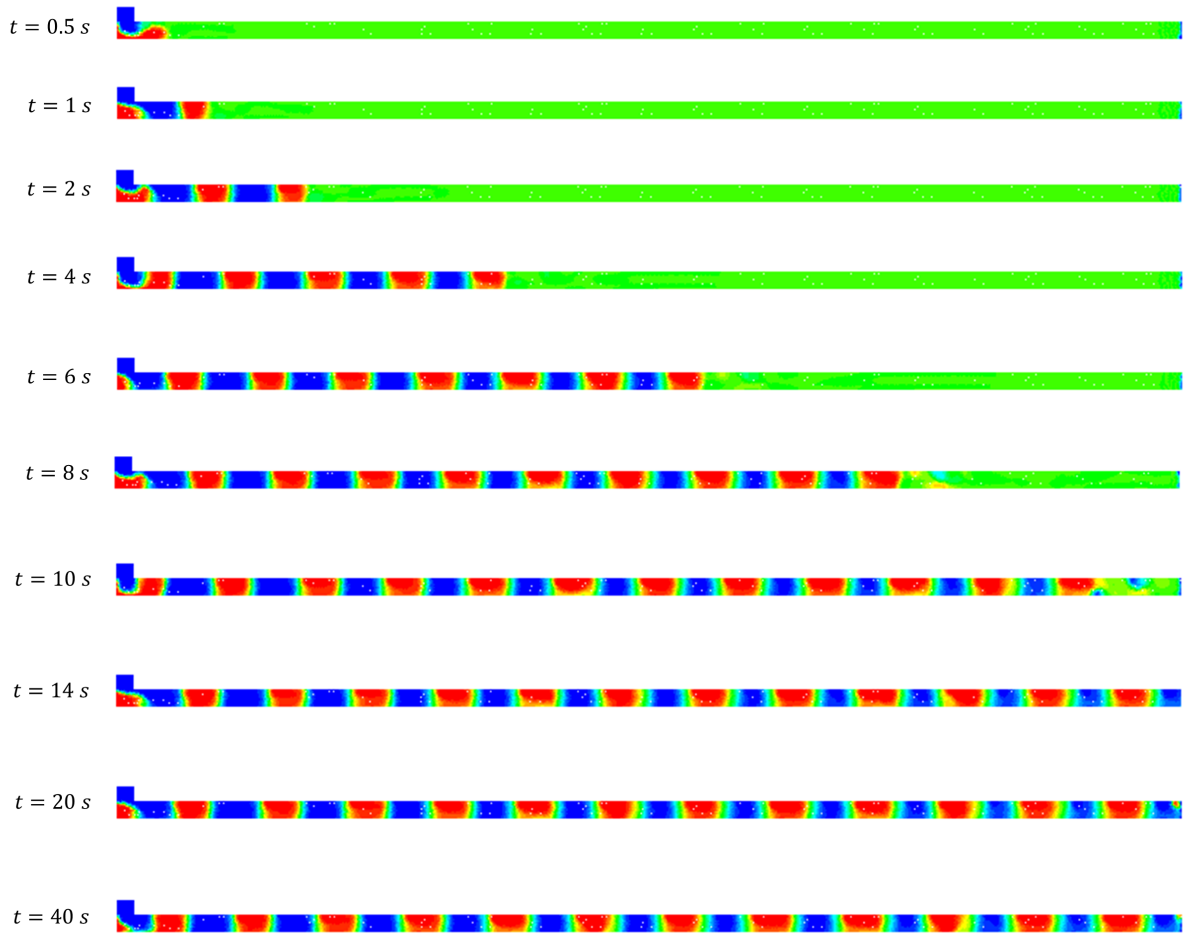


Figure 3.5: Compilation of the CFD simulation snapshots, which shows the contour of nitrogen volume fraction in the SFC. The nitrogen velocity ($v_{nitrogen}$) was 0.03 m/s, and the toluene velocity ($v_{toluene}$) was 0.04 m/s.

The oscillating amplitude ($y$ axis) in Figure 3.6 is characteristic of a stable alternating slug flow condition[154]. Specifically, gas volume fraction oscillated between a magnitude of 1 (gas slug), and 0 (liquid slug), thereby indicating the existence of alternating gas-liquid slugs.

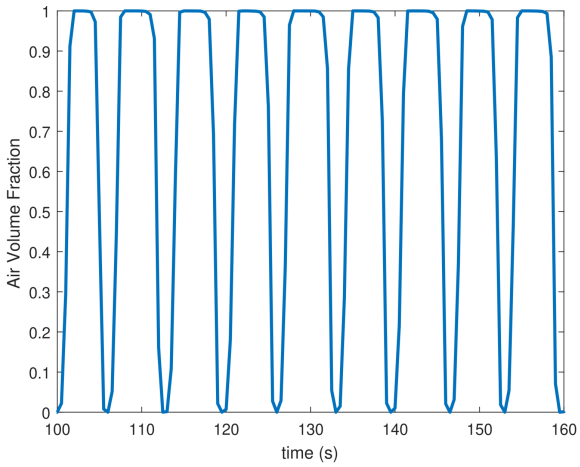


Figure 3.6: Temporal evolution of gas volume fraction in the SFC when operated at a stable slug flow condition. The gas velocity was 0.03 m/s, and the toluene velocity was 0.04 m/s.

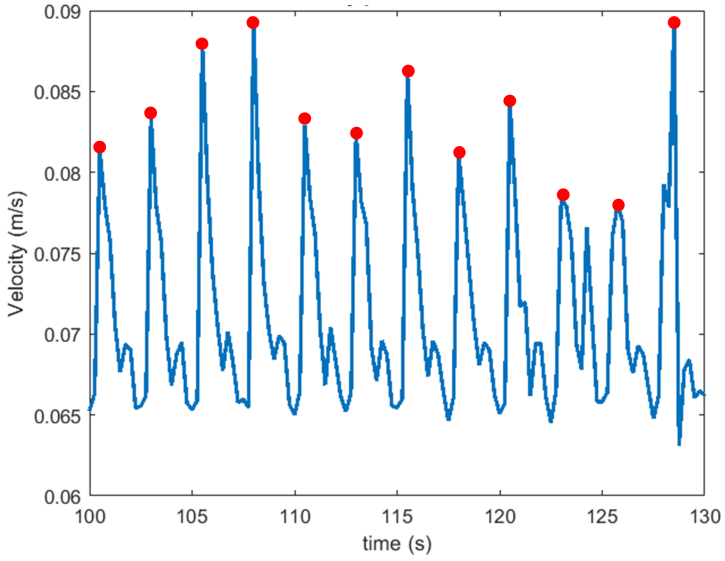


Figure 3.7: Slug velocity at the tracer plane AB showcasing the varying slug velocity for each incoming liquid slug. In this case, $v_{nitrogen}$ was 0.03 m/s and $v_{toluene}$ was 0.04 m/s.

Furthermore, to validate the proposed CFD model, the SFC was operated at a set of fluid velocities, and the corresponding slug velocities were measured experimentally. From Figure 3.4 it can be observed that ANSYS simulation mimics the experimental observations well for a set of fluid velocities (indicated by 'Counts' on $x$-axis in Figure 3.4).

### 3.2.2 Fitting Slug Velocity to Normal Distribution

The phenomenon of S2S can be observed even in the presence of a stable slug flow regime [158]. For example, Figure 3.7 shows the slug velocity peaks (i.e., $y$ axis) are slightly different for each incoming slug. Then, the slug velocity was plotted in Figure 3.8 to see if there is a certain pattern to S2S. It is evident that the slug velocity in a SFC closely follows a normal distribution, and thus, quantifies this variation.

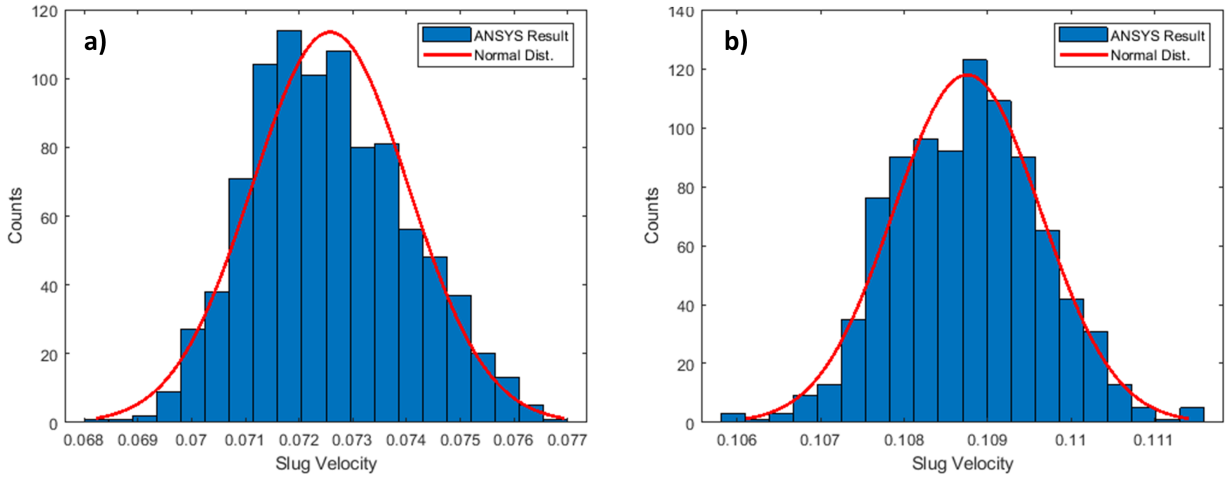


Figure 3.8: Slug velocity variation in the SFC showcasing a normal distribution for different sets of fluid velocities: (a) $v_{nitrogen}$ = 0.03 m/s, $v_{toluene}$ = 0.04 m/s, $\mu$ = 0.072 m/s, and $\sigma$ = 2.1 %; and (b) $v_{toluene}$ = 0.03 m/s, $v_{nitrogen}$ = 0.06 m/s, $\mu$ = 0.091 m/s, and $\sigma$ = 1.4 %. Here, $\mu$ represents the mean slug flow velocity, and $\sigma$ represents the standard deviation of the slug velocity.

### 3.2.3 Lookup table for Predicting Slug Velocity Variation

The previous section exhibited the existence of S2S variation and indicated that slug velocity conforms well to a normal distribution. When a similar analysis was performed for all the grid points in the fluid velocity space, it was observed that S2S follows a normal distribution with varying mean ($\mu$) and standard deviation ($\sigma$). Furthermore, the surface contour in Figure 3.9 is used in the form of a lookup table as it provides the values of average slug velocity ($\mu$), and slug velocity variation ($\sigma$) at the required set of fluid velocities. Overall, Figure 3.9 serves as a guide

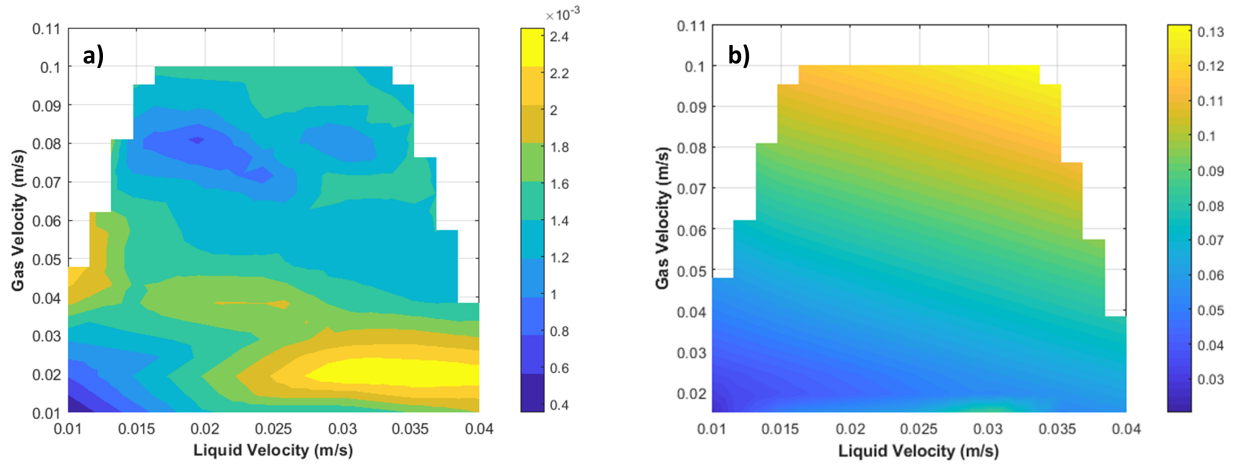


Figure 3.9: Surface contour plot showcasing the spread of (a) variation in slug velocity ($\sigma$), and (b) mean slug velocity ($\mu$) across the fluid velocity space. The region with no color corresponds to the fluid velocities at which a stable slug flow condition was not achieved.

to determine the fluid velocities which result in a minimum slug variation, and possibly lead to a homogeneous crystallization behavior across the SFC.

### 3.3 Multivariable Optimal Operation Problem

An optimization problem aimed at finding the optimal input profile (i.e., nitrogen velocity ($v_{nitrogen}$), toluene velocity($v_{toluene}$), and precursor concentration ($C_0$)), which can ensure the good set-point tracking (i.e., QD size) along with a narrow CSD, was constructed as follows:

$$
\begin{aligned}
&\underset{C_o, v_{nitrogen}, v_{toluene}}{Minimize} && (r_{final} - r_{final,sp})^2 + \lambda \sigma_{cry}^2 \\
&\text{s.t} && 5 < C_o(t) \leq 15 \; (mol/m^3) \\
& && v_{nitrogen}(t), v_{toluene}(t) \in Stable\ slug\ regime \\
& && v_{slug}(i) \in \phi(v_{nitrogen}, v_{toluene}) \\
& && \frac{\partial C(i)}{\partial t} = \rho_s n_{seed}(i) 4\pi r^2(i,t) G_r(i)
\end{aligned}
\tag{3.4}
$$

where $r_{final,sp}$ is the desired QD crystal size (i.e., set-point), $r_{final}$ is the predicted QD size at the SFC exit, $\sigma_{cry}$ is the standard deviation of CSD, $\lambda$ is the regularization parameter, which penalizes

a broad CSD, and $\phi(v_{nitrogen}, v_{toluene})$ is the normal distribution of slug velocities as described in the lookup table. Specifically, $\phi(v_{nitrogen}, v_{toluene})$ is used to generate an array of slug velocities for $N$ liquid slugs. This information is fed to the slug crystallizer model, and the crystal size evolution and precursor concentration profile are generated (Figure 3.3). Furthermore, since the solution to Equation 3.4 would require computation of crystal growth rate, $G_r(i)$, over multiple optimization iterations, the previously developed ANN [144] was utilized to increase the efficiency of the optimizer.

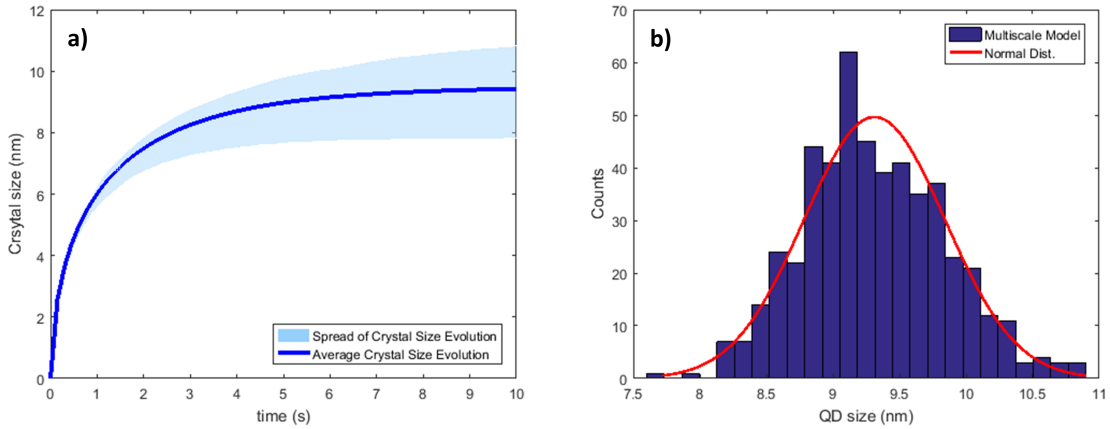


Figure 3.10: (a) Crystal size evolution of $CsPbBr_3$ QDs in SFC, and (b) CSD of $CsPbBr_3$ QDs at the SFC exit. The CSD at the SFC exit follows a normal distribution with a mean ($\mu_{cry}$) of 9.38 nm, and a standard deviation ($\sigma_{cry}$) of 5.71 %.

### 3.3.1 Optimal Operation Results

The optimal operation problem was solved for a set-point (QD size) value of 9 nm. The solution to the optimal operation problem yields a $C_0$ value of 13 mM, $v_{nitrogen}$ of 0.082 m/s, and $v_{toluene}$ of 0.022 m/s as the optimal input values, which are indeed in the stable slug regime. Feeding this input to the slug crystallizer model provides the evolution of QD crystal size with time, and the CSD at the exit of the SFC (Figure 3.10). Specifically, the average crystal size evolution in the SFC is shown in Figure 3.10a. The light blue region illustrates the variation of crystal size in $N$ different slugs and represents the evolution of QD crystal size. Figure 3.10b shows the CSD computed at

the SFC exit follows a normal distribution with a mean ($\mu_{cry}$) of 9.38 nm and a standard deviation ($\sigma_{cry}$) of 5.71 %. Furthermore, the relative deviation between $\mu_{cry}$ and the set-point value is $\sim$ 3.5 %. Also, a $\sigma_{cry}$ of 5.71 % suggests that the crystal size in $N$ different slugs is not significantly different.

### 3.4 Conclusions

This present work was motivated by the challenges faced in the operation of SFCs for continuous manufacturing of $CsPbBr_3$ QDs. Specifically, the existence of a stable slug flow regime and the effect of S2S on QD crystallization was not addressed in the literature. To tackle these challenges, a CFD-based multiscale modeling and control framework was introduced in this work. Firstly, a CFD model was used to investigate the existence of a slug regime, and quantify the variation in slug velocity under different nitrogen and toluene velocities. Then, the results from the CFD simulations were incorporated in the slug crystallizer model, which was constructed by coupling a continuum model and previously developed kMC simulation. The proposed CFD-based multiscale framework described the crystallization of QDs in the SFC, and demonstrated the effect of slug variation on CSD. Based on this modeling framework, an optimization problem was formulated to perform set-point (QD size) tracking, and to minimize the effect of slug variation on crystal growth. The optimization problem provided an optimal input profile comprising fluid velocities and inlet precursor concentration, which ensured a narrow CSD and $< 10$ % deviation from the set-point value. Thus, the present work demonstrates a CFD-based multiscale modeling and control framework for enabling fast manufacturing (i.e., 30 to 170 ml/s) of $CsPbBr_3$ QD crystals.

# 4. MODELING OF SPRAY COATING OF QDS FOR THIN-FILM APPLICATIONS*

The above two chapters focus on the construction of a multiscale modeling and control framework for enabling continuous manufacturing of QDs to meet market demands. Subsequently, these solution-processed QDs need to be converted to thin-films for application in various QD-based devices. To this end, literature studies demonstrate spray coating as a promising approach for the deposition of high-quality thin-films [48, 49]. That being said, the combination of macroscopic phenomena (e.g., transport and thermal), and surface-level interactions makes the modeling and control of spray coating a non-trivial task.

Motivated by these concerns, in this work, a spray coater is modeled using a system of macroscopic mass and energy balance equations (MEBE), which describe solvent evaporation. Then, to model the particle aggregation, the discrete element method (DEM) is utilized [159]. Specifically, the DEM considers different molecular interactions (i.e., dipole-dipole forces, Brownian motion, van der Waals forces, and circulatory flow) [160, 161]. Thus, the DEM-based model in conjunction with MEBE describes the solvent evaporation, and particle aggregation in spray coating of perovskite QDs. Furthermore, the developed model is integrated with a model predictive control (MPC) framework to regulate the film characteristics (i.e., thickness, and roughness). Specifically, the deposition rate and the spread of the spray cone are manipulated in a spray coating apparatus. More details about this work are presented in our previous work.

## 4.1 Mathematical Modeling of Thin-Film Deposition

### 4.1.1 Process Description

In this work, a spray applicator atomizes and sprays colloidal QD solution onto a heated substrate to achieve thin-film deposition as shown in Figure 4.1. Consequently, atomized droplets impinge onto the substrate and form tiny droplets followed by solvent evaporation. Furthermore,

*Content of this chapter was published in the Chemical Engineering Research and Design Journal [162], and copyright permission from the journal has been granted for inclusion in the dissertation. All the figures in this work are adapted from the abovementioned journal publication.

during solvent evaporation, the QD particles, which have a size range of $\sim$ 10 nm, undergo particle aggregation due to the presence of various molecular interactions and result in film formation [163]. Also, liquid velocity ($v_l$) and gas velocity ($v_g$), which dictate the deposition rate of atomized droplets, can be adjusted to change the thin-film deposition dynamics. Furthermore, spray nozzle height ($H_n$) can be adjusted to change the spread of deposited droplets, which follows a Gaussian distribution, $X \sim N(\mu, \sigma)$. That is to say that the density of impinging droplets decreases in a radial manner as one moves away from the center of spray applicator.

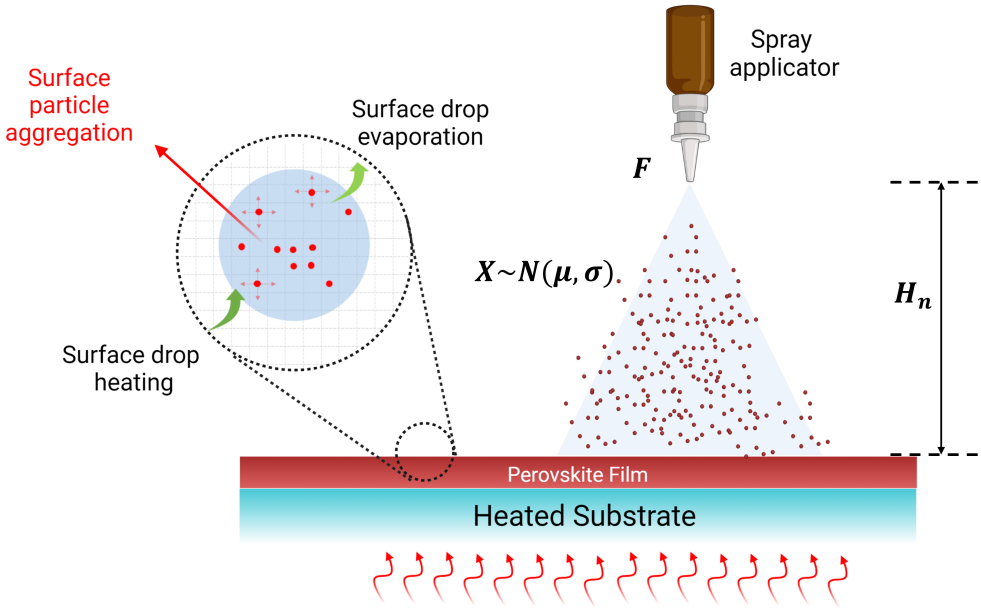


Figure 4.1: A schematic illustration of the proposed multiscale spray coating process along with a heated substrate for auto-curing of the thin film. The red dots in the magnified area are QD particles that are undergoing particle aggregation.

### 4.1.2 Macroscopic Thin-film Deposition Model

Based on the above description, the evolution of QD thin-film thickness is given as follows:

$$A_{sub} \int_0^t \frac{dh_{x,y}}{dt} = \int_0^t F(t) exp\left[-\frac{1}{2}\left(\frac{x^2+y^2}{H_n^2}\right)\right] \tag{4.1}$$

where $h_{x,y}$ indicates the film height at location $(x, y) \in L$, $A_{sub}$ is the substrate area, and $L$ represents the substrate lattice. Thus, the evolution of film thickness varies with the deposition rate ($F$), and $H_n$ across the substrate lattice. $F$ is determined by liquid velocity, and is given as $F = v_l A_{noz}$, where $A_{noz}$ is the cross-sectional area of nozzle. Furthermore, along with the deposition rate, droplet size and the distribution of droplet size are important considerations. Specifically, the ratio of air velocity ($v_g$) and liquid velocity ($v_l$) controls the droplet size distribution in a spray nozzle. Thus, to include the size variation of atomized droplets, the following correlation for two-phase gas/liquid nozzles is utilized:

$$\bar{d_s} = \frac{585}{v_g - v_l}\sqrt{\frac{\sigma_l}{\rho_l}} + 597\left(\frac{\mu_l}{\sqrt{\rho_l \sigma_l}}\right)^{0.45}\left(\frac{1000 v_g}{v_l}\right) \tag{4.2}$$

where $d_s$ is the Sauter-mean diameter (SMD) of atomized droplets, $\sigma_l$ is the surface tension of solvent, $\rho_l$ is the solvent density, and $\mu_l$ is the solvent viscosity. Also, to include droplet-to-droplet size variation, atomized droplets are assumed to have a Gaussian distribution as shown below:

$$d_i = N_d(SMD, \sigma_d) \tag{4.3}$$

where $d_i$ indicates the diameter of an arbitrary droplet, and $\sigma_d$ is the standard deviation of the droplet size around SMD. Lastly, the quality of thin-film was calculated using the root-mean-square error-based roughness ($\psi_{RMSE}$) of thin-film, which is defined as follows:

$$\psi_{RMSE} = \sqrt{\frac{1}{L}\sum^{L}\left(h_{x,y} - \bar{h}\right)^2} \tag{4.4}$$

where $\bar{h}$ is the average film height, and $L$ represents all the lattice points on the substrate.

### 4.1.3 Surface-level Droplet Evaporation

Consider droplets of radius $R_d$ that are now stationary on the substrate surface as shown in Figure 4.2, and a diffusion-controlled droplet evaporation dynamics is considered as shown below [161]:

$$\frac{dm}{dt} = -4\pi R_d D_g \left(\rho_{g,R_d} - \rho_{g,\infty}\right)$$
$$\rho_{g,R_d} = P_{sat}/R_{gas}T \tag{4.5}$$

where $m$ is the total mass of evaporating droplet, $R_d$ is the radius of droplet, $D_g$ is the gas-vapor mutual diffusion coefficient, and $\rho_{g,R_d}$ and $\rho_{g,\infty}$ are the solvent vapor concentration ($kg/m^3$) at the surface and ambient condition, respectively. Also, $P_{sat}$ is the saturation pressure of toluene at temperature $T$. Additionally, the temperature evolution of droplets needs to be monitored by defining an energy balance equation across droplets as follows:

$$\rho_s C_p \frac{dT}{dt} = \pi R_d^2 \lambda (T_s - T) + \Delta H_L \frac{dm}{dt} \tag{4.6}$$

where $T$ is the droplet temperature, $\lambda$ is the heat transfer coefficient, and $C_p$ is the heat capacity of solvent.

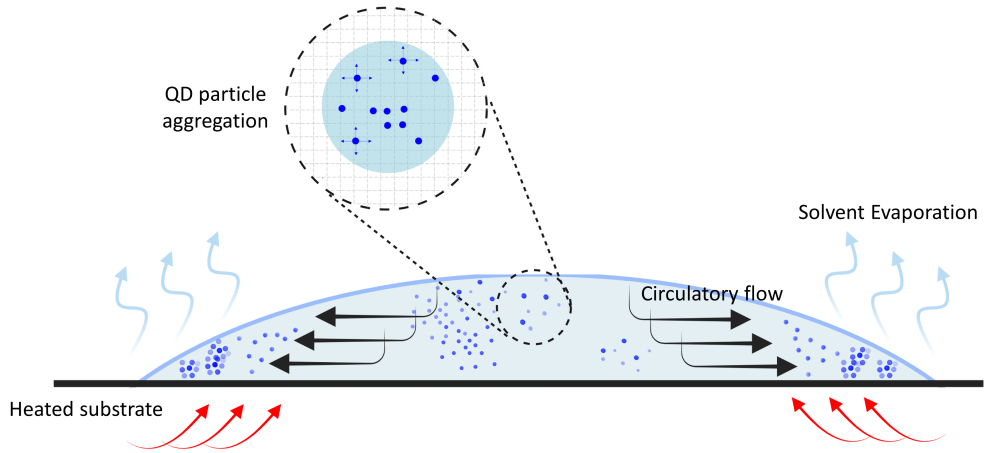


Figure 4.2: A schematic illustration of the evaporating droplet is considered in this work. The blue dots in the magnified area are QD particles within each atomized droplet.

### 4.1.4 Surface-level QD Particle Interactions

Atomized spray droplets impinge onto the heated substrate and undergo evaporation, and simultaneously, the QD particles within the droplets undergo particle aggregation as shown in Fig-

ure 4.2 due to the influence of various molecular interactions. Thus, to accurately describe the microscopic dynamics of this phenomenon, a DEM model is developed. In the model, the resultant force on each QD particle in the system is computed in accordance with Newton's law of motion, which is used to update the position of that QD particle as shown below:

$$m_p \frac{dv_p}{dt} = F = f_d + f_{vdW} + f_b + f_c \tag{4.7}$$

where $m_p$ is the mass of a single QD particle, $v_p$ is the instantaneous particle velocity, $f_d$ is the dipole force, $f_{vdW}$ is the van der Waal's force, $f_b$ describes Brownian motion, and $f_c$ represents the circulatory flow in an evaporating droplet. After computing the resultant force on each QD particle, the instantaneous velocity and displacement of the QD particle are calculated in the $x$ and $y$ directions, and given as follows:

$$\begin{aligned} X^i_{t+\Delta t_s} &= X^i_t + \Delta t_s v^i_{x,t} \; ; \quad v^i_{x,t} = (F^i_x/m_p)\Delta t_s \\ Y^i_{t+\Delta t_s} &= Y^i_t + \Delta t_s v^i_{y,t} \; ; \quad v^i_{y,t} = (F^i_y/m_p)\Delta t_s \end{aligned} \tag{4.8}$$

where $X^i$ and $Y^i$ represent the position of the $i^{th}$ QD particle in the Cartesian space, and $\Delta t_s$ is the microscopic simulation time-step. Also, $v^i_x$ and $v^i_y$ are the instantaneous velocity of the $i^{th}$ QD particle in the $x$, and $y$ directions, respectively. Finally, a schematic illustration of the computation of the resultant force on a particular QD particle is shown in Figure 4.3.

#### *4.1.4.1 Brownian Motion*

The QD particles are in the size range of 5-20 nm, and at this length scale, Brownian motion becomes a dominant transport mechanism. The stochasticity of Brownian motion is effectively captured by Gaussian white noise, which is given as follows [159]:

$$f_B = \xi \sqrt{\frac{12\pi R \mu_l k_B T}{\Delta t_s}} \tag{4.9}$$

where $R$ is the radius of QD particles, $k_B$ is the BoltzmDNN constant, and $\xi \in (0, 1]$ is a random number.

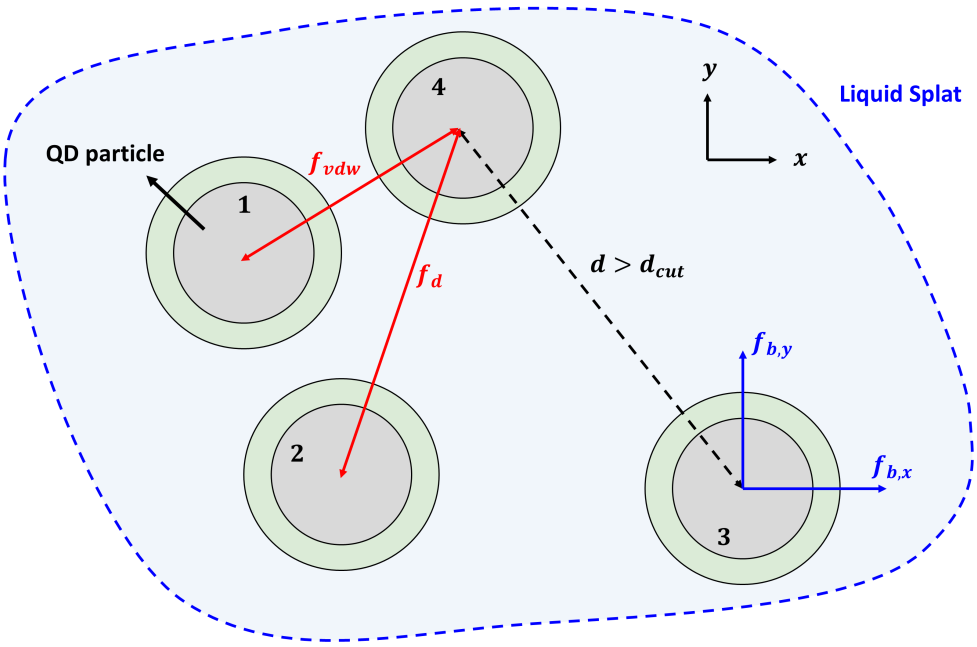


Figure 4.3: A schematic illustration of resultant force calculation in the developed microscopic DEM model. Here, $d_{cut}$ is the cut-off distance, after which the strength of molecular interactions is negligible, and $d$ is the distance between two QD particles.

#### *4.1.4.2 van der Waal's Interactions*

At the nanoscale, it is important to consider the effect of van der Waal's force between QD particles. The van der Waal's force is inversely proportional to the distance between QD particles. This is defined using a Hamaker approximation of the van der Waal's interaction, which is given as follows [164]:

$$f_{vdw} = \begin{cases} \frac{2A_{131}}{3} R^2[d+2R] \left( \frac{1}{d^2+4Rx} - \frac{1}{[d+2R]^2} \right)^2 & \text{if } d_{cut} > d > 0.1(R+h_0) \\ \frac{R}{12} \left( -\frac{A_{232}}{d^2} + \frac{2A_{123}}{[d+h_0]^2} - \frac{A_{131}}{[d+2h_0]^2} \right) & \text{if } d < 0.1(R+h_0) \end{cases} \tag{4.10}$$

where $d$ is the distance between two QD particles, $R$ is the radius of the QD particle, and $h_0$ is the equilibrium length of the ligand. $A_{131}$, $A_{123}$, and $A_{232}$ are the Hamaker constants for $CH_3NH_3PbX_3$ QDs, n-octylamine (ligand), and toluene (solvent), respectively [164].

#### 4.1.4.3 Dipole Interactions

Due to the asymmetric distribution of electron cloud within QD particles, a significant dipole moment is found for the family of QD particles (i.e., CdTe, CdSe, $CsPbX_3$, $MAPbX_3$) [165, 166]. The literature suggests that the dipole force between two QD particles can be defined as follows [164]:

$$f_d = \frac{\mu_{12}^2 C_1^2}{4\pi\epsilon_0\epsilon_{eff}} e^{-\kappa d}\left[\frac{6}{d^4} + \frac{6\kappa}{d^3} + \frac{3\kappa^2}{d^2} + \frac{\kappa^3}{d}\right] \tag{4.11}$$

where $\mu_{12}$ = $1.18 \times 10^{-26}$ Cm is the dipole moment of the two interacting QD particles, $\epsilon_0$ is the dielectric constant for vacuum ($8.854 \times 10^{-12}$ $Fm^{-1}$), $\epsilon_{eff}$ is the relative permittivity of solvent, $1/\kappa$ is Debye screening length, and $C_1$ is a proportionality constant.

#### 4.1.4.4 Circulatory Flow

Another important microscopic force that needs to be considered is circulatory flow. Experimental observations suggest that the degree of solvent evaporation near the contact line (i.e., edge of the evaporating droplet) is higher than that at the center [167, 168]. Further, Deegan and coworkers advocated that this phenomenon results in a diffusive gradient from the center to the periphery of droplet [169]. This preferential flow also carries the solute (i.e., QD particles in our case) to the periphery of the droplet leading to preferential deposition of solute at the droplet edge. To provide a mathematical expression of this phenomenon, Hu and Larson defined an analytical expression to compute circulatory flow velocity as shown below [170]:

$$\bar{v}_r = \frac{3}{8\bar{r}}\left(\frac{1}{1-\bar{t}}\right)\left[(1-\bar{r}^{-2})^{-\lambda_0}\right]\left[\frac{\bar{z}^2}{\bar{h}^2} - \frac{2\bar{z}}{\bar{h}}\right] + \frac{\bar{r}h_0^2\bar{h}}{R_0^2}\left[\bar{J}\lambda_0(1-\bar{r}^{-2})^{\lambda_0-1}+1\right]\left[\frac{\bar{z}}{\bar{h}} - \frac{3\bar{z}^2}{2\bar{h}^2}\right] \tag{4.12}$$

where $\bar{v}_r = v_r t_f / R_d$ is the dimensionless circulatory flow velocity, $\bar{t} = t/t_f$ is the dimensionless evaporation time, $\bar{z}/\bar{h}$ is the dimensionless droplet height, $t_f$ is the total time for complete evaporation of droplet, $\bar{J}$ is the dimensionless evaporation rate, $\bar{r}$ is the dimensionless droplet

radius, and $\lambda_0$ is the modified contact angle.

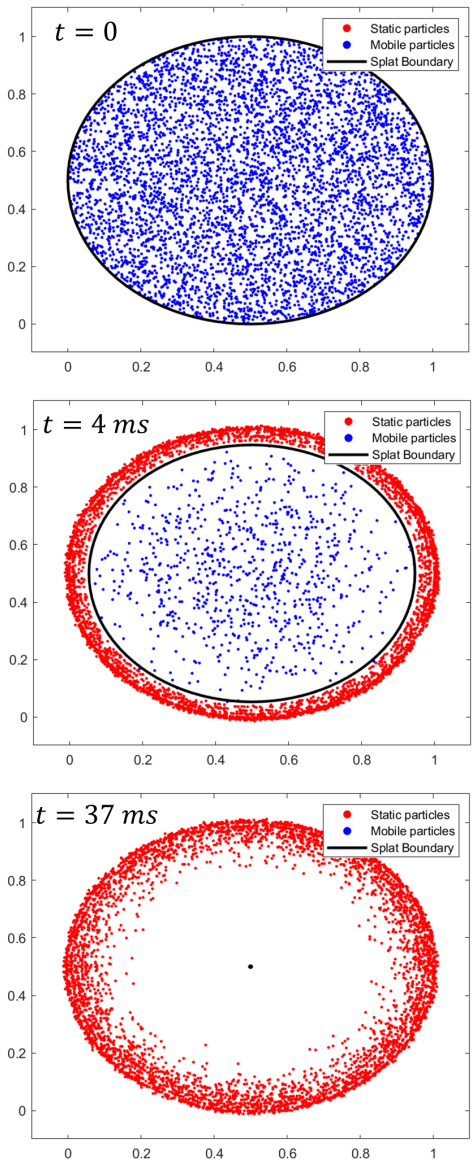


Figure 4.4: Simulation snapshots of the surface-level spatiotemporal evolution of deposition of QD particles. The blue-colored () QD particles are termed as mobile particles and are within the bulk of the evaporating drop. The red-colored QD particles () are static particles. The black boundary indicates the receding radius of the evaporating drop. Here, $T_s$ is 100°C, and the droplet size is 100 $\mu$m.

### 4.1.5 Multiscale Thin-film Deposition Model

Next, various aspects of the film-deposition process are combined together as shown in Figure 4.5. Specifically, (a) thin-film deposition equations; (b) droplet size distribution data; (c) evaporation dynamics; and (d) information from the surface-level particle interactions are integrated to construct a multiscale thin-film deposition model.

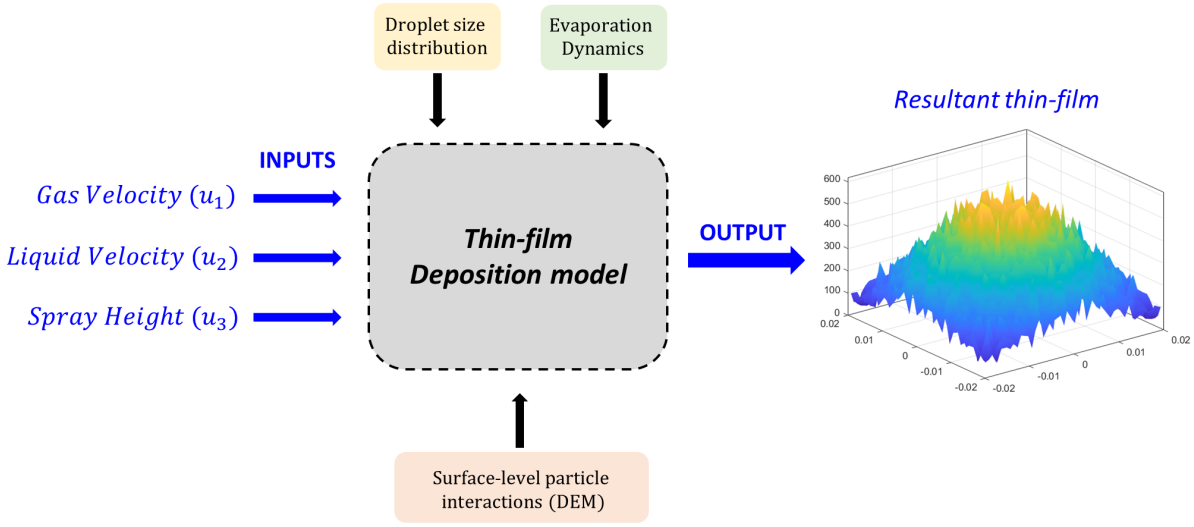


Figure 4.5: Schematic illustration of the multiscale thin-film deposition framework developed in this work.

## 4.2 Simulation Results

### 4.2.1 Surface-level Particle Aggregation

As mentioned earlier, it is important to elucidate the surface-level deposition pattern of QD particles. The DEM-based model of an evaporating QD solution droplet was simulated for a representative impinging droplet with a size of 100 $\mu$m as shown in Figure 4.4. It can be seen that at $t$ = 0, the QD particles are randomly distributed across the droplet space, and then along with droplet evaporation, the QD particles can aggregate and move around in the QD suspension. Also, during droplet evaporation and particle aggregation, there are two competing phenomena: attractive molecular forces keep QD particles within the central bulk of the droplet, while circulatory

flow adds a velocity component in the outward radial direction and pushes QD particles towards the periphery, resulting in the coffee-ring effect (CRE) of QD particles. The uneven deposition of QD particles due to CRE contributes to the roughness of as-deposited thin films and is an important aspect to investigate [167]. Previous experimental studies agree with simulation results on the existence of the CRE [15, 171].

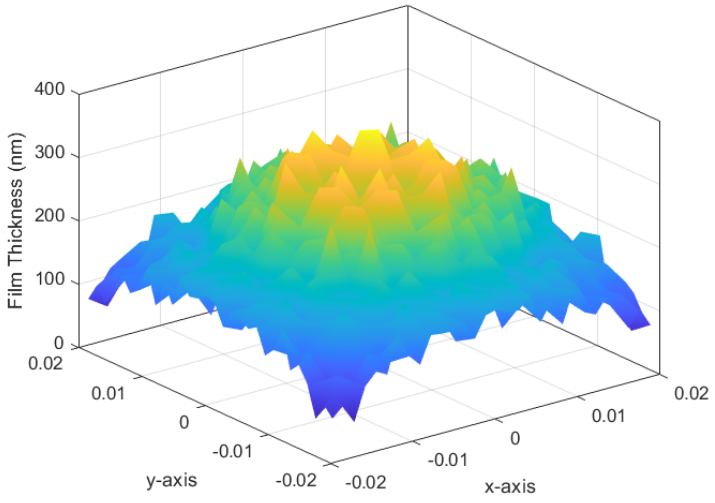


Figure 4.6: Surface evolution of the thin-film deposition when various inputs (i.e., the gas and liquid velocities, and the spray nozzle height) have arbitrary values within the operating range of the spray nozzle.

### 4.2.2 Thin-film Deposition

During spray coating, millions of QD solution droplets will be deposited using spray coating, and their combined effect will result in thin-film deposition on the substrate [172]. Specifically, Figure 4.6 shows the simulated film topography when the three inputs (i.e., gas and liquid velocities and spray nozzle height) follow an arbitrary input profile. It can be seen that thin-film deposition on the substrate is pretty uneven, with a $\psi_{RMSE}$ of $\sim$ 10 nm, variation in film thickness in the range of 100 to 250 nm, which is not suitable for direct utilization in QD-based thin-film applications as it is detrimental to the optoelectronic performance [13, 15]. Thus, there is a need to regulate

the thin-film deposition process to ensure minimized roughness and achieve the desired set-point thickness.

### 4.3 MPC Design

In order to control thin-film thickness ($h$) and film roughness ($\psi_{RMSE}$), an MPC was utilized to manipulate the input variable (i.e. gas and liquid velocity, and spray nozzle height). Since the MPC is deployed in real-time, the solution to the internal optimization problem needs to be obtained very quickly, which is not possible if we use the above-developed multiscale thin-film deposition model. Thus, a DNN is developed to significantly increase the computational efficiency of the MPC.

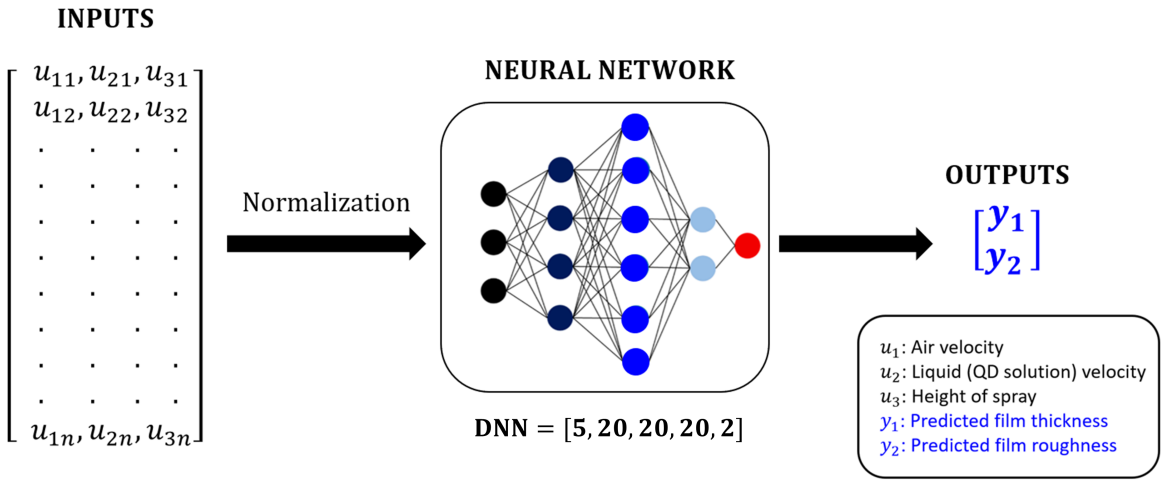


Figure 4.7: Schematic of the developed DNN showcasing the augmented input vector and the desired thin-film outputs.

#### 4.3.1 DNN Training and Testing

For this particular case, we are interested in predicting film thickness (i.e., now represented by $y_1$) and roughness (i.e., now represented by $y_2$). Here, $y_1$ and $y_2$ are dependent on various inputs (i.e., $u_1$, $u_2$, and $u_3$), and thus, the DNN shown in Figure 4.7 is sufficient to mimic the thin-film deposition process. Here, simulation data for 4000 sets of arbitrary input combinations

were collected and stored in the form of the above-mentioned augmented inputs and outputs and gave a total of 20K data points for the DNN training. Furthermore, various DNN architectures (i.e., varying hidden layers and neurons) were trained and tested, and the DNN with 5 inputs, three hidden layers with 20 neurons in each layer, and 2 outputs (i.e., [5, 20, 20, 20, 2]) gave the best training, validation, and testing performance.

### 4.3.2 MPC Formulation

Utilizing the DNN-based computationally efficient surrogate model in the previous section, an MPC can be formulated as follows:

$$
\begin{aligned}
\underset{u_1,u_2,u_3}{Minimize} \quad & \alpha_1 \left(\bar{h} - h_{sp}\right)^2 + \alpha_2 (\psi_{RMSE} - \psi_{sp})^2 \\
\text{s.t} \quad & 10 \leq u_1 \leq 20 \, (m/s) \\
& 1 \leq u_2 \leq 2 \, (m/s) \\
& 0.1 \leq u_3 \leq 0.5 \, (cm) \\
& [\bar{h}, \psi_{RMSE}] = f_{DNN}(u_1, u_2, u_3)
\end{aligned}
\tag{4.13}
$$

where $\alpha_1$ and $\alpha_2$ are the weights for the objective function, $f_{DNN}$ is the DNN, and the manipulated inputs $u_1$, $u_2$, and $u_3$ represent the gas velocity, liquid velocity, and spray nozzle height, respectively.

### 4.3.3 Closed-Loop MPC Results

For MPC demonstration a, set-point film thickness ($\bar{h}_{sp}$) of 50 nm (commonly seen in the literature [173, 16]) was considered along with the objective of minimizing the roughness. Figure 4.8 shows the compilation of the optimal input values and the resultant thin film with the desired film thickness and a minimum value of roughness. First, the variation in the gas velocity results in different droplet sizes due to atomization, and it affects the evaporation dynamics and the surface-level particle aggregation. Second, the variation in liquid velocity largely affects the deposition rate as more liquid is sprayed onto the substrate. Throughout the deposition process, the spray nozzle height is fairly consistent. However, towards the end of the process, to further minimize the

roughness of the thin film, the spray nozzle is increased significantly as it will allow a high spray cone area leading to much more even deposition and maintaining a low roughness value.

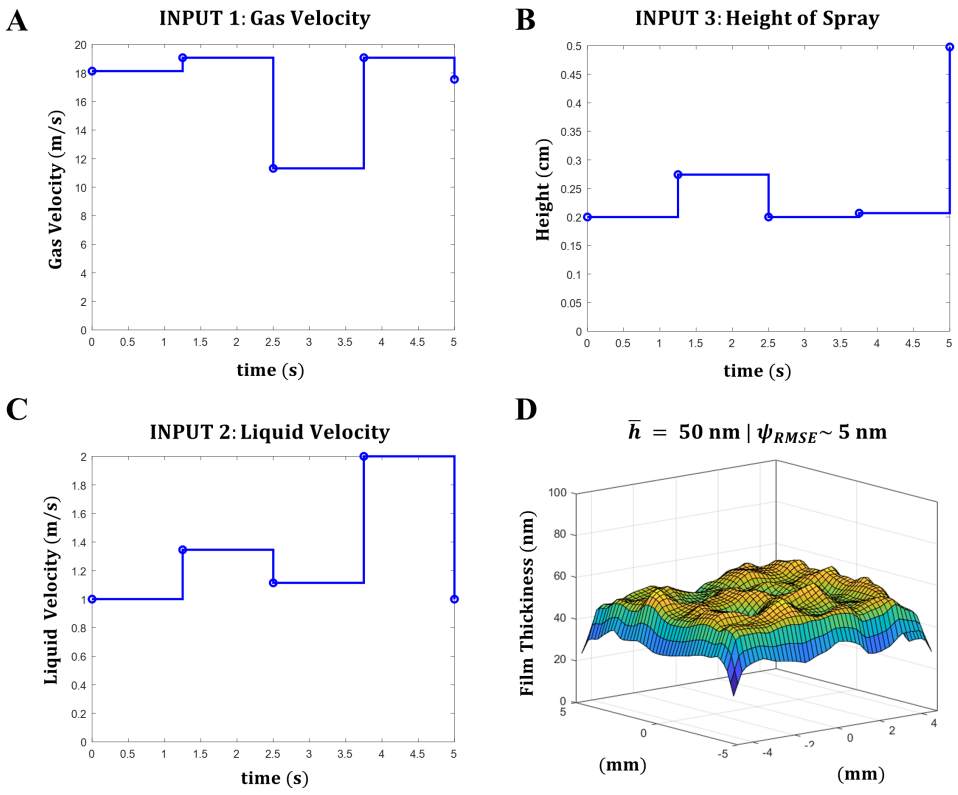


Figure 4.8: Compilation of the optimal inputs, viz., (a) gas velocity, (b) liquid velocity, (c) spray nozzle height, and the output, (d) thin-film achieved by applying the optimal inputs.

## 4.4 Conclusions

The recent interest in QD-based thin-film optoelectronic devices has probed research in the modeling and control of thin-film deposition for the manufacturing of these devices. To this end, a multiscale thin-film deposition model was developed that considers macroscopic factors and surface-level characteristics, including uneven deposition and roughness. The model integrates different factors and their individual models to construct a multiscale thin-film deposition model. Further, an MPC was designed to regulate film characteristics (i.e., thickness and rough-

ness) by manipulating various inputs, and a computationally efficient DNN-based thin-film deposition model was developed for expediting the internal computations of the MPC. The developed MPC successfully achieved set-point tracking for desired film thickness and minimized film roughness.

# 5. MODELING LIGAND CROSSLINKING FOR NANO-PATTERNING OF QDS*

The above section describes the thin-film deposition of QDs, which is essential in the manufacturing of LED displays and solar cells. However, recent studies have revealed that these thin-films are chemically facile in nature, and undergo rapid chemical deterioration when exposed to downstream chemical or mechanical processing [54]. To tackle this issue, Kang and colleagues demonstrated azide-based light-activated ligand crosslinking of QDs that interlock the neighboring QDs to make robust QD thin-films for manufacturing of high-resolution LED displays [3]. However, (a) the chemical reaction involved in the ligand crosslinking process occurs over a very short time ($<$ 1 ms), which makes probing into the kinetics and degradation mechanism during the crosslinking process difficult; and (b) the chemical robustness of the QD film varies with crosslinker composition and structure. Thus, it is imperative to develop an appropriate modeling approach to gain key insights on the crosslinking process, which will help in designing better nano-patterning techniques for the manufacture of QD thin-films in the future.

To this end, a kinetic Monte Carlo (kMC) is developed to describe the crosslinking between QD surface ligands using cross-linkable additives. Specifically, the crosslinking step is broken down into various steps (i.e., reactive radical formation and C-H insertion reaction), and is modeled using appropriate rate kinetics. In the developed kMC model, the influence of spatial ligand-crosslinking configurations is considered, and it is determined by the geometry and the structural dimensions of the crosslinker as well as the ligand spacing density. Furthermore, to perform model validation, we selected the case of azide-containing light-induced ligand crosslinkers (referred to as LIXERs) for crosslinking the ligands of CdSe QDs as an illustrative example. More details about this work are presented in our previous work.

*Content of this chapter was published in the Journal of Material Chemistry C [174], and copyright permission from the journal has been granted for inclusion in the dissertation. All the figures in this work are adapted from the abovementioned journal publication.

## 5.1 kMC Modeling of Ligand Crosslinking

### 5.1.1 kMC Lattice Description

A two-dimensional kMC model (2D-kMC) was developed to spatially and temporally trace the progress of the crosslinking reaction. Specifically, a lattice size of $N$ = 100, and periodic boundary conditions were used to represent the QD surface as shown in Figure 5.1. The ligand molecules are positioned on the 2D lattice in accordance with the ligand density. Then, the crosslinkers are randomly initialized across the entire 2D lattice, and the crosslinker density is computed based on the amount of crosslinkers added to the deposited QD film, $W_i$, which is $\%$ wt. of crosslinkers in the QD film.

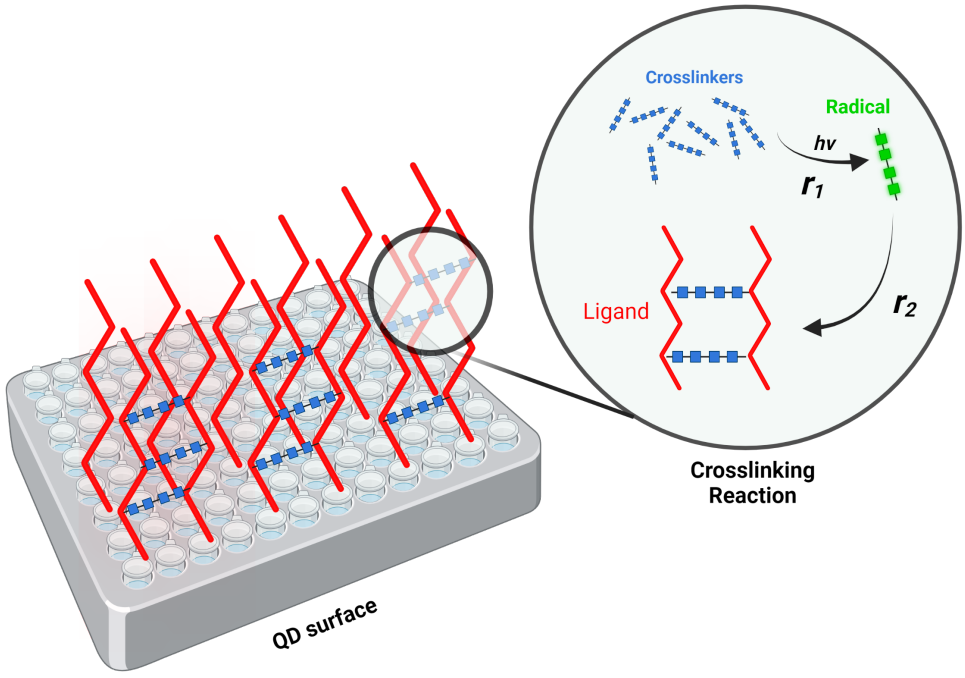


Figure 5.1: Schematic illustration of the QD surface ligands, and the crosslinked network between them.

### 5.1.2 Surface Rate Kinetics

Literature studies suggest that the crosslinking reaction occurs in two distinct steps (i.e., a radical formation step, and then a C-H insertion reaction to crosslink two ligands) [3, 175, 176]. First, the radical formation step can be initiated by photoactivation, or other precursor reactions [177, 178], and can be described by a general Arrhenius-type empirical rate expression as shown below:

$$r_1 = k_1 exp\left(\frac{-E_1}{RT}\right)[C_{CL}]^{g_1} \tag{5.1}$$

where $k_1$ represents the rate constant, $E_1$ is the activation barrier for this reaction, $g_1$ is the order of the reaction, $C_{CL}$ is the concentration of crosslinkers, $R$ is the universal gas constant, and $T$ is temperature.

Second, the activated radicals react with a suitable carbon on the alkyl chain of the surface ligands (i.e., C-H insertion reaction) [179]. Previous studies probing into the kinetics and mechanism of the C-H insertion reaction suggest that it also follows Arrhenius-type kinetics given as follows: [180, 181]

$$r_2 = k_2 exp\left(\frac{-E_2}{RT}\right)[C^*_{CL}]^{g_2} \tag{5.2}$$

where $k_2$ represents the rate constant, $E_2$ is the activation barrier for this reaction, $g_2$ is the order of the reaction, and $C^*_{CL}$ is the concentration of activated crosslinkers with a reactive radical moiety. Lastly, the total rate of all the reactions, $R_{total}$, is the summation of rates of the above-mentioned two reactions and is defined as $R_{total} = r_1 + r_2$.

### 5.1.3 Different Crosslinking Configurations

During the ligand crosslinking reaction, the activated crosslinker molecule (i.e., with an active radical), reacts with one of the carbons on the alkyl ligand chain to undergo the C-H insertion reaction. It is important to note that based on the geometry of the surface ligands, ligand density,

and the dimensions of the crosslinker, the crosslinker can bond with two ligands in various configurations as shown in Figure 5.2 and enumerated in Table 5.1. This crosslinking configuration will affect the linkage between two neighboring QDs (i.e., QD-QD crosslinking).

| Crosslinking Configuration | QD-QD crosslinking |
|---|---|
| 1 | 50% chance |
| 2 | Yes |
| 3 | No |
| 4 | Yes |
| 5 | No |

Table 5.1: Different crosslinking configurations and their effect on QD-QD crosslinking.

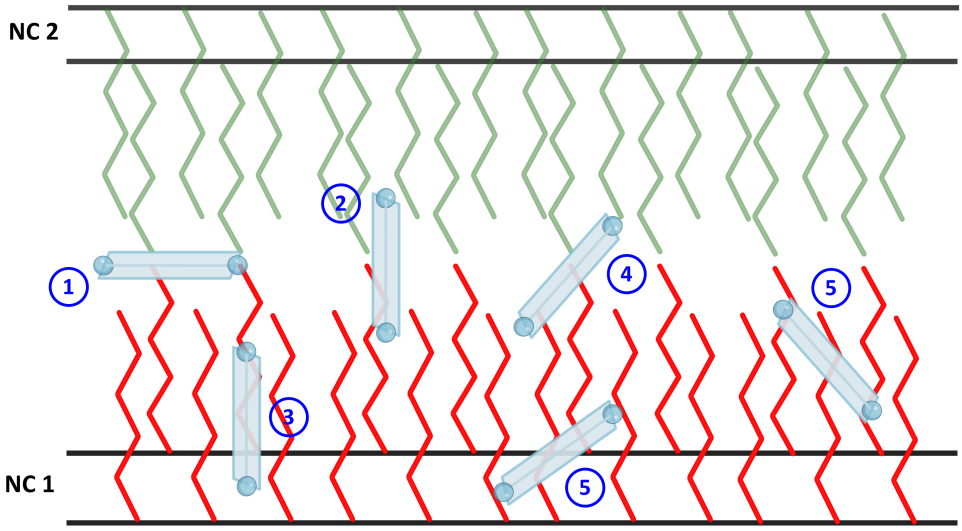


Figure 5.2: Schematic illustration of different crosslinking configurations between a crosslinker and surface ligands.

### 5.1.4 kMC Event Execution

During a kMC simulation, only one kMC event can be performed at each time instant, and the Gillespie algorithm is followed in this work [182]. Specifically, the probability of a crosslinker getting activated to form a reactive radical species is denoted by $P_1$, and the probability of the activated crosslinker reacting with carbon on the alkyl chain of the surface ligand to form a crosslinking bond is denoted by $P_2$. These probabilities are calculated as shown below:

$$\begin{aligned} P_1 &= r_1/R_{total} \\ P_2 &= r_2/R_{total} \end{aligned} \tag{5.3}$$

Then, a random number $\xi_1 \in [0, 1]$ is generated, and used in conjunction with Table 5.2 to select an appropriate kMC event. For example, if Case 2 is chosen, then an activated crosslinker molecule undergoes a C-H insertion reaction with one of the surface ligands to form a crosslinking bond. Then, to decide the crosslinking configurations, another random number, $\xi_2 \in Z^+$, is chosen to select a certain crosslinking configuration. Lastly, after every kMC event, there is a corresponding time increment, $\Delta t$, which is given by $\Delta t = \frac{-\log \xi_3}{R_{total}}$, where $\xi_3 \in (0, 1]$ is a random number.

| Cases | Probability Conditions | Event Executed |
|---|---|---|
| Case 1 | $0 < \xi_1 \leq P_1$ | Nitrene radical formation |
| Case 2 | $P_1 < \xi_1 \leq P_1 + P_2$ | C-H insertion reaction |

Table 5.2: Probability conditions for selecting a kMC event.

## 5.2 Case Study of CdSe QDs

In this work, the particular case of the azide-based ligand crosslinking of CdSe QDs is modeled, and the simulation results are experimentally validated.

### 5.2.1 Process Description

To fabricate a QD-based high-resolution electroluminescence display, a QD film consisting of QDs emitting either red (R), blue (B), or green (G) light is deposited, and this process is repeated at least three times to realize RGB patterns. However, the deposited QD films are not chemically robust, and can be blemished during the subsequent chemical steps, which is highly detrimental to the photoelectronic characteristics of these materials [183]. To resolve this challenge, azide-based light-induced ligand crosslinkers (referred to as LIXERs) for interlocking neighboring QDs to make chemically robust QD films has been demonstrated in our previous work [3]. This process is illustrated in Figure 5.3, and the precise experimental details about this process can be found in the literature [3].

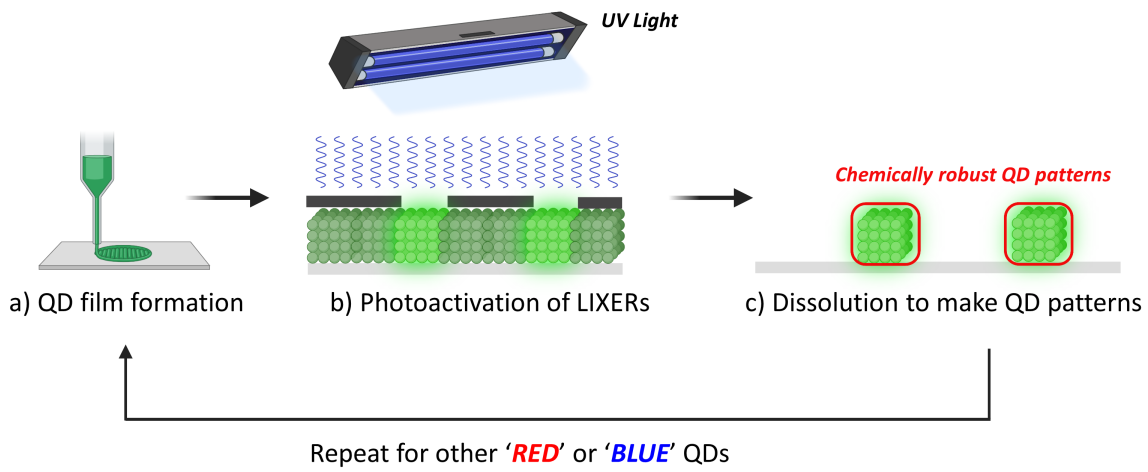


Figure 5.3: Schematic illustration of the light-induced crosslinker (LIXER)-based QD patterning process followed in this work[3].

### 5.2.2 Kinetic Parameters

The literature studies for CdSe QDs indicate that the crosslinking process follows a two-step process [3]; (1) the photoactivation of the azide moiety forms a reactive nitrene intermediate ($r_1$); and (2) the nitrene radical reacts with one of the carbons on the alkyl ligand chain ($r_2$). To this end,

a first-order C-H insertion reaction (i.e., $g$ is 1) was considered in this work along with specific reaction parameters enumerated in Table 5.3.

Furthermore, in the case of CdSe QDs, two kinds of LIXERs were studied to understand the influence of LIXER structure on crosslinking performance. The ethane-1,2-diyl bis(4-azido-2,3,5,6-tetrafluorobenzoate), which is termed as 2C-LIXER, has an ethane chain separating the two azide crosslinking arms, and octane-1,8-diyl bis(4-azido-2,3,5,6-tetrafluorobenzoate), which is termed as 8C-LIXER, has an octane chain separating them. Although these two LIXERs will have similar widths and heights, the 8C-LIXER is significantly longer than the 2C-LIXER.

| Parameters | Value | Reference |
|---|---|---|
| $k_1$ | $4.2 \times 10^6\ s^{-1}$ | Platz and co-workers [184] |
| $k_2$ | $4.5 \times 10^4$ $M^{-1}s^{-1}$ | Sundberg and co-workers [181] |
| $E_a$ | 1.8 kcal $mol^{-1}$ | Sundberg and co-workers [181] |
| Ligand Density | 3/$nm^2$ | From experiments |
| QD diameter | 13 nm | From experiments |

Table 5.3: Model parameters for the specific case of azide-based ligand crosslinking for CdSe QDs

### 5.2.3 Calculating QD-QD Crosslinking

Ligand crosslinking across neighboring QD will keep the QD film chemically interlocked and resistant. Thus, the key variable of interest in the developed crosslinking model is the percentage of QD-QD crosslinking LIXERs (i.e., the number of the LIXERs which crosslink two separate QDs to the number of the total crosslinking LIXERs), which is given as follows:

$$\eta_{QD-QD} = \frac{Number\ of\ QD\text{–}QD\ crosslinking\ LIXERs}{Total\ number\ of\ crosslinking\ LIXERs} \tag{5.4}$$

## 5.3 Results

### 5.3.1 Temporal Evolution of QD-QD Crosslinking

Figure 5.4 shows the evolution of $\eta_{QD-QD}$ for the case of 2C-LIXER and 8C-LIXER. It can be seen from Figure 5.4 that initially $\eta_{QD-QD}$ is zero, and then gradually increases and saturates to a certain value. Further, $\eta_{QD-QD}$ is larger for the case of 8C-LIXER than that for 2C-LIXER. The is because, the 8C-LIXER is longer than 2C-LIXER, and thus considering the different configurations in Figure 5.2, the 8C-LIXER can crosslink with neighboring QDs over a long distance. In simpler terms, the 8C-LIXER provides a greater probability of crosslinking two neighboring QDs than 2C-LIXER, which positively contributes to its crosslinking performance.

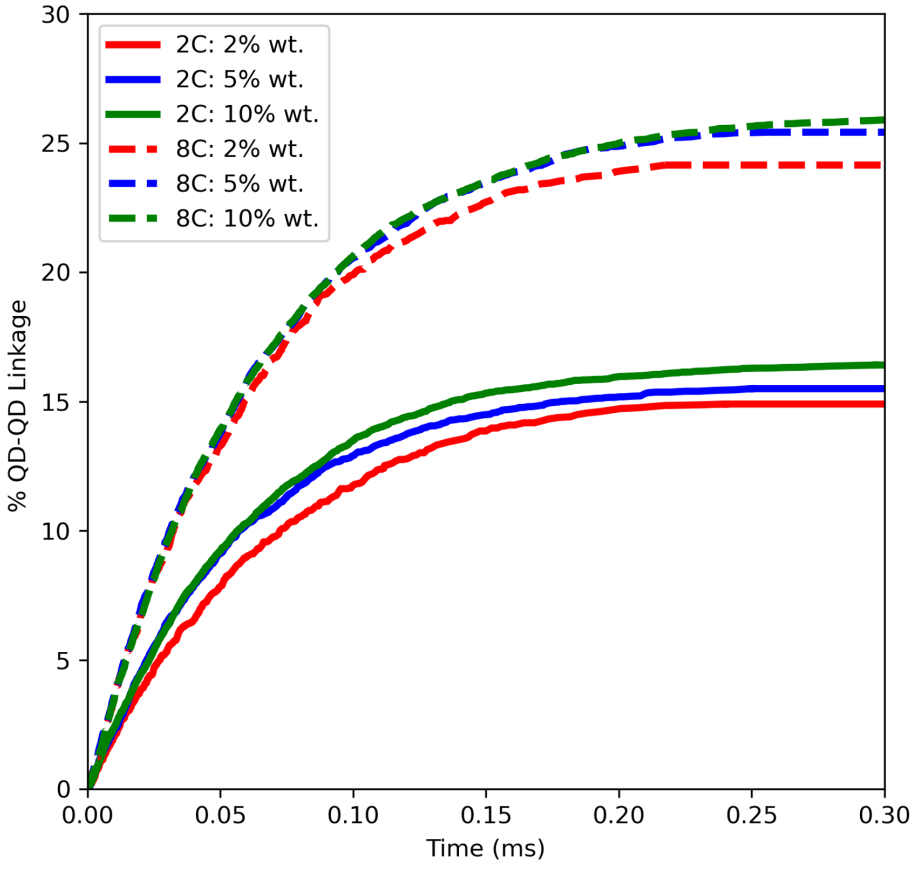


Figure 5.4: Comparison of temporal evolution of percentage QD-QD crosslinking ($\eta_{QD-QD}$) for the case of 2C-LIXER and 8C-LIXER for $W_i$ ($i$ = 2, 5, 10).

### 5.3.2 Effect of Weight Percent of LIXERs ($W_i$)

Further, it is important to see the effect of $W_i$ on $\eta_{QD-QD}$ for the two LIXER cases. Figure 5.4 also shows the compilation of $\eta_{QD-QD}$ evolution for varying $W_i$ for both the cases (i.e., 8C-LIXER and 2C-LIXER). It is evident that $W_i$ does not significantly affect the evolution of $\eta_{QD-QD}$ for either of the LIXER cases, and this behavior can be explained in the following manner. The ordinate in Figure 5.4 shows $\eta_{QD-QD}$, which represents the ratio between the number of QD-QD crosslinking LIXERs, and the total number of crosslinking LIXERs. Intuitively, the number of QD-QD crosslinking LIXERs will increase with $W_i$. However, along with the QD-QD crosslinks, the total number of LIXERs crosslinking the various ligands will also proportionally increase, thereby keeping the ratio of these two terms (i.e., $\eta_{QD-QD}$) at a constant value.

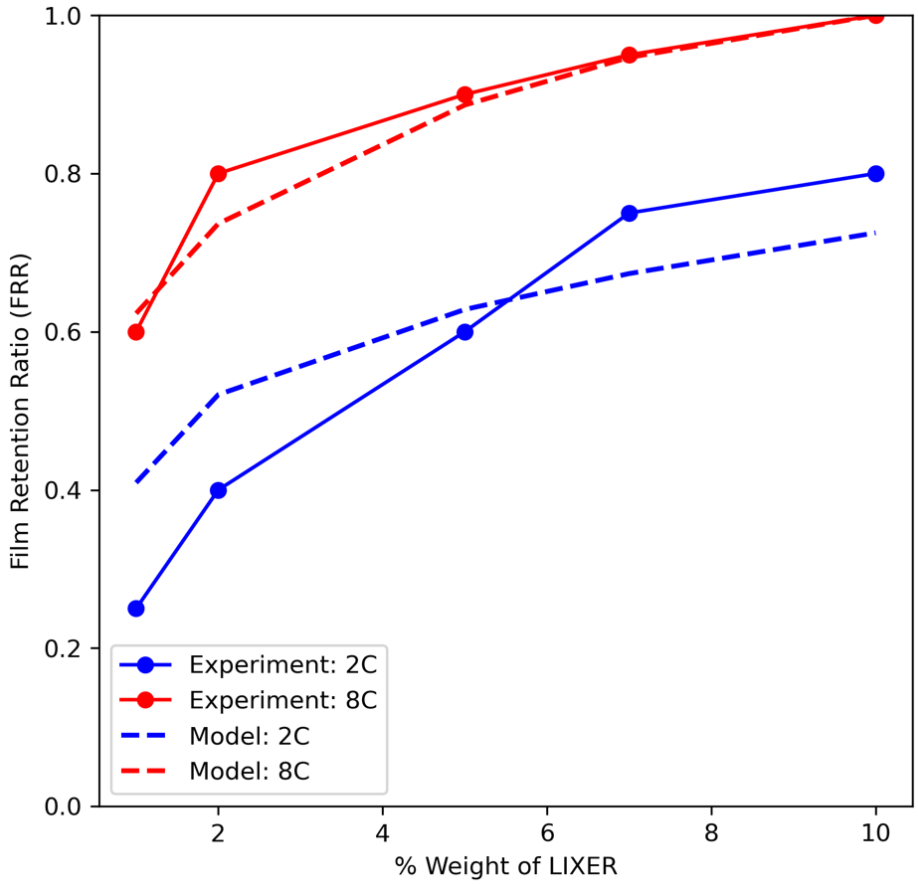


Figure 5.5: Evolution of experimentally measured FRR, and FRR predicted from Equation 5.5.

### 5.3.3 Experimental Validation

To provide further insight into the role of different LIXER kinetics and structures on the chemical robustness of the QD film, it is important to correlate the experimentally measured FRR with number of QD-QD crosslinks ($N_{QD-QD}$) obtained from kMC simulations. Specifically, a crosslinking correlation developed for polymer crosslinking can be modified for the case of ligand crosslinking in QDs in the following manner [185, 186]:

$$FRR = log(N_{QD-QD})M_{LIXER}^{1.5} \tag{5.5}$$

where, $log(N_{QD-QD})$ is a correlation function of number of QD-QD crosslinks which are determined from the kMC simulation, $M_{LIXER}$ is the molecular weight of the LIXER ($g/mol$) and is an indirect measure of the length and bulkiness of the LIXER molecule [187]. Furthermore, Figure 5.5 shows the evolution of experimentally measured FRR, and FRR predicted from Equation 5.5. It is evident from Figure 5.5 that the FRR predictions for 8C-2LIXERs are in excellent agreement with the measured FRR values, whereas the predictions for 2C-LIXER have slight deviations from the measured FRR values. Overall, Equation 5.5 provides a quantitative relationship between experimentally measured FRR and number of QD-QD crosslinks obtained from the kMC simulations.

### 5.3.4 Extension to Multiarmed LIXERs

The above two cases utilize a linear two-armed LIXER that requires higher LIXER loading for better film resistance. However, engineering a 4-armed or 6-armed LIXER can potentially provide a high level of %QD-QD linkage for a low LIXER loading [188]. Moreover, the large molecular size of 4-LIXER and 6-LIXER results in steric hindrance that promotes the LIXER to stay on the surface of the QDs and not penetrate the ligand shell of the QDs. This leads to a higher probability of crosslinking neighboring QDs in addition to increased crosslinking due to the presence of multiple crosslinking arms. Figure 5.6 shows the simulated crosslinking performance (i.e., %QD-QD linkage) in the presence of multiarmed LIXERs along with the previously mentioned linear

LIXER.

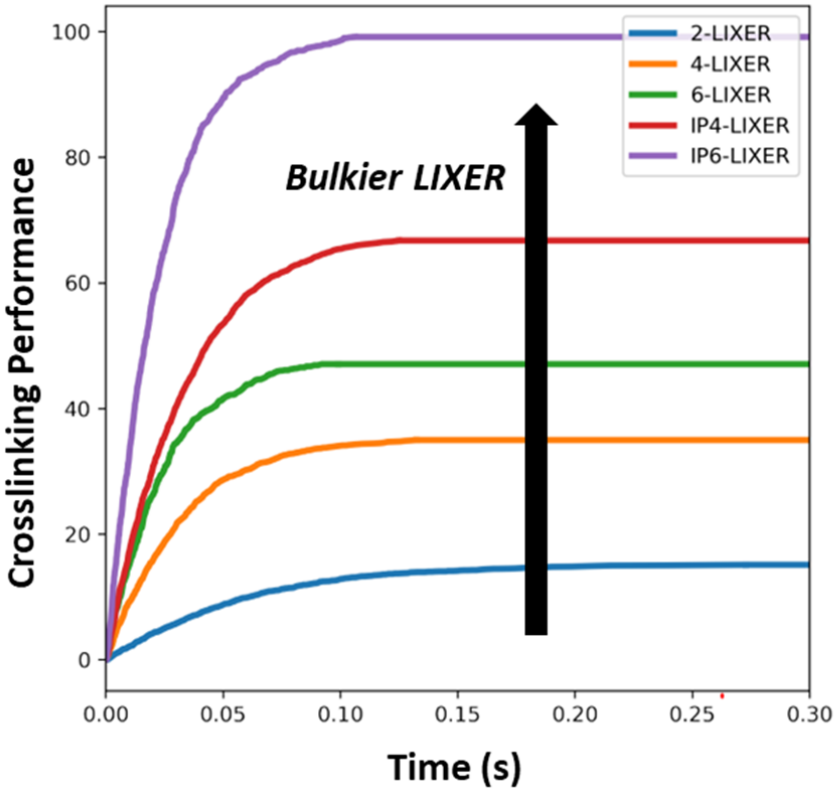


Figure 5.6: Crosslinking performance (i.e., QD-QD linkage) for bulkier multiarmed LIXERs.

## 5.4 Conclusions

Despite the practical importance of forming chemically robust QD films using ligand crosslinkers, the effects of different crosslinkers and their loading in the QD film on the crosslinking performance have not been thoroughly investigated. Here, a kMC model was developed to trace the spatiotemporal evolution of the crosslinking reaction for different crosslinker systems. Specifically, the developed model considers (a) a two-step crosslinking process; (b) considers different spatial crosslinking configurations for the crosslinkers; and (c) computes the crosslinking performance for various different cases. Then, kMC simulations can be performed for different crosslinkers with varying structures within a range of crosslinker loading. Furthermore, CdSe QDs with

light-induced crosslinkers (i.e., LIXERs) were taken as a case study to demonstrate the model predictions. In this particular case, the simulation results suggest that the long length of the 8C-LIXER improves the crosslinking performance as compared to the 2C-LIXER, which is consistent with the experimental observations. Moreover, further analysis shows that engineering multiarmed LIXERs can provide higher crosslinking performance by virtue of a higher steric hindrance and the presence of multiple engaging crosslinking arms. Overall, the developed kMC model provides a mechanistic understanding of the crosslinking process and presents an insight into the engineering of future crosslinkers for better crosslinking performance.

# 6. FUTURE DIRECTIONS

The doctoral thesis work is focused on developing multiscale modeling and control framework for continuous QD production and QD thin-film deposition for various optoelectronic applications. Using the above-developed models as a launchpad, high-impact future works can be formulated to create more generalizable and easily scalable QD models. Specifically, the modeling philosophy followed in the current work has two parts: (a) developing first-principled high-fidelity QD models, and then (b) constructing ML-based black-box models that are computationally efficient. Although this strategy can be implemented for accurate modeling and control of QD manufacturing, it can be improved by following the paradigm of hybrid modeling. Specifically, a more intimate coupling between system-agnostic physics (e.g., mass and energy balance equations, population balance, and transport phenomena, etc.) with system-specific information (i.e., kinetic parameters, growth and nucleation rate, etc.) will result in a hybrid model that is both accurate and computationally efficient. To this end, the following section provides brief details on developing a powerful hybrid model for QD processes and considers a specific example of crystallization.

## 6.1 Transformer-enhanced Hybrid Modeling of QD Systems

Recent years have seen a tremendous push toward the development of digital twins for different chemical systems that facilitate better online process monitoring, control, and on-the-go process optimization. The majority of the digital twins are based on a fully data-driven approach like DNNs along with a few examples of RNN to account for the time-series dynamics of chemical systems. However, given the hesitance of directly deploying a black-box tool in practice due to safety and operational issues, these models have not seen the light of day. To tackle this conundrum, hybrid models that combine first-principles physics-based dynamics with some data-driven components have increased in popularity as they are considered to be a 'best of both worlds' approach. Basically, the first-principle module comprises typical mass and energy balance equations, rate kinetics, and population balance model (PBM) while the data-driven part estimates the system-

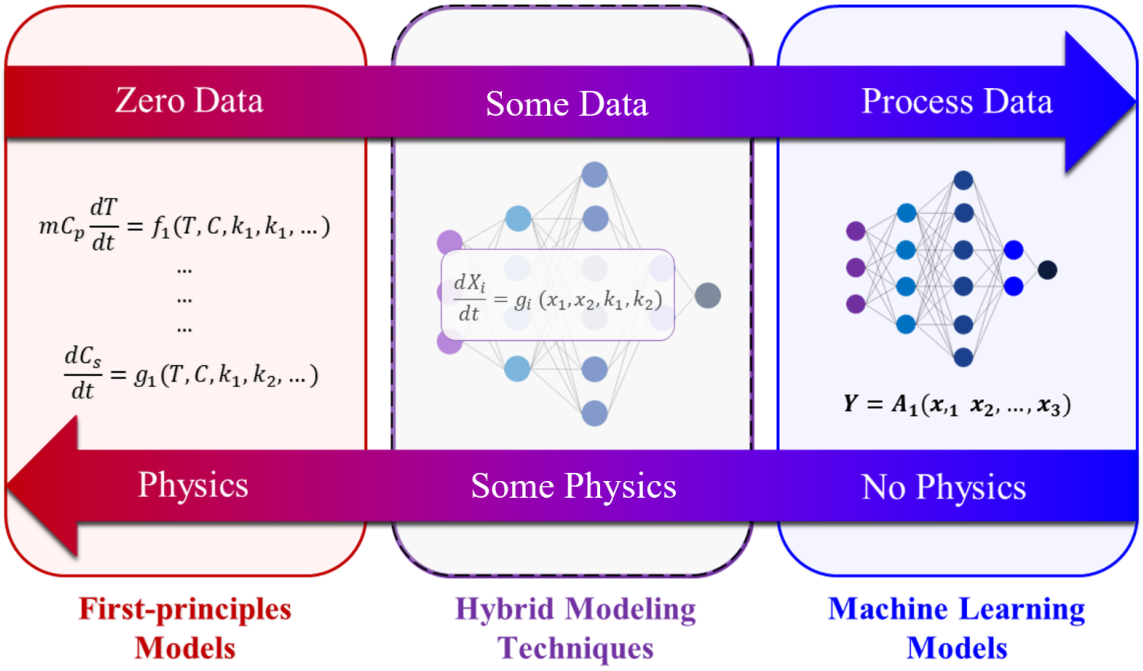


Figure 6.1: Schematic illustration of different modeling paradigms in process systems engineering (PSE).

specific parameters (i.e., kinetic rate constant, growth and nucleation rate, and other parameters), thereby acting as an input to the first-principle module.

Unfortunately, existing hybrid models (that are majorly based on DNNs) require *a priori* information of the kinetic equations which then can be fed with the estimated parameters. This provides a major implementation hurdle as knowing the exact kinetic information of complex systems (i.e., crystallization, fermentation, heterogeneous catalysis) is difficult. For example, in crystallization, knowledge of growth rate (G) and nucleation rate (B) and their dependence on supersaturation, temperature, crystal moments, etc. is difficult to procure. Further, DNN-based hybrid models find it difficult to make accurate time-series predictions in the presence of process uncertainties and noise. Thus, to resolve these two challenges, an alternative paradigm of hybrid modeling that can (a) utilize process data to approximate the underlying kinetic function, and (b) accurately capture the short and long-term evolution of system states is required.

### 6.1.1 Emergence of Transformer Models

On the lines of transfer learning, very recently, transformer-based large language models (LLMs) and vision transformers have pioneered the advent of disruptive applications including ChatGPT, CodeGPT, Dall-E, and others. These applications act as unified models within the natural language processing (NLP) and computer vision space [189, 190, 191, 192, 193, 194, 195, 196]. The key driving force for this revolution has been the advent of transformer networks that utilize (a) a multiheaded self-attention (MAH) mechanism to gain human-like contextual understanding between the words in a given input sentence, (b) positional encoding to embed sequential information efficiently, (c) impressive transfer learning capabilities for rapid fine-tuning for niche tasks, and (d) highly parallelization-friendly architecture (unlike sequential models like RNN) that empowers training of extraordinarily large models (i.e., 100M+ to 10B+ parameters), with of 10TB+ of textual/image data by enabling maximum use of graphics processing units (GPUs). Transformers utilize attention modules that are trained on large amounts of textual data from multiple sources to learn the underlying grammar, syntax, vocabulary, and nuances of a language. This allows the trained transformer model to be directly used for tasks like sentiment analysis and fraudulent email detection or fine-tuned for specific tasks like filtering movie reviews. Unfortunately, utilizing pretrained language models (LLMs) for chemical systems, which involve multivariate time-series data with *floats* and *integers*, is a challenging task with only a few studies in the field. Schweidtmann and colleagues recently converted process flow sheets into input tokens compatible with NLP models, allowing auto-completion of chemical process flow sheets [197]. Meanwhile, *AlphaFold* is a transformer model that predicts protein structure based solely on its amino acid sequence, providing a groundbreaking solution to the longstanding problem of protein folding [198, 199, 200]. Similarly, Venkatasubramanian and Mann demonstrate excellent improvement on existing protein modeling transformers [201]. Lastly, a recent study showcased first-of-a-kind transformer-based MPC implementation for regulation crystal size in an industrial-scale batch crystallizer [202].

Moreover, transformers show a remarkable ability to establish strong correlations between input and outputs, even in the presence of system noise or uncertainties. These models adeptly focus

on short-term and long-term dependencies in the evolution of system states [203, 204]. In essence, the attention mechanism performs a scaled-dot product calculation between various input vectors, enabling it to selectively pay attention to significant long-term (e.g., concentration evolution) and short-term (e.g., sudden change in temperature due to control actions) process alterations by assigning higher attention scores to such instances. As a result, the attention mechanism serves as a filtering mechanism to dynamically handle process uncertainties and data noise by effectively dampening weak correlations and amplifying strong interactions between the system states. Given these unique features, transformers can be highly suitable for time-series predictions and control tasks in crystallization. This is especially true given the complex dependencies that exist between system states, which are highly sensitive to short-term control actions. Despite these exciting possibilities, the practical implementation of various transformer architectures for the modeling and control of various chemical processes, especially for hybrid modeling, has yet to be conclusively demonstrated.

### 6.1.2 Developing TST-based Hybrid Models

Motivated by these exciting opportunities, a hybrid time-series transformer (TST) model for a chemical system with a specific focus on crystallization can be developed [202, 205]. Specifically, the first-principle module will include system agnostic dynamics (i.e., mass-energy balance and population balance equations) while the transformer model approximates a system-specific functional form of growth and nucleation dynamics to allow for a dynamic coupling with the first-principle module. Further, since the existing *vanilla*-transformer architecture utilizes a DNN for approximating the nonlinearities between inputs and outputs, it is not well suited for providing multivariate time-series predictions. Thus, long-short-term-memory networks (LSTM) are integrated with the TST architecture to create a novel TST-LSTM framework that combines the remarkable ability of transformers to learn underlying system dynamics and functionality with the superior performance of LSTM on time-series predictions. As a result, the hybrid-TST-LSTM model is comprised of a first-principles module comprised of generalized mass, energy, and PBM, and a TST-LSTM model that utilizes state information (i.e., concentration, temperature, crystal

moments, etc.) to estimate the functional form of $G$ and $B$. The developed hybrid model can be trained and tested for simulating various QD crystallization systems developed in the previous sections and can be even integrated with an MPC. Overall, the unique ability of transformers to learn complex system dynamics and functions, coupled with superior temporal predictions offered by LSTM, and first-principle modeling offers exciting opportunities for the development of accurate hybrid model-based digital twins for various chemical systems. Moreover, the developed framework can be extended to other chemical systems such as fermentation, reaction engineering, and catalysis. In light of these promising avenues, the future is indeed bright, and we look forward to seeing transformer-based hybrid models make a profound impact in the chemical industry.

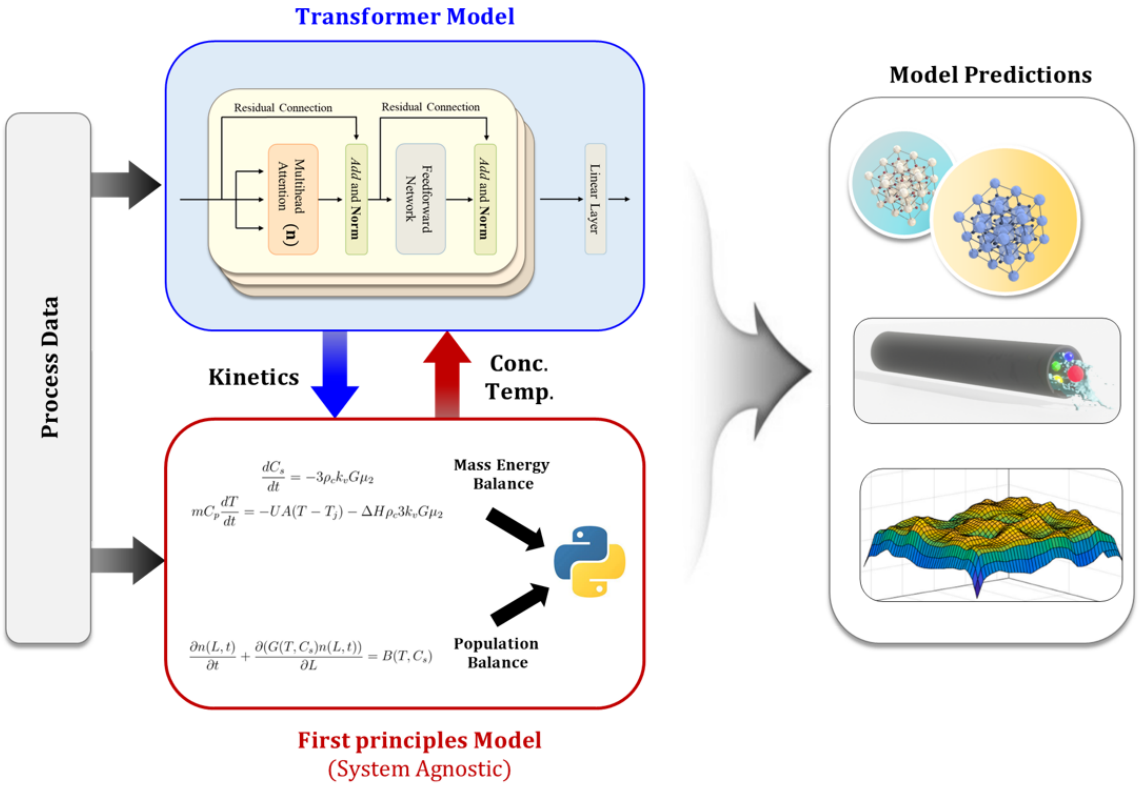


Figure 6.2: Schematic illustration of a transformer-based hybrid model for QD systems.

# 7. SUMMARY

Although there has been a huge impetus for research and commercialization of high-performance QDs for various optoelectronic applications (i.e., solar cells and display technology), there are certain challenges that have not been adequately addressed in the literature. For example, (a) there is a lack of understanding of the crystallization kinetics of various QD systems, which hinders the predictive control of the QD size; (b) very few demonstrations of fast-scalable manufacturing of QDs as well as QD-based optoelectronics; and (c) absence of computationally efficient solutions for online control and optimization of QD processes (i.e., QD crystallization and thin-film deposition). To address these challenges (Figure 7.1), we have developed a continuous QD manufacturing framework using multiscale modeling and advanced process control techniques. First, a multiscale PFC model and CFD-based multiscale SFC were developed to demonstrate set-point tracking of desired QD size and a narrow CSD. This was done by combining a microscopic kMC model, which incorporates the surface-level phenomenon of unit cell adsorption, ligand attachment, and detachment to describe QD crystallization, with macroscopic mass and energy balance equations. The resulting high-fidelity multiscale model was then surrogated using a DNN to obtain computationally efficient optimal operation of PFC and SFC for regulation QD size (i.e., a key product specification for LEDs and solar cells). Second, spray coating-based QD thin-film deposition was modeled using a multiscale model which combines surface-level DEM with macroscopic droplet evaporation. Further, a DNN-based surrogate model was incorporated within the MPC and utilized in conjunction with the multiscale model to regulate thin-film thickness and roughness. Third, although QD crystals of desired size, and smooth thin-films of desired size can be simulated and experimentally synthesized using the above methods, they are not chemically robust leading to postprocessing problems for QD-based devices. Thus, a configurational kMC (ckMC) model for ligand crosslinking was developed to provide insight into QD-QD crosslinking for the development of robust QD nano-patterning techniques. Using the ckMC model, different multiarmed crosslinking agents were engineered to boost QD the thin-film resistance. Overall, the

presented work tackles various modeling challenges in QD manufacturing using a combination of multiscale models (i.e., coupled microscopic and macroscopic models), machine learning, and process control techniques. Moreover, as a natural extension of the developed framework (Figure 7.1), a time-series transformer-based hybrid modeling paradigm is suggested as a promising future direction.

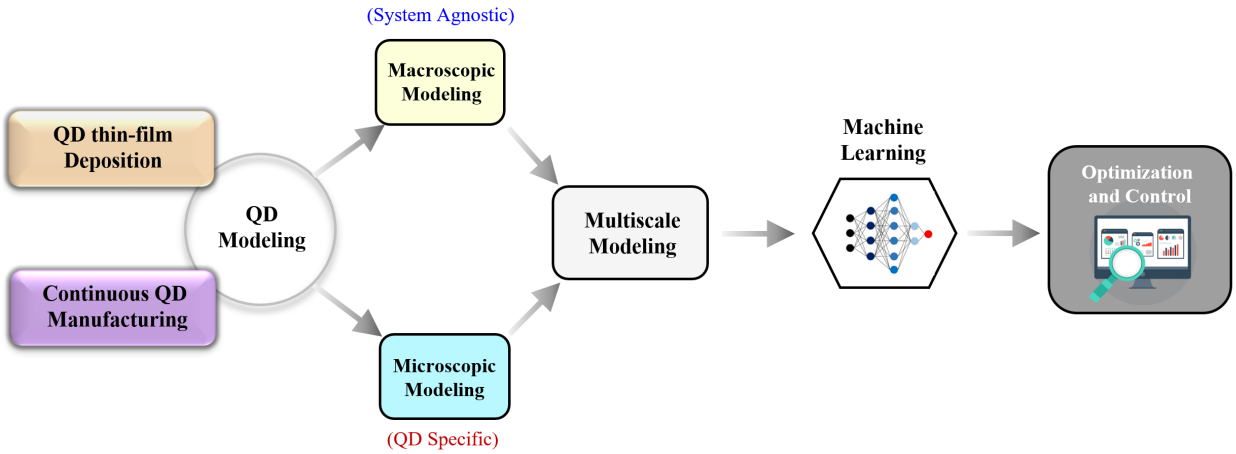


Figure 7.1: Schematic illustration of the QD modeling framework utilized in the current work.

# REFERENCES


[1] R. W. Epps, K. C. Felton, C. W. Coley, and M. Abolhasani, "Automated microfluidic platform for systematic studies of colloidal perovskite nanocrystals: towards continuous nano-manufacturing," *Lab on a Chip*, vol. 17, no. 23, pp. 4040–4047, 2017.

[2] C. B. Kerr, R. W. Epps, and M. Abolhasani, "A low-cost, non-invasive phase velocity and length meter and controller for multiphase lab-in-a-tube devices," *Lab on a Chip*, vol. 19, no. 12, pp. 2107–2113, 2019.

[3] J. Yang, D. Hahm, K. Kim, S. Rhee, M. Lee, S. Kim, Chang, and M. S. Kang, "High-resolution patterning of colloidal quantum dots via non-destructive, light-driven ligand crosslinking," *Nature Communications*, vol. 11, no. 1, pp. 1–9, 2020.

[4] M. L. Petrus, J. Schlipf, C. Li, T. P. Gujar, N. Giesbrecht, P. Müller-Buschbaum, M. Thelakkat, T. Bein, S. Hüttner, and P. Docampo, "Capturing the sun: A review of the challenges and perspectives of perovskite solar cells," *Advanced Energy Materials*, vol. 7, no. 16, p. 1700264, 2017.

[5] D. Li, D. Zhang, K.-S. Lim, Y. Hu, Y. Rong, A. Mei, N.-G. Park, and H. Han, "A review on scaling up perovskite solar cells," *Advanced Functional Materials*, vol. 31, no. 12, p. 2008621, 2021.

[6] G. H. Carey, A. L. Abdelhady, Z. Ning, S. M. Thon, O. M. Bakr, and E. H. Sargent, "Colloidal quantum dot solar cells," *Chemical Reviews*, vol. 115, no. 23, pp. 12732–12763, 2015.

[7] M. I. H. Ansari, A. Qurashi, and M. K. Nazeeruddin, "Frontiers, opportunities, and challenges in perovskite solar cells: A critical review," *Journal of Photochemistry and Photobiology C: Photochemistry Reviews*, vol. 35, pp. 1–24, 2018.

[8] N.-G. Park and K. Zhu, "Scalable fabrication and coating methods for perovskite solar cells and solar modules," *Nature Reviews Materials*, vol. 5, no. 5, pp. 333–350, 2020.

[9] R. Zhu, Z. Luo, H. Chen, Y. Dong, and S.-T. Wu, "Realizing rec. 2020 color gamut with quantum dot displays," *Optics Express*, vol. 23, no. 18, pp. 23680–23693, 2015.

[10] X. Zhang, H.-C. Wang, A.-C. Tang, S.-Y. Lin, H.-C. Tong, C.-Y. Chen, Y.-C. Lee, T.-L. Tsai, and R.-S. Liu, "Robust and stable narrow-band green emitter: an option for advanced wide-color-gamut backlight display," *Chemistry of Materials*, vol. 28, no. 23, pp. 8493–8497, 2016.

[11] M. K. Choi, J. Yang, T. Hyeon, and D.-H. Kim, "Flexible quantum dot light-emitting diodes for next-generation displays," *NPJ Flexible Electronics*, vol. 2, no. 1, pp. 1–14, 2018.

[12] Z. Liu, C.-H. Lin, B.-R. Hyun, C.-W. Sher, Z. Lv, B. Luo, F. Jiang, T. Wu, C.-H. Ho, and H.-C. Kuo, "Micro-light-emitting diodes with quantum dots in display technology," *Light: Science & Applications*, vol. 9, no. 1, pp. 1–23, 2020.

[13] L. Protesescu, S. Yakunin, M. I. Bodnarchuk, F. Krieg, R. Caputo, C. H. Hendon, R. X. Yang, A. Walsh, and M. V. Kovalenko, "Nanocrystals of cesium lead halide perovskites ($CsPbX_3$, X= Cl, Br, and I): novel optoelectronic materials showing bright emission with wide color gamut," *Nano Letters*, vol. 15, no. 6, pp. 3692–3696, 2015.

[14] I. J. Kramer, J. C. Minor, G. Moreno-Bautista, L. Rollny, P. Kanjanaboos, D. Kopilovic, S. M. Thon, G. H. Carey, K. W. Chou, and D. Zhitomirsky, "Efficient spray-coated colloidal quantum dot solar cells," *Advanced Materials*, vol. 27, no. 1, pp. 116–121, 2015.

[15] C. Jiang, Z. Zhong, B. Liu, Z. He, J. Zou, L. Wang, J. Wang, J. Peng, and Y. Cao, "Coffee-ring-free quantum dot thin film using inkjet printing from a mixed-solvent system on modified zno transport layer for light-emitting devices," *ACS Applied Materials & Interfaces*, vol. 8, no. 39, pp. 26162–26168, 2016.

[16] Z. Yang, M. Wang, J. Li, J. Dou, H. Qiu, and J. Shao, "Spray-coated $CsPbBr_3$ quantum dot films for perovskite photodiodes," *ACS Applied Materials & Interfaces*, vol. 10, no. 31, pp. 26387–26395, 2018.

[17] C. R. Kagan, E. Lifshitz, E. H. Sargent, and D. V. Talapin, "Building devices from colloidal quantum dots," *Science*, vol. 353, no. 6302, p. aac5523, 2016.

[18] P. Ramasamy, D.-H. Lim, B. Kim, S.-H. Lee, M.-S. Lee, and J.-S. Lee, "All-inorganic cesium lead halide perovskite nanocrystals for photodetector applications," *Chemical Communications*, vol. 52, no. 10, pp. 2067–2070, 2016.

[19] Y. Wei, Z. Cheng, and J. Lin, "An overview on enhancing the stability of lead halide perovskite quantum dots and their applications in phosphor-converted leds," *Chemical Society Reviews*, vol. 48, no. 1, pp. 310–350, 2019.

[20] M. Liu, N. Yazdani, M. Yarema, M. Jansen, V. Wood, and E. H. Sargent, "Colloidal quantum dot electronics," *Nature Electronics*, vol. 4, no. 8, pp. 548–558, 2021.

[21] M. B. Faheem, B. Khan, C. Feng, M. U. Farooq, F. Raziq, Y. Xiao, and Y. Li, "All-inorganic perovskite solar cells: energetics, key challenges, and strategies toward commercialization," *ACS Energy Letters*, vol. 5, no. 1, pp. 290–320, 2019.

[22] F. P. García de Arquer, D. V. Talapin, V. I. Klimov, Y. Arakawa, M. Bayer, and E. H. Sargent, "Semiconductor quantum dots: Technological progress and future challenges," *Science*, vol. 373, no. 6555, p. eaaz8541, 2021.

[23] M. Danek, K. F. Jensen, C. B. Murray, and M. G. Bawendi, "Synthesis of luminescent thin-film CdSe/ZnSe quantum dot composites using CdSe quantum dots passivated with an overlayer of ZnSe," *Chemistry of Materials*, vol. 8, no. 1, pp. 173–180, 1996.

[24] M. V. Kovalenko, "Opportunities and challenges for quantum dot photovoltaics," *Nature Nanotechnology*, vol. 10, no. 12, pp. 994–997, 2015.

[25] M. R. Kim and D. Ma, "Quantum-dot-based solar cells: recent advances, strategies, and challenges," *The Journal of Physical Chemistry Letters*, vol. 6, no. 1, pp. 85–99, 2015.

[26] Y. Lou, M. Fang, J. Chen, and Y. Zhao, "Formation of highly luminescent cesium bismuth halide perovskite quantum dots tuned by anion exchange," *Chemical Communications*, vol. 54, no. 30, pp. 3779–3782, 2018.

[27] K. Abdel-Latif, R. W. Epps, C. B. Kerr, C. M. Papa, F. N. Castellano, and M. Abolhasani, "Facile room-temperature anion exchange reactions of inorganic perovskite quantum dots enabled by a modular microfluidic platform," *Advanced Functional Materials*, vol. 29, no. 23, p. 1900712, 2019.

[28] T. Chiba, Y. Hayashi, H. Ebe, K. Hoshi, J. Sato, S. Sato, Y.-J. Pu, S. Ohisa, and J. Kido, "Anion-exchange red perovskite quantum dots with ammonium iodine salts for highly efficient light-emitting devices," *Nature Photonics*, vol. 12, no. 11, pp. 681–687, 2018.

[29] A. Pan, B. He, X. Fan, Z. Liu, J. J. Urban, A. P. Alivisatos, L. He, and Y. Liu, "Insight into the ligand-mediated synthesis of colloidal $CsPbBr_3$ perovskite nanocrystals: the role of organic acid, base, and cesium precursors," *ACS Nano*, vol. 10, no. 8, pp. 7943–7954, 2016.

[30] S. Sun, D. Yuan, Y. Xu, A. Wang, and Z. Deng, "Ligand-mediated synthesis of shape-controlled cesium lead halide perovskite nanocrystals via reprecipitation process at room temperature," *ACS Nano*, vol. 10, no. 3, pp. 3648–3657, 2016.

[31] B. Luo, Y.-C. Pu, S. A. Lindley, Y. Yang, L. Lu, Y. Li, X. Li, and J. Z. Zhang, "Organolead halide perovskite nanocrystals: branched capping ligands control crystal size and stability," *Angewandte Chemie International Edition*, vol. 55, no. 31, pp. 8864–8868, 2016.

[32] J. De Roo, M. Ibáñez, P. Geiregat, G. Nedelcu, W. Walravens, J. Maes, J. C. Martins, I. Van Driessche, M. V. Kovalenko, and Z. Hens, "Highly dynamic ligand binding and light absorption coefficient of cesium lead bromide perovskite nanocrystals," *ACS Nano*, vol. 10, no. 2, pp. 2071–2081, 2016.

[33] D. Parobek, Yitong, T. Qiao, and D. H. Son, "Direct Hot-Injection Synthesis of Mn-Doped $CsPbBr_3$ Nanocrystals," *Chemistry of Materials*, vol. 30, pp. 2939–2944, May 2018.

[34] E. Yassitepe, Z. Yang, O. Voznyy, Y. Kim, G. Walters, J. A. Castañeda, P. Kanjanaboos, M. Yuan, X. Gong, F. Fan, J. Pan, S. Hoogland, R. Comin, O. M. Bakr, L. A. Padilha, A. F. Nogueira, and E. H. Sargent, "Amine-Free Synthesis of Cesium Lead Halide Per-

ovskite Quantum Dots for Efficient Light-Emitting Diodes," *Advanced Functional Materials*, vol. 26, pp. 8757–8763, December 2016.

[35] J. Y. Woo, Y. Kim, J. Bae, T. G. Kim, J. W. Kim, D. C. Lee, and S. Jeong, "Highly Stable Cesium Lead Halide Perovskite Nanocrystals through in Situ Lead Halide Inorganic Passivation," *Chemistry of Materials*, vol. 29, pp. 7088–7092, September 2017.

[36] Y. Dong, T. Qiao, D. Kim, D. Parobek, D. Rossi, and D. H. Son, "Precise control of quantum confinement in cesium lead halide perovskite quantum dots via thermodynamic equilibrium," *Nano Letters*, vol. 18, no. 6, pp. 3716–3722, 2018.

[37] J. S. Kwon, M. Nayhouse, P. D. Christofides, and G. Orkoulas, "Modeling and control of protein crystal shape and size in batch crystallization," *AIChE Journal*, vol. 59, no. 7, pp. 2317–2327, 2013.

[38] S. D. Durbin and G. Feher, "Crystal growth studies of lysozyme as a model for protein crystallization," *Journal of Crystal Growth*, vol. 76, no. 3, pp. 583–592, 1986.

[39] S. D. Durbin and G. Feher, "Simulation of lysozyme crystal growth by the Monte Carlo method," *Journal of Crystal Growth*, vol. 110, pp. 41–51, March 1991.

[40] A. Markande, A. Nezzal, J. Fitzpatrick, L. Aerts, and A. Redl, "Influence of impurities on the crystallization of dextrose monohydrate," *Journal of Crystal Growth*, vol. 353, no. 1, pp. 145–151, 2012.

[41] R. W. Epps, M. S. Bowen, A. A. Volk, K. Abdel-Latif, S. Han, K. G. Reyes, A. Amassian, and M. Abolhasani, "Artificial chemist: an autonomous quantum dot synthesis bot," *Advanced Materials*, vol. 32, no. 30, p. 2001626, 2020.

[42] R. W. Epps and M. Abolhasani, "Modern nanoscience: Convergence of AI, robotics, and colloidal synthesis," *Applied Physics Reviews*, vol. 8, no. 4, p. 041316, 2021.

[43] R. W. Epps, K. C. Felton, C. W. Coley, and M. Abolhasani, "A modular microfluidic technology for systematic studies of colloidal semiconductor nanocrystals," *JoVE (Journal of Visualized Experiments)*, no. 135, p. e57666, 2018.

[44] J. Zheng, M. Zhang, C. F. J. Lau, X. Deng, J. Kim, Q. Ma, C. Chen, M. A. Green, S. Huang, and A. W. Ho-Baillie, "Spin-coating free fabrication for highly efficient perovskite solar cells," *Solar Energy Materials and Solar Cells*, vol. 168, pp. 165–171, 2017.

[45] X. Pi, Q. Li, D. Li, and D. Yang, "Spin-coating silicon-quantum-dot ink to improve solar cell efficiency," *Solar Energy Materials and Solar Cells*, vol. 95, no. 10, pp. 2941–2945, 2011.

[46] Y.-J. Lee, C.-J. Lee, and C.-M. Cheng, "Enhancing the conversion efficiency of red emission by spin-coating CdSe quantum dots on the green nanorod light-emitting diode," *Optics Express*, vol. 18, no. 104, pp. A554–A561, 2010.

[47] M. Chen, H. Yu, S. V. Kershaw, H. Xu, S. Gupta, F. Hetsch, A. L. Rogach, and N. Zhao, "Fast, air-stable infrared photodetectors based on spray-deposited aqueous hgte quantum dots," *Advanced Functional Materials*, vol. 24, no. 1, pp. 53–59, 2014.

[48] J. E. Bishop, J. A. Smith, and D. G. Lidzey, "Development of spray-coated perovskite solar cells," *ACS Applied Materials & Interfaces*, vol. 12, no. 43, pp. 48237–48245, 2020.

[49] M. Li, W. Zhang, G. Shao, H. Kan, Z. Song, S. Xu, H. Yu, S. Jiang, J. Luo, and H. Liu, "Sensitive $NO_2$ gas sensors employing spray-coated colloidal quantum dots," *Thin Solid Films*, vol. 618, pp. 271–276, 2016.

[50] H. Chen, X. Ding, X. Pan, T. Hayat, A. Alsaedi, Y. Ding, and S. Dai, "Reducing the universal "coffee-ring effect" by a vapor-assisted spraying method for high-efficiency $CH_3NH_3PbI_3$ perovskite solar cells," *ACS Applied Materials & Interfaces*, vol. 10, no. 28, pp. 23466–23475, 2018.

[51] Z. Zhang, X. Zhang, Z. Xin, M. Deng, Y. Wen, and Y. Song, "Controlled inkjetting of a conductive pattern of silver nanoparticles based on the coffee-ring effect," *Advanced Materials*, vol. 25, no. 46, pp. 6714–6718, 2013.

[52] M. Schramböck, A. M. Andrews, T. Roch, W. Schrenk, A. Lugstein, and G. Strasser, "Controlled inkjetting of a conductive pattern of silver nanoparticles based on the coffee-ring effect," *Microelectronics Journal*, vol. 37, no. 12, pp. 1532–1534, 2006.

[53] W. Xie, R. Gomes, T. Aubert, S. Bisschop, Y. Zhu, Z. Hens, E. Brainis, and D. Van Thourhout, "Nanoscale and single-dot patterning of colloidal quantum dots," *Nano Letters*, vol. 15, no. 11, pp. 7481–7487, 2015.

[54] G. Liu, H. Zhao, F. Diao, Z. Ling, and Y. Wang, "Stable tandem luminescent solar concentrators based on CdSe/CdS quantum dots and carbon dots," *Journal of Materials Chemistry C*, vol. 6, no. 37, pp. 10059–10066, 2018.

[55] J. Lim, W. K. Bae, J. Kwak, S. Lee, C. Lee, and K. Char, "Perspective on synthesis, device structures, and printing processes for quantum dot displays," *Optical Materials Express*, vol. 2, no. 5, pp. 594–628, 2012.

[56] N. YoungáCho and J. WooáChoi, "Simple one-pot synthesis and high-resolution patterning of perovskite quantum dots using a photocurable ligand," *Chemical Communications*, vol. 57, no. 95, pp. 12824–12827, 2021.

[57] M. Nayhouse, J. S. Kwon, P. D. Christofides, and G. Orkoulas, "Crystal shape modeling and control in protein crystal growth," *Chemical Engineering Science*, vol. 87, pp. 216–223, 2013.

[58] J. S. Kwon, M. Nayhouse, P. D. Christofides, and G. Orkoulas, "Protein crystal shape and size control in batch crystallization: Comparing model predictive control with conventional operating policies," *Industrial & Engineering Chemistry Research*, vol. 53, no. 13, pp. 5002–5014, 2014.

[59] J. S. Kwon, M. Nayhouse, G. Orkoulas, and P. D. Christofides, "Crystal shape and size control using a plug flow crystallization configuration," *Chemical Engineering Science*, vol. 119, pp. 30–39, 2014.

[60] J. S. Kwon, M. Nayhouse, G. Orkoulas, D. Ni, and P. D. Christofides, "Run-to-run-based model predictive control of protein crystal shape in batch crystallization," *Industrial & Engineering Chemistry Research*, vol. 54, no. 16, pp. 4293–4302, 2015.

[61] J. S. Kwon, M. Nayhouse, P. D. Christofides, and G. Orkoulas, "Modeling and control of shape distribution of protein crystal aggregates," *Chemical Engineering Science*, vol. 104, pp. 484–497, 2013.

[62] J. S. Kwon, M. Nayhouse, G. Orkoulas, and P. D. Christofides, "Enhancing the crystal production rate and reducing polydispersity in continuous protein crystallization," *Industrial & Engineering Chemistry Research*, vol. 53, no. 40, pp. 15538–15548, 2014.

[63] J. S. Kwon, M. Nayhouse, and P. D. Christofides, "Multiscale, multidomain modeling and parallel computation: application to crystal shape evolution in crystallization," *Industrial & Engineering Chemistry Research*, vol. 54, no. 47, pp. 11903–11914, 2015.

[64] M. Crose, J. S. Kwon, M. Nayhouse, D. Ni, and P. D. Christofides, "Multiscale modeling and operation of PECVD of thin film solar cells," *Chemical Engineering Science*, vol. 136, pp. 50–61, 2015.

[65] M. Crose, J. S. Kwon, A. Tran, and P. D. Christofides, "Multiscale modeling and run-to-run control of PECVD of thin film solar cells," *Renewable Energy*, vol. 100, pp. 129–140, 2017.

[66] M. Crose, W. Zhang, A. Tran, and P. D. Christofides, "Multiscale three-dimensional CFD modeling for PECVD of amorphous silicon thin films," *Computers & Chemical Engineering*, vol. 113, pp. 184–195, 2018.

[67] M. Crose, W. Zhang, A. Tran, and P. D. Christofides, "Run-to-run control of PECVD systems: Application to a multiscale three-dimensional CFD model of silicon thin film deposition," *AIChE Journal*, vol. 65, no. 7, p. e16400, 2019.

[68] G. Kimaev and L. A. Ricardez-Sandoval, "Nonlinear model predictive control of a multiscale thin film deposition process using artificial neural networks," *Chemical Engineering Science*, vol. 207, pp. 1230–1245, 2019.

[69] G. Kimaev and L. A. Ricardez-Sandoval, "Artificial neural network discrimination for parameter estimation and optimal product design of thin films manufactured by chemical vapor deposition," *The Journal of Physical Chemistry C*, vol. 124, no. 34, pp. 18615–18627, 2020.

[70] S. Rasoulian and L. A. Ricardez-Sandoval, "Stochastic nonlinear model predictive control applied to a thin film deposition process under uncertainty," *Chemical Engineering Science*, vol. 140, pp. 90–103, 2016.

[71] D. Chaffart and L. A. Ricardez-Sandoval, "Optimization and control of a thin film growth process: A hybrid first principles/artificial neural network based multiscale modelling approach," *Computers & Chemical Engineering*, vol. 119, pp. 465–479, 2018.

[72] H.-K. Choi and J. S. Kwon, "Multiscale modeling and model-based feedback control of pulp digester," in *2019 American Control Conference (ACC)*, pp. 2819–2824, IEEE, 2019.

[73] S. Pahari, J. Kim, H.-K. Choi, M. Zhang, A. Ji, C. G. Yoo, and J. S. Kwon, "Multiscale kinetic modeling of biomass fractionation in an experiment: Understanding individual reaction mechanisms and cellulose degradation," *Chemical Engineering Journal*, vol. 467, p. 143021, 2023.

[74] H.-K. Choi and J. S. Kwon, "Multiscale modeling and multiobjective control of wood fiber morphology in batch pulp digester," *AIChE Journal*, vol. e16972, 2020.

[75] S. H. Son, H.-K. Choi, and J. S. Kwon, "Multiscale modeling and control of pulp digester under fiber-to-fiber heterogeneity," *Computers & Chemical Engineering*, vol. 143, p. 107117, 2020.

[76] H.-K. Choi and J. S. Kwon, "Multiscale modeling and predictive control of cellulose accessibility in alkaline pretreatment for enhanced glucose yield," *Fuel*, vol. 280, p. 118546, 2020.

[77] H.-K. Choi, S. H. Son, and J. Kwon, "Inferential model predictive control of continuous pulping under grade transition," *Industrial & Engineering Chemistry Research*, vol. 60, no. 9, pp. 3699–3710, 2021.

[78] J. Jung, H.-K. Choi, S. H. Son, J. S. Kwon, and J. H. Lee, "Multiscale modeling of fiber deformation: Application to a batch pulp digester for model predictive control of fiber strength," *Computers & Chemical Engineering*, vol. 158, p. 107640, 2022.

[79] S. H. Son, H.-K. Choi, J. Moon, and J. S. Kwon, "Hybrid Koopman model predictive control of nonlinear systems using multiple EDMD models: An application to a batch pulp digester with feed fluctuation," *Control Engineering Practice*, vol. 118, p. 104956, 2022.

[80] P. Shah, H.-K. Choi, and J. S. Kwon, "Achieving optimal paper properties: A layered multiscale kMC and LSTM-ANN-based control approach for kraft pulping," *Processes*, vol. 11, no. 3, p. 809, 2023.

[81] S. H. Son, H.-K. Choi, and J. S. Kwon, "Application of offset-free Koopman-based model predictive control to a batch pulp digester," *AIChE Journal*, vol. 67, no. 9, p. e17301, 2021.

[82] S. Pahari, J. Moon, M. Akbulut, S. Hwang, and J. S. Kwon, "Model predictive control for wormlike micelles (WLMs): Application to a system of CTAB and NaCl," *Chemical Engineering Research and Design*, vol. 174, pp. 30–41, 2021.

[83] S. Pahari, S. Liu, C. H. Lee, M. Akbulut, and J. S. Kwon, "SAXS-guided unbiased coarse-grained Monte Carlo simulation for identification of self-assembly nanostructures and dimensions," *Soft Matter*, vol. 18, no. 28, pp. 5282–5292, 2022.

[84] S. Pahari, B. Bhadriraju, M. Akbulut, and J. S. Kwon, "A slip-spring framework to study relaxation dynamics of entangled wormlike micelles with kinetic Monte Carlo algorithm," *Journal of Colloid and Interface Science*, vol. 600, pp. 550–560, 2021.

[85] D. Chaffart and L. A. Ricardez-Sandoval, "A three dimensional kinetic monte carlo defect-free crystal dissolution model for biological systems, with application to uncertainty analysis and robust optimization," *Computers & Chemical Engineering*, vol. 157, p. 107586, 2022.

[86] D. Lee, A. Singla, H.-J. Wu, and J. S. Kwon, "Dynamic modeling of binding kinetics between GD1b ganglioside and CTB," in *2018 Annual American Control Conference (ACC)*, pp. 1999–2004, IEEE, 2018.

[87] H.-K. Choi, D. Lee, A. Singla, J. S. Kwon, and H.-J. Wu, "The influence of heteromultivalency on lectin–glycan binding behavior," *Glycobiology*, vol. 29, no. 5, pp. 397–408, 2019.

[88] D. Lee, A. Green, H.-J. Wu, and J. S. Kwon, "Hybrid PDE-kMC modeling approach to simulate multivalent lectin-glycan binding process," *AIChE Journal*, vol. 67, no. 12, p. e17453, 2021.

[89] N. C. Worstell, A. Singla, P. Saenkham, T. Galbadage, P. Sule, D. Lee, A. Mohr, J. S. Kwon, J. D. Cirillo, and H.-J. Wu, "Hetero-multivalency of Pseudomonas aeruginosa lectin LecA binding to model membranes," *Scientific Reports*, vol. 8, no. 1, p. 8419, 2018.

[90] D. Lee, A. Mohr, J. S. Kwon, and H.-J. Wu, "Kinetic Monte Carlo modeling of multivalent binding of CTB proteins with gm1 receptors," *Computers & Chemical Engineering*, vol. 118, pp. 283–295, 2018.

[91] D. Lee, A. Jayaraman, and J. S. Kwon, "Identification of cell-to-cell heterogeneity through systems engineering approaches," *AIChE Journal*, vol. 66, no. 5, p. e16925, 2020.

[92] D. Lee, A. Jayaraman, and J. S. Kwon, "Development of a hybrid model for a partially known intracellular signaling pathway through correction term estimation and neural network modeling," *PLoS Computational Biology*, vol. 16, no. 12, p. e1008472, 2020.

[93] C. H. Lee, S. Pahari, N. Sitapure, M. A. Barteau, and J. S. Kwon, "DFT–kMC analysis for identifying novel bimetallic electrocatalysts for enhanced NRR performance by suppressing HER at ambient conditions via active-site separation," *ACS Catalysis*, vol. 12, no. 24, pp. 15609–15617, 2022.

[94] C. H. Lee, S. Pahari, N. Sitapure, M. A. Barteau, and J. S. Kwon, "Investigating high-performance non-precious transition metal oxide catalysts for nitrogen reduction reaction: A multifaceted DFT-kMC-LSTM approach," *ACS Catalysis*, 2023 *(in press)*.

[95] M. Stamatakis, Y. Chen, and D. G. Vlachos, "First-principles-based kinetic Monte Carlo simulation of the structure sensitivity of the water–gas shift reaction on platinum surfaces," *The Journal of Physical Chemistry C*, vol. 115, no. 50, pp. 24750–24762, 2011.

[96] G. Kimaev, D. Chaffart, and L. A. Ricardez-Sandoval, "Multilevel Monte Carlo applied for uncertainty quantification in stochastic multiscale systems," *AIChE Journal*, vol. e16262, 2020.

[97] M. Salciccioli, M. Stamatakis, S. Caratzoulas, and D. G. Vlachos, "A review of multiscale modeling of metal-catalyzed reactions: Mechanism development for complexity and emergent behavior," *Chemical Engineering Science*, vol. 66, no. 19, pp. 4319–4355, 2011.

[98] J. Li, E. Croiset, and L. Ricardez-Sandoval, "Carbon nanotube growth: First-principles-based kinetic monte carlo model," *Journal of Catalysis*, vol. 326, pp. 15–25, 2015.

[99] D. Chaffart and L. A. Ricardez-Sandoval, "Robust optimization of a multiscale heterogeneous catalytic reactor system with spatially-varying uncertainty descriptions using polynomial chaos expansions," *The Canadian Journal of Chemical Engineering*, vol. 96, no. 1, pp. 113–131, 2018.

[100] D. Chaffart and L. A. Ricardez-Sandoval, "Robust dynamic optimization in heterogeneous multiscale catalytic flow reactors using polynomial chaos expansion," *Journal of Process Control*, vol. 60, pp. 128–140, 2017.

[101] J. Li, G. Liu, B. Ren, E. Croiset, Y. Zhang, and L. Ricardez-Sandoval, "Mechanistic study of site blocking catalytic deactivation through accelerated kinetic monte carlo," *Journal of Catalysis*, vol. 378, pp. 176–183, 2019.

[102] D. Chaffart, S. Shi, C. Ma, C. Lv, and L. A. Ricardez-Sandoval, "A moving front kinetic monte carlo algorithm for moving interface systems," *The Journal of Physical Chemistry B*, vol. 126, no. 9, pp. 2040–2059, 2022.

[103] D. Chaffart, S. Shi, C. Ma, C. Lv, and L. A. Ricardez-Sandoval, "A semi-empirical force balance-based model to capture sessile droplet spread on smooth surfaces: A moving front kinetic monte carlo study," *Physics of Fluids*, vol. 35, no. 3, 2023.

[104] N. Sitapure, H. Lee, F. Ospina-Acevedo, P. B. Balbuena, S. Hwang, and J. S. Kwon, "A computational approach to characterize formation of a passivation layer in lithium metal anodes," *AIChE Journal*, p. e17073, 2020.

[105] H. Lee, N. Sitapure, S. Hwang, and J. S. Kwon, "Multiscale modeling of dendrite formation in lithium-ion batteries," *Computers & Chemical Engineering*, vol. 153, p. 107415, 2021.

[106] G. Hwang, N. Sitapure, J. Moon, H. Lee, S. Hwang, and J. S. Kwon, "Model predictive control of lithium-ion batteries: Development of optimal charging profile for reduced intracycle capacity fade using an enhanced single particle model (SPM) with first-principled chemical/mechanical degradation mechanisms," *Chemical Engineering Journal*, vol. 134768, 2022.

[107] A. Narasingam and J. S. Kwon, "Development of local dynamic mode decomposition with control: Application to model predictive control of hydraulic fracturing," *Computers & Chemical Engineering*, vol. 106, pp. 501–511, 2017.

[108] A. Narasingam, P. Siddhamshetty, and J. S. Kwon, "Handling spatial heterogeneity in reservoir parameters using proper orthogonal decomposition based ensemble kalman filter for model-based feedback control of hydraulic fracturing," *Industrial & Engineering Chemistry Research*, vol. 57, no. 11, pp. 3977–3989, 2018.

[109] A. Narasingam, P. Siddhamshetty, and J. S. Kwon, "Temporal clustering for order reduction of nonlinear parabolic PDE systems with time-dependent spatial domains: Application to a hydraulic fracturing process," *AIChE Journal*, vol. 63, no. 9, pp. 3818–3831, 2017.

[110] A. Narasingam and J. S. Kwon, "Data-driven identification of interpretable reduced-order models using sparse regression," *Computers & Chemical Engineering*, vol. 119, pp. 101–111, 2018.

[111] S. L. Brunton, J. L. Proctor, and J. N. Kutz, "Discovering governing equations from data by sparse identification of nonlinear dynamical systems," *Proceedings of the National Academy of Sciences*, vol. 113, no. 15, pp. 3932–3937, 2016.

[112] B. Bhadriraju, A. Narasingam, and J. S. Kwon, "Machine learning-based adaptive model identification of systems: Application to a chemical process," *Chemical Engineering Research and Design*, vol. 152, pp. 372–383, 2019.

[113] B. Bhadriraju, M. S. F. Bangi, A. Narasingam, and J. S. Kwon, "Operable adaptive sparse identification of systems: Application to chemical processes," *AIChE Journal*, vol. 66, no. 11, p. e16980, 2020.

[114] B. Bhadriraju, J. S. Kwon, and F. Khan, "Risk-based fault prediction of chemical processes using operable adaptive sparse identification of systems (OASIS)," *Computers & Chemical Engineering*, vol. 152, p. 107378, 2021.

[115] B. Bhadriraju, J. S. Kwon, and F. Khan, "An adaptive data-driven approach for two-timescale dynamics prediction and remaining useful life estimation of li-ion batteries," *Computers & Chemical Engineering*, p. 108275, 2023.

[116] A. Narasingam and J. S. Kwon, "Koopman Lyapunov-based model predictive control of nonlinear chemical process systems," *AIChE Journal*, vol. 65, no. 11, p. e16743, 2019.

[117] A. Narasingam and J. S. Kwon, "Application of Koopman operator for model-based control of fracture propagation and proppant transport in hydraulic fracturing operation," *Journal of Process Control*, vol. 91, pp. 25–36, 2020.

[118] A. Narasingam and J. S. Kwon, "Closed-loop stabilization of nonlinear systems using Koopman Lyapunov-based model predictive control," in *59th IEEE Conference on Decision and Control (CDC), Jeju Island, Republic of Korea*, pp. 704–709, IEEE, 2020.

[119] A. Narasingam, S. H. Son, and J. S. Kwon, "Data-driven feedback stabilisation of nonlinear systems: Koopman-based model predictive control," *International Journal of Control*, vol. 96, no. 3, pp. 770–781, 2023.

[120] S. H. Son, A. Narasingam, and J. S. Kwon, "Development of offset-free Koopman Lyapunov-based model predictive control and mathematical analysis for zero steady-state offset condition considering influence of Lyapunov constraints on equilibrium point," *Journal of Process Control*, vol. 118, pp. 26–36, 2022.

[121] J. A. Keith, V. Vassilev-Galindo, B. Cheng, S. Chmiela, M. Gastegger, K. R. Muller, and A. Tkatchenko, "Combining machine learning and computational chemistry for predictive insights into chemical systems," *Chemical Reviews*, vol. 121, no. 16, pp. 9816–9872, 2021.

[122] C. D. Rankine, M. M. Madkhali, and T. J. Penfold, "A deep neural network for the rapid prediction of X-ray absorption spectra," *The Journal of Physical Chemistry A*, vol. 124, no. 21, pp. 4263–4270, 2020.

[123] B. Bhadriraju, J. S. Kwon, and F. Khan, "OASIS-P: Operable adaptive sparse identification of systems for fault prognosis of chemical processes," *Journal of Process Control*, vol. 107, pp. 114–126, 2021.

[124] M. S. F. Bangi and J. S. Kwon, "Deep hybrid modeling of chemical process: Application to hydraulic fracturing," *Computers & Chemical Engineering*, vol. 134, p. 106696, 2020.

[125] S. Jiang and V. M. Zavala, "Convolutional neural nets in chemical engineering: Foundations, computations, and applications," *AIChE Journal*, vol. 67, no. 9, p. e17282, 2021.

[126] K. Wang, K. Li, L. Zhou, Y. Hu, Z. Cheng, J. Liu, and C. Chen, "Multiple convolutional neural networks for multivariate time series prediction," *Neurocomputing*, vol. 360, pp. 107–119, 2019.

[127] J. Lym, G. H. Gu, Y. Jung, and D. G. Vlachos, "Lattice convolutional neural network modeling of adsorbate coverage effects," *The Journal of Physical Chemistry C*, vol. 123, no. 31, pp. 18951–18959, 2019.

[128] B. Nagy, D. L. Galata, A. Farkas, and Z. K. Nagy, "Application of artificial neural networks in the process analytical technology of pharmaceutical manufacturing—a review," *The AAPS Journal*, vol. 24, no. 4, p. 74, 2022.

[129] D. Ma, L. Shang, J. Tang, Y. Bao, J. Fu, and J. Yin, "Classifying breast cancer tissue by raman spectroscopy with one-dimensional convolutional neural network," *Spectrochimica Acta Part A: Molecular and Biomolecular Spectroscopy*, vol. 256, p. 119732, 2021.

[130] A. Elbasir, B. Moovarkumudalvan, K. Kunji, P. R. Kolatkar, R. Mall, and H. Bensmail, "Deepcrystal: a deep learning framework for sequence-based protein crystallization prediction," *Bioinformatics*, vol. 35, no. 13, pp. 2216–2225, 2019.

[131] R. W. Epps, A. A. Volk, K. Abdel-Latif, and M. Abolhasani, "An automated flow chemistry platform to decouple mixing and reaction times," *Reaction Chemistry & Engineering*, vol. 5, pp. 1212–1217, 2020.

[132] J. Zhang, Y. Meng, J. Wu, J. Qin, T. Yao, and S. Yu, "Monitoring sugar crystallization with deep neural networks," *Journal of Food Engineering*, vol. 280, p. 109965, 2020.

[133] A. Gandhi and M. F. Hasan, "Machine learning for the design and discovery of zeolites and porous crystalline materials," *Current Opinion in Chemical Engineering*, vol. 35, p. 100739, 2022.

[134] W. Sun, A. R. Paiva, P. Xu, A. Sundaram, and R. D. Braatz, "Fault detection and identification using bayesian recurrent neural networks," *Computers & Chemical Engineering*, vol. 141, p. 106991, 2020.

[135] Z. Wu, D. Rincon, J. Luo, and P. D. Christofides, "Machine learning modeling and predictive control of nonlinear processes using noisy data," *AIChE Journal*, vol. 67, no. 4, p. e17164, 2021.

[136] Y. Zheng and Z. Wu, "Predictive control of batch crystallization process using machine learning," *IFAC-PapersOnLine*, vol. 55, no. 7, pp. 798–803, 2022.

[137] F. A. R. Lima, M. G. de Moraes, A. R. Secchi, and M. B. de Souza Jr, "Development of a recurrent neural networks-based NMPC for controlling the concentration of a crystallization process," *Digital Chemical Engineering*, vol. 5, p. 100052, 2022.

[138] W. Tang and P. Daoutidis, "Data-driven control: Overview and perspectives," in *2022 American Control Conference (ACC)*, pp. 1048–1064, IEEE, 2022.

[139] Y. Zheng, X. Wang, and Z. Wu, "Machine learning modeling and predictive control of the batch crystallization process," *Industrial & Engineering Chemistry Research*, vol. 61, no. 16, pp. 5578–5592, 2022.

[140] Y. Zheng, T. Zhao, X. Wang, and Z. Wu, "Online learning-based predictive control of crystallization processes under batch-to-batch parametric drift," *AIChE Journal*, vol. 68, no. 11, p. e17815, 2022.

[141] P. Shah, M. Z. Sheriff, M. S. F. Bangi, C. Kravaris, J. S. Kwon, C. Botre, and J. Hirota, "Deep neural network-based hybrid modeling and experimental validation for an industry-scale fermentation process: Identification of time-varying dependencies among parameters," *Chemical Engineering Journal*, vol. 441, p. 135643, 2022.

[142] M. S. F. Bangi, K. Kao, and J. S. Kwon, "Physics-informed neural networks for hybrid modeling of lab-scale batch fermentation for $\beta$-carotene production using saccharomyces cerevisiae," *Chemical Engineering Research and Design*, vol. 179, pp. 415–423, 2022.

[143] M. S. F. Bangi and J. S. Kwon, "Deep hybrid model-based predictive control with guarantees on domain of applicability," *AIChE Journal*, vol. 69, no. 5, p. e18012, 2023.

[144] N. Sitapure, R. Epps, M. Abolhasani, and J. S. Kwon, "Multiscale modeling and optimal operation of millifluidic synthesis of perovskite quantum dots: towards size-controlled continuous manufacturing," *Chemical Engineering Journal*, vol. 127905, 2020.

[145] B. J. Ridder, A. Majumder, and Z. K. Nagy, "Population balance model-based multiobjective optimization of a multisegment multiaddition (MSMA) continuous plug-flow antisolvent

crystallizer," *Industrial & Engineering Chemistry Research*, vol. 53, no. 11, pp. 4387–4397, 2014.

[146] J. Cho, H. Jin, D. G. Sellers, D. F. Watson, D. H. Son, and S. Banerjee, "Influence of ligand shell ordering on dimensional confinement of cesium lead bromide ($CsPbBr_3$) perovskite nanoplatelets," *Journal of Materials Chemistry C*, vol. 5, no. 34, pp. 8810–8818, 2017.

[147] N. Sitapure, T. Qiao, D. Son, and J. S. Kwon, "Kinetic Monte Carlo modeling of the equilibrium-based size control of $CsPbBr_3$ perovskite quantum dots in strongly confined regime," *Computers & Chemical Engineering*, vol. 139, p. 106872, 2020.

[148] N. Sitapure, T. Qiao, D. H. Son, and J. S. Kwon, "Modeling and size control of $CsPbBr_3$ perovskite quantum dots," in *American Control Conference (ACC), IEEE at Denver, Colorado, USA*, pp. 4331–4336, IEEE, 2020.

[149] N. Sitapure, R. W. Epps, M. Abolhasani, and J. S Kwon, "CFD-based computational studies of quantum dot size control in slug flow crystallizers: Handling slug-to-slug variation," *Industrial & Engineering Chemistry Research*, vol. 60, no. 13, pp. 4930–4941, 2021.

[150] K. Abdel-Latif, F. Bateni, S. Crouse, and M. Abolhasani, "Flow synthesis of metal halide perovskite quantum dots: from rapid parameter space mapping to ai-guided modular manufacturing," *Matter*, vol. 3, no. 4, pp. 1053–1086, 2020.

[151] M. V. Annaland, W. Dijkhuizen, N. Deen, and J. Kuipers, "Numerical simulation of behavior of gas bubbles using a 3D front-tracking method," *AIChE Journal*, vol. 52, no. 1, pp. 99–110, 2006.

[152] D. Bothe, M. Koebe, K. Wielage, and H.-J. Warnecke, "VOF-simulations of mass transfer from single bubbles and bubble chains rising in aqueous solutions," in *Fluids Engineering Division Summer Meeting*, vol. 36975, pp. 423–429, 2003.

[153] D. J. Benson, "Volume of fluid interface reconstruction methods for multi-material problems," *Applied Mechanics Reviews*, vol. 55, no. 2, pp. 151–165, 2002.

[154] H. Grzybowski and R. Mosdorf, "Modelling of two-phase flow in a minichannel using level-set method," *Journal of Physics*, vol. 530, no. 1, p. 012049, 2014.

[155] A. Soulaimani and Y. Saad, "An arbitrary Lagrangian-Eulerian finite element method for solving three-dimensional free surface flows," *Computer Methods in Applied Mechanics and Engineering*, vol. 162, no. 1-4, pp. 79–106, 1998.

[156] M. L. Rasche, M. Jiang, and R. D. Braatz, "Mathematical modeling and optimal design of multi-stage slug-flow crystallization," *Computers & Chemical Engineering*, vol. 95, pp. 240–248, 2016.

[157] M. Su and Y. Gao, "Air-liquid segmented continuous crystallization process optimization of the flow field, growth rate, and size distribution of crystals," *Industrial & Engineering Chemistry Research*, vol. 57, no. 10, pp. 3781–3791, 2018.

[158] W. Xin, G. Liejin, and X. Zhang, "Development of liquid slug length in gas-liquid slug flow along horizontal pipeline: experiment and simulation," *Chinese Journal of Chemical Engineering*, vol. 14, no. 5, pp. 626–633, 2006.

[159] Z. Peng, E. Doroodchi, and G. Evans, "DEM simulation of aggregation of suspended nanoparticles," *Powder Technology*, vol. 204, no. 1, pp. 91–102, 2010.

[160] T. Xu, M. L. Lam, and T.-H. Chen, "Discrete element model for suppression of coffee-ring effect," *Scientific Reports*, vol. 7, no. 1, pp. 1–10, 2017.

[161] M. Eslamian, "A mathematical model for the design and fabrication of polymer solar cells by spray coating," *Drying Technology*, vol. 31, no. 4, pp. 405–413, 2013.

[162] N. Sitapure and J. S. Kwon, "Neural network-based model predictive control for thin-film chemical deposition of quantum dots using data from a multiscale simulation," *Chemical Engineering Research and Design*, vol. 183, p. 595, 2022.

[163] L. Wang, L. R. Karadaghi, R. L. Brutchey, and N. Malmstadt, "Self-optimizing parallel millifluidic reactor for scaling nanoparticle synthesis," *Chemical Communications*, vol. 56, no. 26, pp. 3745–3748, 2020.

[164] W. Wang, Y. Zhang, W. Wu, X. Liu, X. Ma, G. Qian, and J. Fan, "Quantitative modeling of self-assembly growth of luminescent colloidal $CH_3NH_3PbBr_3$ nanocrystals," *The Journal of Physical Chemistry C*, vol. 123, no. 20, pp. 13110–13121, 2019.

[165] K.-S. Cho, D. V. Talapin, W. Gaschler, and C. B. Murray, "Designing PbSe nanowires and nanorings through oriented attachment of nanoparticles," *Journal of the American Chemical Society*, vol. 127, no. 19, pp. 7140–7147, 2005.

[166] X. Zhang, L. Lv, L. Ji, G. Guo, L. Liu, D. Han, B. Wang, Y. Tu, J. Hu, and D. Yang, "Self-assembly of one-dimensional nanocrystal superlattice chains mediated by molecular clusters," *Journal of the American Chemical Society*, vol. 138, no. 10, pp. 3290–3293, 2016.

[167] K. L. Maki and S. Kumar, "Fast evaporation of spreading droplets of colloidal suspensions," *Langmuir*, vol. 27, no. 18, pp. 11347–11363, 2011.

[168] A. Crivoi and F. Duan, "Three-dimensional Monte Carlo model of the coffee-ring effect in evaporating colloidal droplets," *Scientific Reports*, vol. 4, no. 1, pp. 1–6, 2014.

[169] R. D. Deegan, O. Bakajin, T. F. Dupont, G. Huber, S. R. Nagel, and T. A. Witten, "Capillary flow as the cause of ring stains from dried liquid drops," *Nature*, vol. 389, no. 6653, pp. 827–829, 1997.

[170] H. Hu and R. G. Larson, "Marangoni effect reverses coffee-ring depositions," *The Journal of Physical Chemistry B*, vol. 110, no. 14, pp. 7090–7094, 2006.

[171] H. Li, N. Liu, Z. Shao, H. Li, L. Xiao, J. Bian, J. Li, Z. Tan, M. Zhu, and Y. Duan, "Coffee ring elimination and crystalline control of electrohydrodynamically printed high-viscosity perovskites," *Journal of Materials Chemistry C*, vol. 7, no. 47, pp. 14867–14873, 2019.

[172] N. Sitapure and J. S. Kwon, "Model predictive control of spray coating of perovskite quantum dots for application in perovskite solar cells," in *2022 American Control Conference (ACC), Atlanta, GA.*, pp. 5334–5339, IEEE, 2022.

[173] J. Yuan, C. Bi, S. Wang, R. Guo, T. Shen, L. Zhang, and J. Tian, "Spray-coated colloidal perovskite quantum dot films for highly efficient solar cells," *Advanced Functional Materials*, vol. 29, no. 49, p. 1906615, 2019.

[174] N. Sitapure, T. H. Kwon, M. Lee, B. Kim, M. S. Kang, and J. S. Kwon, "Modeling ligand crosslinking for interlocking quantum dots in thin-films," *Journal of Materials Chemistry C*, vol. 10, no. 18, pp. 7132–7140, 2022.

[175] Y. Wang, J.-A. Pan, H. Wu, and D. V. Talapin, "Direct wavelength-selective optical and electron-beam lithography of functional inorganic nanomaterials," *ACS Nano*, vol. 13, no. 12, pp. 13917–13931, 2019.

[176] F. Palazon, Q. A. Akkerman, M. Prato, and L. Manna, "X-ray lithography on perovskite nanocrystals films: from patterning with anion-exchange reactions to enhanced stability in air and water," *ACS Nano*, vol. 10, no. 1, pp. 1224–1230, 2016.

[177] S. Denizligil, Y. Yagci, and C. McArdle, "Photochemically and thermally induced radical promoted cationic polymerization using an allylic sulfonium salt," *Polymer*, vol. 36, no. 16, pp. 3093–3098, 1995.

[178] P. Riesz and T. Kondo, "Free radical formation induced by ultrasound and its biological implications," *Free Radical Biology and Medicine*, vol. 13, no. 3, pp. 247–270, 1992.

[179] G. Fleet, R. Porter, and J. Knowles, "Affinity labelling of antibodies with aryl nitrene as reactive group," *Nature*, vol. 224, no. 5218, pp. 511–512, 1969.

[180] H. J. Curran, "Rate constant estimation for C1 to C4 alkyl and alkoxyl radical decomposition," *International Journal of Chemical Kinetics*, vol. 38, no. 4, pp. 250–275, 2006.

[181] B. A. DeGraff, D. W. Gillespie, and R. J. Sundberg, "Phenyl nitrene. flash photolytic investigation of the reaction with secondary amines," *Journal of the American Chemical Society*, vol. 96, no. 24, pp. 7491–7496, 1974.

[182] D. T. Gillespie, "Exact stochastic simulation of coupled chemical reactions," *The Journal of Physical Chemistry*, vol. 81, no. 25, pp. 2340–2361, 1977.

[183] L. Wang, Y. Zhu, H. Liu, J. Gong, W. Wang, S. Guo, Y. Yu, H. Peng, and Y. Liao, "Giant stability enhancement of $CsPbX_3$ nanocrystal films by plasma-induced ligand polymerization," *ACS Applied Materials & Interfaces*, vol. 11, no. 38, pp. 35270–35276, 2019.

[184] N. P. Gritsan, H. B. Zhai, T. Yuzawa, D. Karweik, J. Brooke, and M. S. Platz, "Spectroscopy and kinetics of singlet perfluoro-4-biphenylnitrene and singlet perfluorophenylnitrene," *The Journal of Physical Chemistry A*, vol. 101, no. 15, pp. 2833–2840, 1997.

[185] I. E. Pacios, A. Pastoriza, and I. F. Pierola, "Effect of the crosslinking density and the method of sample preparation on the observed microstructure of macroporous and conventional poly (n, n-dimethylacrylamide) hydrogels," *Colloid and Polymer Science*, vol. 285, no. 3, pp. 263–272, 2006.

[186] I. E. Pacios, M. J. Molina, M. R. Gómez-Antón, and I. F. Piérola, "Correlation of swelling and crosslinking density with the composition of the reacting mixture employed in radical crosslinking copolymerization," *Journal of Applied Polymer Science*, vol. 103, no. 1, pp. 263–269, 2007.

[187] I. E. Pacios and I. F. Piérola, "Discrimination of the roles of crosslinking density and morphology in the swelling behavior of crosslinked polymers: Poly (n-vinylimidazole) hydrogels," *Journal of Applied Polymer Science*, vol. 112, no. 3, pp. 1579–1586, 2009.

[188] J. Yang, M. Lee, S. Y. Park, M. Park, J. Kim, N. Sitapure, D. Hahm, S. Rhee, D. Lee, H. Jo, J. S. Kwon, and M. Kang, "Nondestructive photopatterning of heavy-metal-free quantum dots," *Advanced Materials*, p. 2205504, 2022.

[189] OpenAI, "GPT-4 technical report," vol. 2303.08774, 2023.

[190] T. Brown, B. Mann, N. Ryder, M. Subbiah, J. D. Kaplan, P. Dhariwal, A. Neelakantan, P. Shyam, G. Sastry, and A. Askell, "Language models are few-shot learners," *Advances in Neural Information Processing Systems*, vol. 33, pp. 1877–1901, 2020.

[191] A. Dosovitskiy, L. Beyer, A. Kolesnikov, D. Weissenborn, X. Zhai, T. Unterthiner, M. Dehghani, M. Minderer, G. Heigold, and S. Gelly, "An image is worth 16x16 words: Transformers for image recognition at scale," *arXiv preprint arXiv:2010.11929*, 2020.

[192] M. Shoeybi, M. Patwary, R. Puri, P. LeGresley, J. Casper, and B. Catanzaro, "Megatron-LM: Training multi-billion parameter language models using model parallelism," *arXiv preprint*, vol. 1909.08053, 2019.

[193] D. Narayanan, M. Shoeybi, J. Casper, P. LeGresley, M. Patwary, V. Korthikanti, D. Vainbrand, P. Kashinkunti, J. Bernauer, and B. Catanzaro, "Efficient large-scale language model training on GPU clusters using Megatron-LM," in *Proceedings of the International Conference for High Performance Computing, Networking, Storage and Analysis*, pp. 1–15, 2021.

[194] A. Radford, J. Wu, R. Child, D. Luan, D. Amodei, and I. Sutskever, "Language models are unsupervised multitask learners," *OpenAI blog*, vol. 1, no. 8, p. 9, 2019.

[195] Z. Liu, Y. Lin, Y. Cao, H. Hu, Y. Wei, Z. Zhang, S. Lin, and B. Guo, "Swin transformer: Hierarchical vision transformer using shifted windows," in *Proceedings of the IEEE/CVF International Conference on Computer Vision*, pp. 10012–10022, 2021.

[196] R. Rombach, A. Blattmann, D. Lorenz, P. Esser, and B. Ommer, "High-resolution image synthesis with latent diffusion models," in *Proceedings of the IEEE/CVF Conference on Computer Vision and Pattern Recognition*, pp. 10684–10695, 2022.

[197] G. Vogel, L. S. Balhorn, and A. M. Schweidtmann, "Learning from flowsheets: A generative transformer model for autocompletion of flowsheets," *Computers & Chemical Engineering*, p. 108162, 2023.

[198] J. Jumper, R. Evans, A. Pritzel, T. Green, M. Figurnov, O. Ronneberger, K. Tunyasuvunakool, R. Bates, A. Žídek, and A. Potapenko, "Highly accurate protein structure prediction with AlphaFold," *Nature*, vol. 596, no. 7873, pp. 583–589, 2021.

[199] R. Evans, M. O'Neill, A. Pritzel, N. Antropova, A. Senior, T. Green, A. Žídek, R. Bates, S. Blackwell, and J. Yim, "Protein complex prediction with AlphaFold-Multimer," *BioRxiv*, vol. 2021–10, 2021.

[200] A. W. Senior, R. Evans, J. Jumper, J. Kirkpatrick, L. Sifre, T. Green, C. Qin, A. Žídek, A. W. Nelson, and A. Bridgland, "Improved protein structure prediction using potentials from deep learning," *Nature*, vol. 577, no. 7792, pp. 706–710, 2020.

[201] V. Mann and V. Venkatasubramanian, "Predicting chemical reaction outcomes: A grammar ontology-based transformer framework," *AIChE Journal*, vol. 67, no. 3, p. e17190, 2021.

[202] N. Sitapure and J. S. Kwon, "Exploring the potential of time-series transformers for process modeling and control in chemical systems: an inevitable paradigm shift?," *Chemical Engineering Research and Design*, 2023.

[203] A. Vaswani, N. Shazeer, N. Parmar, J. Uszkoreit, L. Jones, A. N. Gomez, L. Kaiser, and I. Polosukhin, "Attention is all you need," *Advances in Neural Information Processing Systems*, vol. 30, 2017.

[204] J. Devlin, M.-W. Chang, K. Lee, and K. Toutanova, "BERT: Pre-training of deep bidirectional transformers for language understanding," *arXiv preprint*, vol. 1810.04805, 2018.

[205] N. Sitapure and J. S. Kwon, "CrystalGPT: Enhancing system-to-system transferability in crystallization prediction and control using time-series transformers," *Computers & Chemical Engineering*, 2023 *(under review)*.

# APPENDIX A

# LIST OF PUBLICATIONS

## A.1 List of Journal Publications

- **Sitapure, N.**, Qiao, T., Son, D. H., & Kwon, J. S.(2020). Kinetic Monte Carlo modeling of the equilibrium-based size control of $CsPbBr_3$ perovskite quantum dots in strongly confined regime. Computers & Chemical Engineering, 139, 106872.

- **Sitapure, N.**, Lee, H., Ospina-Acevedo, F., Balbuena, P. B., Hwang, S., & Kwon, J. S. (2021). A computational approach to characterize formation of a passivation layer in lithium metal anodes. AIChE Journal, 67 (1), e17073.

- **Sitapure, N.**, Epps, R., Abolhasani, M., & Kwon, J. S. (2021). Multiscale modeling and optimal operation of millifluidic synthesis of perovskite quantum dots: towards size-controlled continuous manufacturing. Chemical Engineering Journal, 413, 127905.

- **Sitapure, N.**, Epps, R. W., Abolhasani, M., & Kwon, J. S. (2021). CFD-based computational studies of quantum dot size control in slug flow crystallizers: Handling slug-to-slug variation. Industrial & Engineering Chemistry Research, 60 (13), 4930-4941.

- Lee, H., **Sitapure, N.**, Hwang, S., & Kwon, J. S. (2021). Multiscale modeling of dendrite formation in lithium-ion batteries. Computers & Chemical Engineering, 153, 107415.

- **Sitapure, N.**, Kwon, T. H., Lee, M., Kim, B., Kang, M. S., & Kwon, J. S. (2022). Modeling ligand crosslinking for interlocking quantum dots in thin-films. Journal of Materials Chemistry C, 10 (18), 7132-7140.

- **Sitapure, N.**, & Kwon, J. S.(2022). Neural network-based model predictive control for thin-film chemical deposition of quantum dots using data from a multiscale simulation. Chemical Engineering Research and Design, 183, 595-607.

- Hwang, G., **Sitapure, N.**, Moon, J., Lee, H., Hwang, S., & Kwon, J. S. (2022). Model predictive control of Lithium-ion batteries: Development of optimal charging profile for reduced intracycle capacity fade using an enhanced single particle model (SPM) with first-principled chemical/mechanical degradation mechanisms. Chemical Engineering Journal, 435, 134768.

- Yang, J., Lee, M., Park, S. Y., Park, M., Kim, J., **Sitapure, N.**, Hahm, D., Rhee, Seunghyun., Lee, D., Jo, H., Jo, Y. H., Lim, J., Jungwook, S., Tae, J., Lee D., Kwak, K., Kwon, J.S., Kim, B.,. Bae, W. K., & Kang, M. S. (2022). Nondestructive Photopatterning of Heavy-Metal-Free Quantum Dots. Advanced Materials, 34 (43), 2205504.

- Lee, C. H., Pahari, S., **Sitapure, N.**, Barteau, M. A., & Kwon, J. S. (2022). DFT–kMC Analysis for Identifying Novel Bimetallic Electrocatalysts for Enhanced NRR Performance by Suppressing HER at Ambient Conditions Via Active-Site Separation. ACS Catalysis, 12(24), 15609-15617.

- Cao, K., **Sitapure, N.**, & Kwon, J. S. (2023). Exploring the benefits of utilizing small modular device for sustainable and flexible shale gas water management. Journal of Cleaner Production, 384, 135282.

- **Sitapure, N.**, & Kwon, J. S. (2023). A Unified Approach for modeling and control of crystallization of quantum dots (QDs). Digital Chemical Engineering, 6, 100077.

- **Sitapure, N.**, & Kwon, J. S. (2023). Exploring the Potential of Time-Series Transformers for Process Modeling and Control in Chemical Systems: An Inevitable Paradigm Shift?. Chemical Engineering Research and Design.

## A.2 Conference Proceedings

- **Sitapure, N.**, Qiao, T., Son, D. H., & Kwon, J. S. (2020, July). Modeling and size control of $CsPbBr_3$ perovskite quantum dots. IN 2020 American Control Conference (ACC) (pp. 4331-4336). IEEE.

- **Sitapure, N.**, Epps, R., Abolhasani, M., & Kwon, J. S. (2021, May). Multiscale CFD modeling and optimal control of a continuous slug flow crystallizer for quantum dot production. In 2021 American Control Conference (ACC) (pp. 1016-1021). IEEE.

- **Sitapure, N.**, & Kwon, J. S. (2022, June). Model Predictive Control of Spray Coating of Perovskite Quantum Dots for Application in Perovskite Solar Cells. In 2022 American Control Conference (ACC) (pp. 5334-5339). IEEE.

- Hwang, G., **Sitapure, N.**, Moon, J., Hwang, S., & Kwon, J. S. (2022, June). Mitigation of intra-cycle mechano-chemical degradation-based capacity fade in Lithium-ion batteries: Application of a model predictive controller. In 2022 American Control Conference (ACC) (pp. 5282-5287). IEEE.